Row-Column Capacitive Micromachined Ultrasonic Transducers for Medical Imaging

by

I-Hsiang Chen

A thesis
presented to the University of Waterloo
in fulfillment of the
thesis requirement for the degree of
Doctor of Philosophy
in
Systems Design Engineering

Waterloo, Ontario, Canada, 2016

Author's Declaration

I hereby declare that I am the sole author of this thesis. This is a true copy of the thesis, including any required final revisions, as accepted by my examiners.

I understand that my thesis may be made electronically available to the public

Abstract

Ultrasound imaging plays an important role in modern medical diagnosis. Recent progress in real-time 3-D ultrasound imaging can offer critical information such as the accurate estimation of organ, cyst, or tumour volumes. However, compared to conventional 2-D ultrasound imaging, the large amount of data and circuit complexity found in 3-D ultrasound imaging results in very expensive systems. Therefore, a simplification scheme for 3-D ultrasound imaging technology is needed for a more wide-spread use and to advance clinical development of volumetric ultrasound. Row-column addressing 2-D array is one particular simplification scheme that requires only N + N addressing lines to activate each element in an N × N array. As a result, the fabrication, circuit, and processing complexity dramatically decrease. Capacitive micromachined ultrasonic transducer (CMUT) technology was chosen to fabricate the array as it offers micro-precision fabrication and a wide bandwidth, which make it an attractive transducer technology.

The objective of this thesis is to investigate and demonstrate the imaging potential of row-column CMUT arrays for RT3D imaging. First, the motivation, physics, and modelling of both CMUTs and row-column arrays are described, followed by the demonstration of a customized row-column CMUT pseudo-real-time 3-D imaging system. One particular limitation about row-column arrays discovered as part of this dissertation work is the limited field-of-view of the row-column arrays' imaging performance. A curved row-column CMUT array was proposed to improve the field-of-view, and the resulting modelling of the acoustic field and simulated reconstructed image are presented. Furthermore, a new fabrication process was proposed to construct a curved row-column CMUT array. The resulting device was tested to demonstrate its flexibility to achieve the necessary curvature. Finally, a new wafer bonding process is introduced to tackle the next generation of RC-CMUT fabrication.

Many of the new fabrication techniques reported in this work are useful for CMUT fabrication engineers. The analysis on row-column array also provides additional insights for 2-D array simplification research.

Acknowledgement

First, I would like to thank my supervisor, Prof. John Yeow, for giving me the opportunity to work in his lab, and to work on such an interesting research project. During the six years of my study, I have spent countless hours in the cleanrooms, printed many PCBs, and ordered many components and equipment; and my requests for the purchases were always approved. It is a wonderful feeling to know that there are always resources to support my project, and I am grateful for that. I would also like to thank the other members of my committee - Prof. Alex Wong, Prof. Patricia Nieva, and Prof. John Zelek - for being there when I had questions. I sincerely thank Prof. Xiaoning Jiang for agreeing to be the external examiner for my defense. In addition, I want to thank Prof. Alex Wong for always keeping an extra eye on me.

To my colleagues, you guys are some of the most amazing human beings I have ever met. First and foremost, the one person I am most indebted to is Lawrence Wong. Without him, I would probably break everything I touch. Thanks for always replying to my dumb questions, and thanks for being a great teacher. I honestly don’t know how I can repay you. To Zhenhao and Nash, you guys make the lab feel like home. Thanks for being there when I am at my lowest. Thanks for making me laugh so hard for so long. To Maziar, I really enjoy our talks. Thanks for walking across campus to help me out with my work without asking for anything. I will never take that for granted. I would like to thank all those (my sincere apologies to those whose names I might have missed) who have supported me in this journey.

To my partner, Erica, thanks for being so patient, loving, and kind. Hearing your voice on the phone at the end of each day really makes me stop thinking about work.

To my sister, Winnie, thanks for offering me great advice that I never listen to. More importantly, thanks for understanding how difficult it can be as a graduate student and letting me know that everything will be okay.

To my parents, I tear up every time I think about how wonderful you guys are and how lucky I am to be your son.

Table of Contents

List of Tables vii

List of Figures viii

Chapter 1 INTRODUCTION 1
- 1.1 Motivation 1
  - 1.1.1 Adopting Row-Column Addressing for 2-D arrays 1
  - 1.1.2 Adopting CMUTs 2
- 1.2 Objectives 2
- 1.3 Contribution 3
- 1.4 Thesis Organization 4

Chapter 2 BACKGROUND ON ULTRASOUND 5
- 2.1 Ultrasound Basics 5
- 2.2 Transducers 7
- 2.3 Probes and Arrays 9
- 2.4 Array Beamforming 11

Chapter 3 CAPACITIVE MICROMACHINED ULTRASONIC TRANSDUCERS 16
- 3.1 Background 16
- 3.2 CMUT Modeling 18
- 3.3 Simulation with Experimental Results 22
- 3.4 Design and Fabrication 25
  - 3.4.1 Membrane (Vibrating Plate): 26
  - 3.4.2 Surface micromachining CMUT fabrication 26
  - 3.4.3 Wafer Bonding Method 27
  - 3.4.4 Encapsulation 28
- 3.5 Benefits 29
  - 3.5.1 Wider-bandwidth 29
  - 3.5.2 Smaller-pitch 30
  - 3.5.3 IC integration 31
- 3.6 Arrays 32
  - 3.6.1 SMALL 1-D/Ring Array 33
  - 3.6.2 LARGE/HIGH-DENSITY 2-D ARRAY 34
  - 3.6.3 Sparse Array 35
  - 3.6.4 Synthetic Array 35
  - 3.6.5 Row-Column (AKA crossed electrodes) 35
- 3.7 Challenges 37

Chapter 4 ROW-COLUMN BEAMFORMING 38
- 4.1 Revisiting Motivation 38
- 4.2 Generalized Operation of RC-Array (Planar) 39
- 4.3 Fabrication of Row-Column CMUTs 42

4.4 Literature Review..44
4.5 Row-column resolution vs. Full-Matrix operation 47
4.6 A graphical look at RC beamforming..48
4.7 Limitations of RC Focusing..53
4.8 Simulation of Curved Array..54

Chapter 5 QUASI-REAL-TIME 3D ULTRASOUND IMAGING 58

5.1 Need for Customizable Ultrasound System...58
5.2 System Design 60
  5.2.1 Front-end System 61
  5.2.2 PXI-based Back-end System..62
  5.2.3 Tx Beamformer...63
  5.2.4 Target FPGA..64
  5.2.5 Host PC 64
5.3 Imaging Results 66
  5.3.1 Focusing Volume 70
5.4 Chapter Conclusion and Future Work 71

Chapter 6 FABRICATION OF A CURVED ROW-COLUMN ADDRESSED CMUT 72

6.1 Curvature-Stress Consideration 74
6.2 Fabrication 75
6.3 RC-CMUT 76
6.4 Thinning..78
6.5 Results and Discussion 81
6.6 Future Work: The Design of a Second Generation Curved CMUT Array........................85
6.7 Chapter Conclusion..87

Chapter 7 PRACTICAL CMUT FABRICATION WITH A NOVEL NITRIDE-TO-OXIDE BASED WAFER BONDING...89

7.1 Revisiting Wafer Bonding 89
7.2 Direct Bonding Considerations...92
  7.2.1 Surface Roughness and Nanopillars 92
  7.2.2 Problem with Current SOIs...94
  7.2.3 Good Practices for Silicon-to-Oxide Bonding..95
7.3 Nitride-to-Oxide Wafer Bonded CMUT...96
7.4 Characterization and Results...99
7.5 Discussion...108
7.6 Chapter Conclusion and Future Work 110

Chapter 8 SUMMARY 111

References 117

Appendix A Detail Design and Implementation of PXI-based Imaging System............135

Appendix B Matlab (Field II) code for curved RC-array 147

List of Tables

6-1: 32×32 RC-CMUT dimension summary. 78

7-1: Design parameters for 4.7-MHz, 16-element CMUT array 97

List of Figures

2-1: Time-of-Flight (TOF) of a simple pulse-echo with two defined boundaries of different materials. 6

2-2: Transducer and natural focusing 7

2-3: Transducer probe structural overview. 8

2-4: Array Probe 9

2-5: A Verasonics medical phased-array probe 10

2-6: Array/Probe Types 10

2-7: Phased-array transmit focusing 11

2-8: Received focusing 12

2-9: Types of probes and scan field 13

2-10: Adjusting for the travel time between elements and focusing points. 14

2-11: 2-D array for 3-D scan. 15

3-1: (Left) Different CMUT designs for different applications. (Middle) Large number of CMUTs with are connected to 100-µm by 200-µm contact pads. (Right) Electrodes are connected together to short several cells into a single element. 17

3-2: Cross-section schematic of a CMUT cell 18

3-3: 1-D model of the vibrating CMUT membrane. 19

3-4: COMSOL CMUT definition using axisymmetric 2D model. 23

3-5: Simulated frequency vs. pressure in air with resonant frequency close to 9.1-MHz with. 24

3-6: Hydrophone measurement of the single element. 25

3-7: Basic process steps for the sacrificial release fabrication method. 27

3-8: Wafer Bonding Process for CMUT fabrication. 28

3-9: Pitch vs. Grating lobe effect. 31

3-10: CMUT-in-CMOS refers to the process where CMUTs and CMOS are fabricated on a single wafer in parallel. 32

3-11: Flip-chip Integration: CMUT fabrication and CMOS process can be fabricated seperately 32

3-12: CMUTs can be built on-top of CMOS. This creates a very tight packaging. 32

3-13: Ring array designs are very popular in IVUS applications since they allow a hollow center for guide wires or the possible integration of a thermal ablation tool. 33

3-14: Some sparse array patters. Darker coloured pixels represent transmit elements and lighter pixels represent receive elements. 35

3-15: Row-column connection scheme. The top electrode are connected in columns while bottom are in rows. 36

3-16: A single transmit column beam is formed at the transmit event. During receive event, a 2D section (dark pixels) are recorded. 36

4-1: Row-Column addressing: transmit vs receive 40

4-2: Transmit focusing using RC array 41

4-3: For each transmit event, a 2-D scan information can be reconstructed in the elevation and depth direction. 41

4-4: Fabrication of RC-CMUT array 43

4-5: Transmit (one-way) acoustic field 49

4-6: Two-way beam profile (PSF) 50

4-7: Pulse echo response of three scatters located at on axis, [-1,-1]mm off axis, and also [3,3] mm off axis are presented here. Aperture size is 4.8 mm and focusing depth if 5 mm. The off-axis peaks are approimately 6-dB and 36-dB below the center peak. 51

4-8: 2.5 mm depth focusing of scatterers distributed 0.5 mm apart parallel to the y-axis. 52

4-9: 5 mm depth focusing of scatterers distributed 0.5mm apart parallel to the y-axis ... 52

4-10: 10 mm depth focusing of scatterers distributed 0.5mm apart parallel to the y-axis 53

4-11: Edge effects of RC-Arrays 54

4-12: Curved RC-array Aperture 55

4-13: One way acoustic profile (in elevation) of curved RC-array 56

4-14: B-mode image with the curved array 57

5-1: SEM images of a 32 × 32 element CMUT array. 61

5-2: Customized PCB for interfacing the CMUT with the front-end circuitry. Analog components (i.e. amplifiers) are connected to the sides/rows of the CMUT. Pulsers are connected to the top and bottom. 62

5-3: Ultrasound system block diagram. 63

5-4: Flowchart of firmware within the Host PC 65

5-5: Simulated B-Mode of wire targets. 67

5-6: Measured and reconstructed B-mode image of actual wire targets. Unfocused wire is seen on the bottom left. 67

5-7: Side view of the oil-tank set-up. The top view of the 3 pins is also shown. 68

5-8: Reconstructed image of the pin heads at 8 different azimuth angles. 69

5-9: 3D Rendered image of the volume created by the 3D Ultrasound Visualization (UltraVis) platform developed by Vision and Image Processing group at UW. 70

6-1: RC-CMUT 75

6-2: Fabrication steps for RC-CMUT and subsequent thinning methods........................ 76

6-3: Photo of the RC-CMUT array. (Left) Micrograph of with a 400 µm× 400µm sub-element consisting of 50 CMUT cells. The top/plate layer is electrically connected with other elements in columns. Bottom electrode is connected in rows. (Right) Top-view 78

6-4: Improved PDMS encapsulation method to prevent edge peeling. 80

6-5: Set-up for thinning. CMUT device is carefully placed, exposing the substrate to be etched, onto an uncured 1mm PDMS film. A polyimide (Kapton®) tape is adhered to glass slide before pouring PDMS over it. During etching, adhesive will dissolve; once etching finishes, polyimide can be peeled off leaving a smooth PDMS surface. PDMS thickness in front of device layer is approximately 350 µm. 80

6-6: Wire-bonds are made between CMUT contact pads and a flat cable prior to PDMS encapsulation. 8 rows and 8 columns were shorted together with a bonder for characterization purposes. 81

6-7: Membrane damages occurring at wide trenches using the Vertical-only design. 82

6-8: Thin plate failure would allow TMAH solution to creep in and etch the silicon row electrodes and cause critical failures. 82

6-9: CMUT after thinning can be curved. 83

6-10: Hydrophone measurement and spectrum of a pulse from the simultaneous transmission of 8x8 elements. The centre frequency is 3.1MHz and the bandwidth is 63%. 84

6-11: Hydrophone experiment after PDMS coating. Transmit power decreased by 80%. Fractional bandwidth is 74%. Centre frequency is 5.7MHz. 84

6-12: Hydrophone experiment after thinning. Centre frequency and fractional bandwidth are 4.5MHz and 82%, respectively. 85

6-13: (Top) a flexible circuit with matching contact pad footprint as the (bottom) RC-CMUT array is required for flip-chip bonding. 86

6-14: A flip-chip bonding can create a more robust device since wire-bond solution are easily damaged. 86

6-15: Nitride membrane can is resistant from TMAH etch-via-creeping. 88

7-1: The AFM scan shows a surface roughness of < 10 ÅRMS which is acceptable for achieving spontaneous bond. There are very few 10-nm nanopillars but at this thickness it is still bondable. 93

7-2: Although RMS roughness did not increase significantly at 600-nm thick deposition, the pillars are much more noticeable in size and frequency. These large pillars are attributed to bonding failures of thicker nitride films. 94

7-3: Fabrication Flow. 97

7-4: An 1-D 16 element CMUT array with 6-mm by 6-mm aperture. 98

7-5: Micrograph of fabricated CMUTs. Each element is 380 µm wide. 98

7-6: Scanning electron microscopy of CMUTs 99

7-7: After CMP, the nitride film is successfully flattened. Pillars are no longer noticeable and roughness dropped to 3ÅRMS. 100

7-8: Vibrometer displacement measurement of collapsed mode at +30-V bias with 10-Vpp AC signal at 10.25MHz. 101

7-9: Impedance Measurement of (top) pre-collapse and (bottom) collapse-mode operation. 102

7-10: A closer look at impedance Characterization 103

7-11: Phase of impedance 104

7-12: Determining transmit spectrum using hydrophone as receiver at 40-mm away. Center frequency is 1.7 MHz with a 122% -3-dB fractional bandwidth. 105

7-13: Receive test with commercial pulser as source and CMUT as receiver at 40-mm away. Centre frequency is measured to be 4.7 MHz with a 124% -3-dB fractional bandwidth. 106

7-14: Pulse-echo waveform. Centre frequency is measured to be 2.1 MHz while -6-dB fractional bandwidth is 100%. 107

7-15: Thickness detection of aluminum block. 108

Chapter 1 INTRODUCTION

1.1 Motivation

Real-time volumetric ultrasound imaging, also known as RT3D or 4-D imaging, is immensely valuable for several reasons. Given real-time visualization of a volume scan, medical practitioners can diagnose quicker and more accurately. This is important since precisely locating a desired 2-D scan, especially when the feature of interest is small, is challenging and non-trivial even for an experienced sonographer. With a volume image, physically adjusting the scan location can be done digitally. Generating an RT3D ultrasound image is an active research area with certain defined challenges. In this work, emphasis will be placed on transducer design from not only a fabrication, but also a system integration level.

1.1.1 Adopting Row-Column Addressing for 2-D arrays

A single ultrasound transducer element can generate a 1-D line of sight (A-line). The same transducer can be mechanically steered to form a 2-D or 3-D image. However, for real-time imaging, mechanical movements can limit scan-rates and deter image quality. In medical sonography, transducers are typically arranged in an array that employs electrical focusing such that physical movements are avoided (unless you want to scan a different part of the body). Although a fully addressed 2-D array can, in theory, provide the best 3-D scan in terms of resolution and contrast, it is almost impossible to realize such a system, as electrically addressing an array of N×N element is too difficult and too bulky for practical use. Moreover, if frame-rates similar to those used in clinical machines are used, the number of scan lines will be highly limited. Therefore, a simplification scheme to address a 2-D array is needed. For this dissertation work, a row-column addressing (RC) scheme is implemented on a 2-D array. This simplification scheme addresses each element in an N×N array with only N+N channels. With some trade-offs in imaging capabilities, this method greatly reduces the number of interconnects required for 3-D imaging. Another great advantage of the RC-method is that the scan-rate is comparable to that of an 1-D array which is the current industry standard.

1.1.2 Adopting CMUTs

Modern ultrasound imaging has progressed significantly since its inception. However, limitations still exist and largely centered around the digital image quality of the transducer. For example, the process of energy transfer from electrical domain and vice versa is still far from being perfect. In fact, the fundamental mechanism of generating sound is still being debated. The conventional method involves transferring a standing wave inside the piezoelectric transducer to the outside medium. As a result, the material and its thickness becomes important and the concept of acoustic impedance becomes very important. It is the acoustic impedance mismatch that impose many of the design trade-offs in transducer design. Furthermore, in high frequency (>25MHz) applications and in-vivo applications, precision in transducer array fabrication becomes the bottle-neck of image quality. These underlying challenges can be overcome through microfabrication technology. Capacitive micromachined ultrasonic transducers (CMUTs) generate ultrasound in a fundamentally different way than conventional transducers. Instead of generating sound through bulk piezoelectric material vibration, the CMUT membrane vibrates generate acoustic waves. As a result, loss due to impedance is no longer a bottleneck and the bandwidth can be greatly increased. Through microfabrication processes, the CMUT and CMUT array can be made incredibly small and precise. Furthermore, the ability to integrate with electronics makes it incredibly desirable for cutting-edge application.

Row-column CMUT array (RC-CMUTs) was first introduced in 2009 by Dr. Andrew Logan, my predecessor. The following year, I arrived to the lab and took over the project as Dr. Logan graduated from the lab. At the time, to acquire a simple 2-D planar scan would require a manual channel-by-channel scan with an oscilloscope. As a result, sampling a single transmit-receive event would consume a day's work, not including the data-processing. Therefore, it is not a surprise that the imaging capabilities of RC-CMUTs are not well-understood at the time.

1.2 Objectives

The objectives of my thesis project are to understand the imaging capabilities of RC-CMUTs and how to use it for medical imaging. The first objective requires the construction of a RC-CMUTs model for simulating and analyzing the acoustic field and imaging behaviour. A customized RC-CMUT imaging system needs to be built in order to compare the simulated and acquired/reconstructed data. The second objective involves the development of a new RC-

CMUT array design for medical imaging. Through modelling and system realization, it was determined that by curving the RC-CMUT array, a more practical device can be achieved for medical imaging. However, unlike polymer or organic-based electronics, the realization of a flexible silicon-based device is not well studied. Therefore, a new fabrication process must be developed to achieve this objective.

1.3 Contribution

My first contribution is adding knowledge to the study of RC-CMUTs. In particular, my analytical work provided insights to the imaging capability and limitation of RC-CMUT. The capability is explained by first creating a model to simulate acoustic field and reconstructed image. This is followed by verifying the model through a custom-built quasi Real-time 3D RC-CMUTs imaging system. Using both the model and custom-built system, I have identified and analyzed the limitation (i.e., field-of-view) of RC-CMUT.

My second contribution involves developing a novel method for constructing a curved/flexible RC-CMUT array. This method resulted in a device which overcame the identified limitation and also made the device more suitable for medical imaging. A subsequent novel complementary process was developed which added robustness and significantly reduced fabrication cost of the previous CMUT fabrication process.

Below is a list of selected publications where I am the primary author. For these work, I am responsible for all of the design, fabrication, integration, and analysis. The co-authors have provided help with minor experimental measurements and also reviewing/editing of the materials.

1. *Modelling of Row-Column Beamforming*.

   This work is presented in Chapter 4.6~4.8 and published in (conference proceeding):

   A. I. H. Chen, L. L. P. Wong and J. T. W. Yeow, "A CMUT-based finger-mounted 3D ultrasound probe," ***2014 IEEE International Ultrasonics Symposium, Chicago, IL,*** **2014, pp. 1603-1606.**

2. *Designed and Developed the first Row-Column CMUT pseudo-real-time imaging system.*

   This work is presented in Chapter 5 and published in (conference proceeding):

   A. I. H. Chen, L. L. Wong, A. S. Logan and J. T. W. Yeow, "A CMUT-based real-time volumetric ultrasound imaging system with row-column addressing," ***2011 IEEE International Ultrasonics Symposium, Orlando, FL*****, 2011, pp. 1755-1758.**

3. <u>*Curved RC-CMUT array fabrication*</u>

   This work is presented in Chapter 6 and published in (refereed journal):

   A. I. H. Chen, L. L. P. Wong, S. Na, Z. Li, M. Macecek and J. T. W. Yeow, "Fabrication of a Curved Row–Column Addressed Capacitive Micromachined Ultrasonic Transducer Array," in *Journal of Microelectromechanical Systems*, vol. 25, no. 4, pp. 675-682, Aug. 2016.

4. <u>*Novel (and practical) wafer-bonding process*</u>

   This work is presented in Chapter 7 and described in (refereed journal):

   A. I. H. Chen, L. L. P. Wong, Z. Li, S. Na, and J. T. W. Yeow, "*Practical CMUT Fabrication with a Novel Nitride-to-Oxide based Wafer Bonding Process,*" in *Journal of Microelectromechanical Systems.* (revised and resubmitted Nov.2016)

1.4 Thesis Organization

This dissertation is organized in seven chapters. Chapter 2 provides the relevant background information on ultrasound imaging; acoustic waves, fundamental acoustic physics, transducer basics, and beamforming. Chapter 3 introduces CMUTs and its advantages over traditional transducers. A 1-D model and finite element model will be presented followed by acoustic characterization of a single element CMUT for verification. The design and fabrication of CMUTs will also be discussed along with applications. Chapter 4 presents the motivation and operation of row-column addressing along with the state-of-the-art research in this area. The strengths and weaknesses of row-column imaging will also be discussed through acoustic field modelling. Chapter 5 describes a pseudo RT3D row-column CMUT ultrasound imaging system I have designed and built. Chapter 6 presents a novel curved CMUT-array fabrication method based on a double-SOI-bonding and wafer-thinning process. Chapter 7 presents a new wafer bonding process that uses nitride as the membrane. Chapter 8 includes the summary and contribution of my dissertation work.

Chapter 2 BACKGROUND ON ULTRASOUND

2.1 Ultrasound Basics

Ultrasound is defined as mechanical waves with operating frequencies beyond human audible range, which is around 20 kHz. Though mechanical waves can come in various forms, the most popular form used in medical diagnostic ultrasound is compression, or longitudinal, waves. A well-known relation of wave propagation in a medium is

$$c = \lambda f \tag{2.1}$$

where c is the speed of sound in a medium, λ the wavelength, and f the frequency. With a shorter wavelength, finer features can be spatially distinguished. This means resolution is typically better at higher frequencies. As an example, sound speed in tissue is ~1500 m/s and imaging at 5 MHz would give a wavelength of 300 µm. In contrast, a frequency around 100kHz would give you a wavelength of 1.5 cm which may not be useful for medical diagnosis. In diagnostic medical ultrasound, some common usages include prenatal monitoring, liver scans, and blood flow analysis. Ultrasound is also used for treatments such as shock wave therapy, lithotripsy, bone healing, and the enhancement of drug uptake. Generally, for diagnostic purposes, higher frequencies are used rather than higher intensities, which is more suitable for therapeutic use.

The basics of ultrasound imaging lies in the pulse-echo sensing principle. Ultrasound signals are created from the reflection and backscattering waves from structure with inhomogeneous acoustic impedance. Reflectance is defined as

$$RF = \frac{(Z_2 - Z_1)}{(Z_2 + Z_1)} \tag{2.2}$$

where Z_1 and Z_2 is the acoustic impedance of the two material. This means the reflection is stronger when the impedance mismatch is great, and thus easier to differentiate the two layers. Acoustic impedance is defined as

$$Z = \rho c \tag{2.3}$$

where ρ is the density of the medium (i.e. tissue) and c, again, is the speed of sound in the medium. In the human body, layers of inhomogeneous tissues exist where the slightly different acoustic response (acoustic impedance) for each layer can be distinguished. In the simplest case of imaging, a 'line of sight', or A-mode, can be acquired after sending an ultrasound pulse and receiving the vibration of the transducer afterwards. Since we know the speed of sound and the recorded timestamp, we can infer distance of the reflecting boundaries.

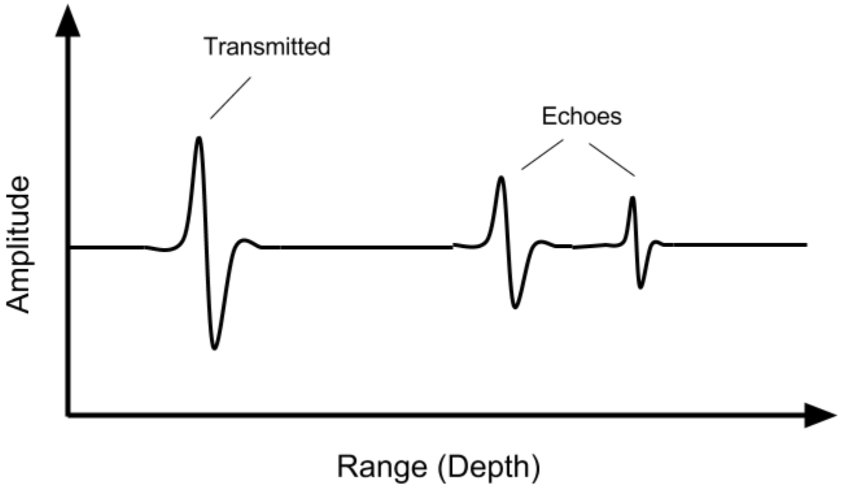

Figure 2-1: Time-of-Flight (TOF) of a simple pulse-echo with two defined boundaries of different materials.

A simple 2-D scan image, or Motion (M-) mode can be obtained by scanning the single probe in contact with the patient. At each line-of-sight, an envelope of received echoes is obtained after the signal amplification and demodulation. The lines can then be reconstructed into an image with the depth direction representing the received signal of each line and the lateral direction as the mechanical scanning direction.

With increasing pulses and scan lines, a better image can be acquired. However, much of the limitations around modern ultrasound systems centres around the speed of sound in the tissue. The minimum pulse repetition period, which defines how often we can fire pulses and ultimately governs the frame-rate, is limited by the time for the echo to arrive from the maximum depth. This limitation will be discussed in detail with examples in Chapter 4.1.

Another critical imaging consideration is the beam width of a transducer. A narrow beam width can distinguish a finer feature. Much like the specification of a camera, natural focusing depth, aperture size, depth-of-field, and f-number all apply to an ultrasound transducer. The lateral field profile at the focal spot can has a Sinc function profile. Thus, effective lateral width (full width at half maximum) is typically defined as the -3dB width from maximum.

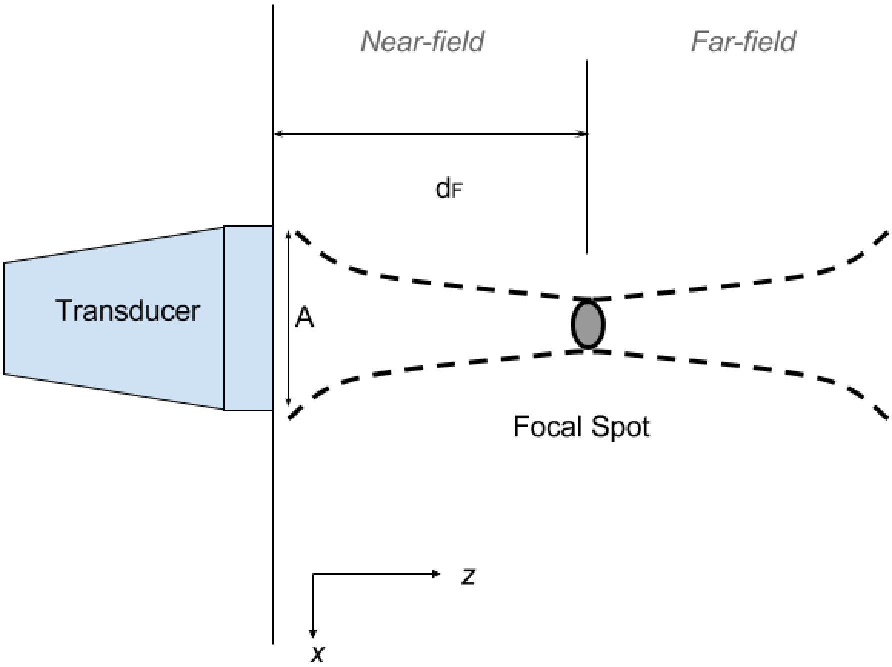

Figure 2-2: Transducer and natural focusing

In practice, transducers for medical imaging are almost always in an array form. A Brightness (B-) mode imaging is done where a 1-D array with generally 64~256 elements is fixed onto a probe and scanning can be made by activating the elements individually. The sequential A-lines then form a 2-D image without mechanical steering.

2.2 Transducers

Conventional transducers make use of the piezoelectric effect, where pressure on the piezoelectric material can be converted into electric energy and vice versa. Therefore, it is common to use the same transducer for both transmitting and receiving the ultrasound wave. In the transmit event, a voltage change causes material deformation which leads to mechanical waves being generated. In a receive event, the received wave generates mechanical stress, which induces material deformation and produces voltage signals. Currently, lead-zirconate-titanate ceramic (PZT) is the most common ultrasonic transducer material as it offers a high electro-mechanical conversion efficiency. PZT crystals can be diced and packaged to form a transducer probe. A structural overview of a standard ultrasonic probe is shown below.

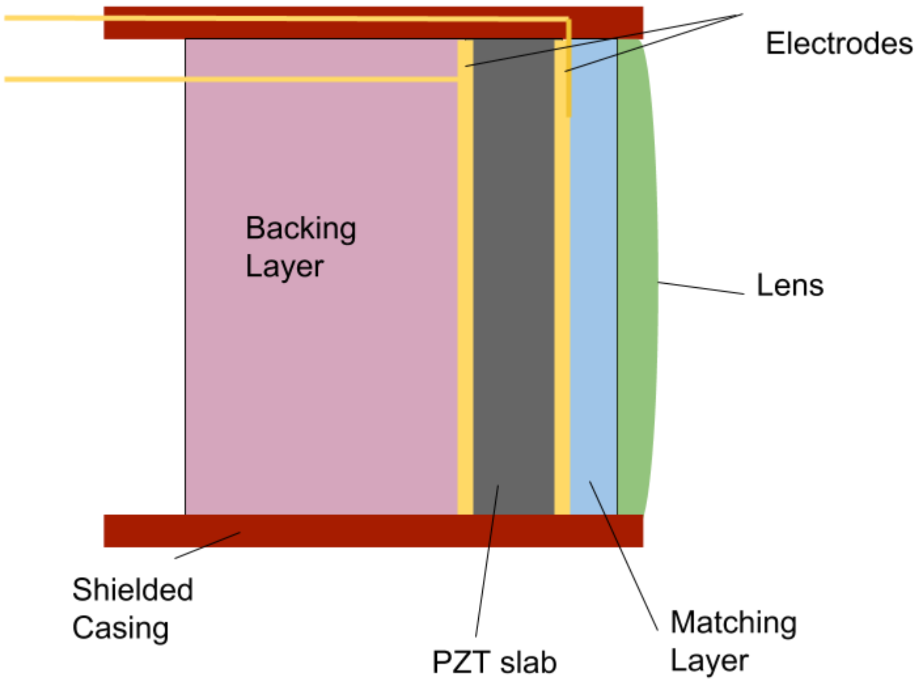

Figure 2-3: Transducer probe structural overview.

A probe is generally composed of a PZT layer, a matching layer, and a backing layer. The thickness, *d*, of the PZT slab is responsible for the occurrence of the standing wave and governed by the equation

$$d = \frac{n\lambda}{2} \tag{2.4}$$

This equation states the minimum slab thickness should be half of the wavelength to efficiently induce and maintain the standing wave. In addition to the PZT layer, a matching layer is needed to improve transmission efficiency since the acoustic impedance of the PZT is drastically different than the body. Given the reflection formula mentioned previously, the thickness of this matching layer should ideally be equal to a quarter of the wavelength. However, in practice, multiple matching layers are used to gradually match the PZT slab to the tissue layer. In addition to a matching layer, an acoustic lens is sometimes used to focus the beam for better resolution and contrast. Finally, a backing layer is needed to dampen the resonance of the PZT slab and reduce the ringing effect which improves the bandwidth. The backing would need to have similar impedance as the PZT for energy to move into the back, while the thickness needs to be greater than the slab to help attenuate the energy in the backing layer. However, with the increase of the backing layer, a great portion (~50%) of acoustic power from the PZT slab on commercial probes dissipates. Since the image quality is fundamentally limited by the transducer, ultrasound engineers are still working on improving transducer designs. Recent trends have been dedicated on improved forms of PZT ceramics that have lower acoustic impedances, to match the tissue, and also wider bandwidth and higher electro-mechanical efficiency.

2.3 *Probes and Arrays*

Medical imaging probes used multiple transducer elements to form a transducer array. These transducer elements are typically 0.3 to 1.5 wavelengths at 50~150 µm apart.

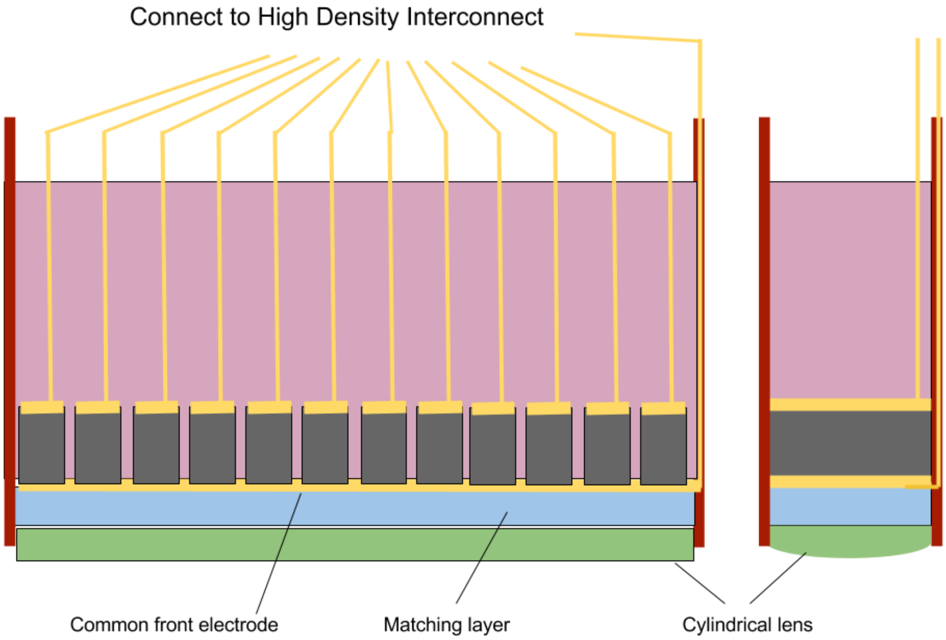

Figure 2-4: Array Probe

A high-end commercial probe would have 128 to 256 transducer elements on the same probe while operating at 1 to 15 MHz.

Figure 2-5: A Verasonics medical phased-array probe

Medical probes can be divided into four types of imaging arrays: linear, phased, curvilinear, and radial as shown in Figure 2-6.

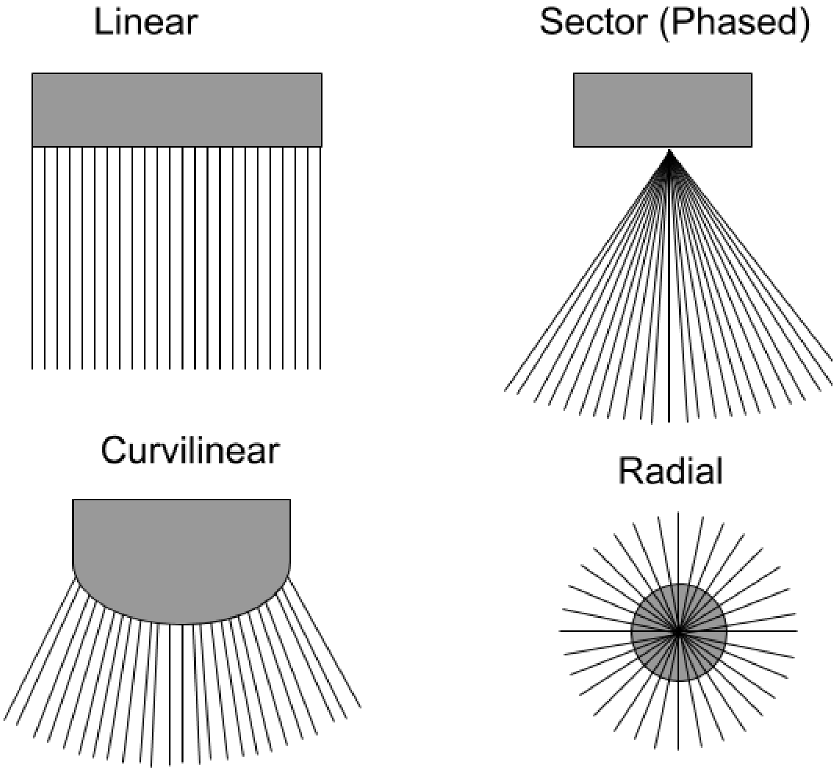

Figure 2-6: Array/Probe Types

Linear array has a field-of-view with constant width and is suitable for imaging organs close to the skin. For cardiovascular imaging, most of the acoustic energy would reflect back if the ribs are in the way as bones' acoustic impedance is much higher than tissue. This is why phased array is used as it has a fan-shaped field-of-view allowing sound enter through a tiny acoustic window while acquiring much of the information in deeper depth. Other popular array includes curvilinear which provides a wider field-of-view and also radial array, which is commonly used in endovascular imaging.

2.4 Array Beamforming

Earlier in the chapter, scanning using linear array transducer was discussed where the individual firing of an element can generate a 2-D image. Beamforming is the act of focusing sound in a given space. In a standard operation of a linear array, a subset of neighbouring elements is used for a single instance of pulse-echo. To obtain a narrower beam, these 'active' elements can be fired at different time as shown in Figure 2-7. As sound from the elements away from the center travel longer to reach a point directly in front of the array, these outer elements can be pulsed at nanoseconds quicker than the center elements such that all the pulses from every element reach this point at the same time. The angle and depth delays for each element can be stored on a Field Programmable Gate Array (FPGA) board. The FPGA can then trigger a small square pulse that triggers a high-voltage switch to pulse the transducer element.

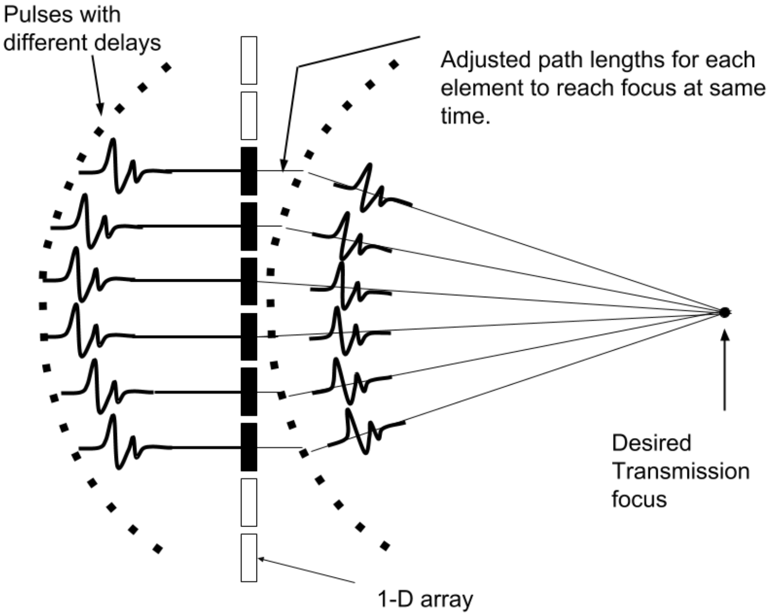

Figure 2-7: Phased-array transmit focusing

Similarly, the echo source can reach the same set of transducer elements with the same delay, creating a two-way focus and further enhancing the contrast. In Figure 2-8, the reflected pulses are out of phase from each other once they converted into electrical signals. The microprocessor can shift each of the signals such that they are in the same phase and then summed for a much higher signal-to-noise ratio pulse. Typically, the summing is done in a computer rather than a FPGA as it goes into signal processing for image reconstruction. Although much of this process was once done in analog processing, modern ultrasound systems have an analog-to-digital convertor placed before the signals go into delays.

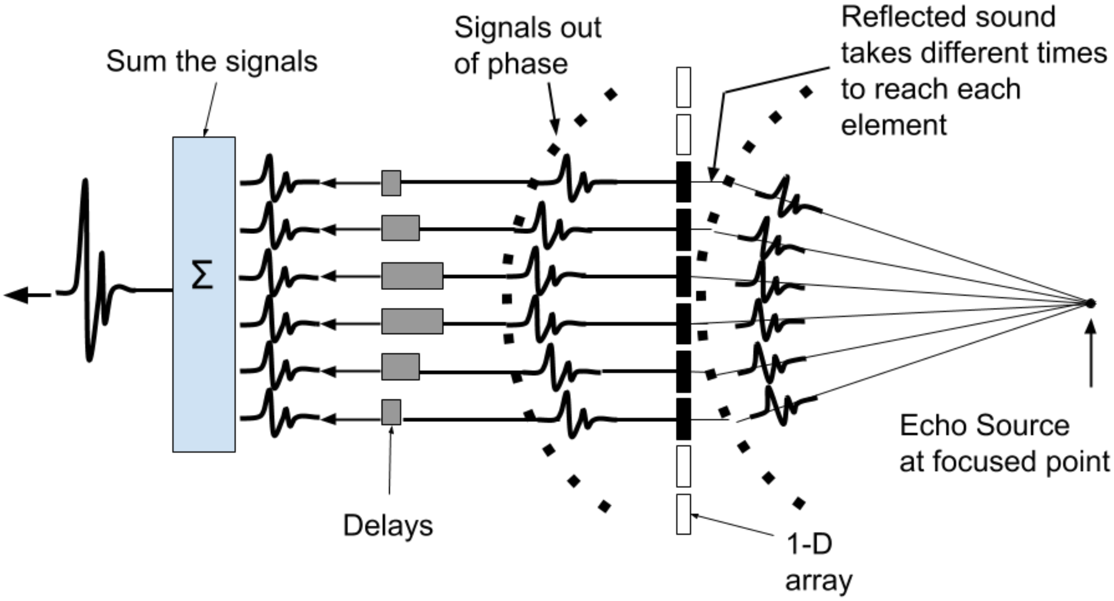

Figure 2-8: Received focusing

In a linear array, this type of beam-focusing method can be repeated from one of the sub-arrays to the other end. A similar method can be used in a curved array as well. As for a phased array transducer, the beam is not only focused but also steered at different angles. The scan areas can be seen in Figure 2-9. In linear arrays, the number of elements in a sub-aperture can be controlled to adjust for the focusing depth and the beam profile. With sub-aperture delay-focusing, activating 16 elements for beamforming can achieve a much narrower profile than 8 elements at the cost of blurring objects away from the focusing depth. Modern ultrasound systems can dynamically control the number of active elements and have multiple focusing depth for better resolution. A phased-array transducer typically uses most of its transducer elements unless there are too many channels. With more elements activated, the sound pressure generated can be much higher therefore allowing a deeper focus depth. Phased-array transducers also perform angular steering in addition to depth steering. The array probes are designed much smaller in total aperture sizes which allows sound to penetrate between the bones of the rib cage which otherwise would not allow most of the sound waves to penetrate through and image behind the ribs. As a result, echocardiography is typically done with phased-array transducers rather than linear/curved.

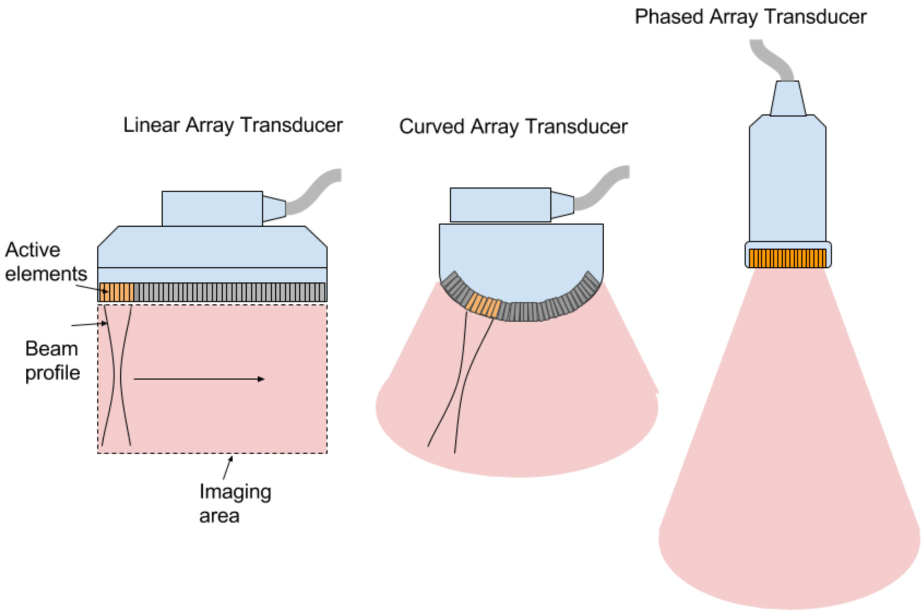

Figure 2-9: Types of probes and scan field

Geometric calculation is made to determine the delay between elements for each transmit-receive event. As shown in Figure 2-10, using simple trigonometry, the distance, r', from the desired focus point to each element that is placed x distance away from the centre of the array can be calculated given that r is the shortest, or radial, distance from the focusing point to the aperture.

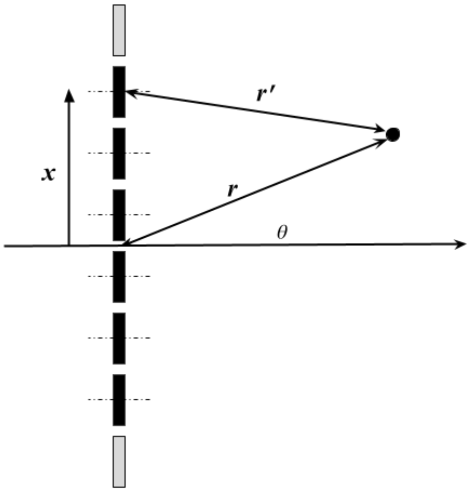

Figure 2-10: Adjusting for the travel time between elements and focusing points.

The distance is found to be

$$r^{'} = \sqrt{x^2 - 2rsin\theta + r^2} \tag{2.5}$$

The time of flight difference that is required to correct for the delay would be given by

$$\varDelta t = \frac{r^{'} - r}{c_L} \tag{2.6}$$

Therefore, in order for all the pulse to travel at the same time, each element should be fired $\varDelta t$ after the center element is triggered. Likewise, receive beamforming is calculated and constructed in a similar manner.

The exact same principle on 1-D phased array can be extended to 2-D arrays to achieve a pyramidal volume scanning, as shown in Figure 2-11. A 1-D phased array has a single angular freedom whereas a 2-D would have two degrees of angular scanning capability. The challenges associated with a 2-D array for 3-D imaging will be discussed in the next few chapters.

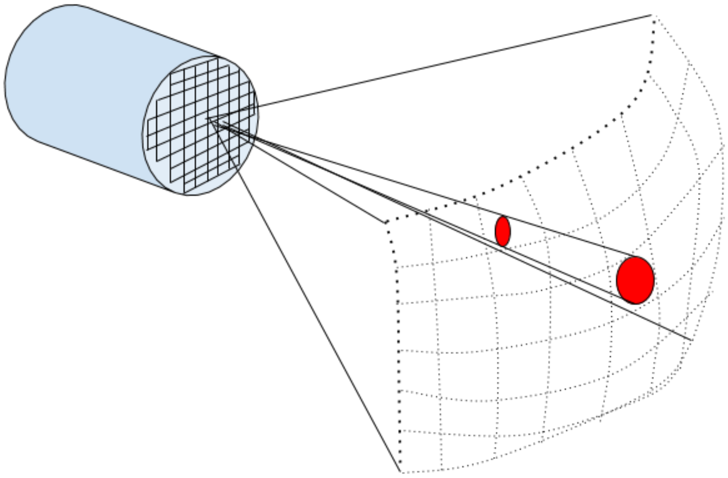

Figure 2-11: 2-D array for 3-D scan.

Chapter 3 CAPACITIVE MICROMACHINED ULTRASONIC TRANSDUCERS

3.1 Background

Conventional ultrasonic transducers are made with piezoelectric materials such as lead zirconate titanate (PZT). One of the short-comings of these transducers is that their acoustic impedance is significantly different than that of air. A typical piezoelectric transducer may have an acoustic impedance of 30 MRayl (Rayl is the notation for Rayleighs, defined as kg/m^2s), which is significantly larger than that of air, which is ~400 Rayl. Given the large mismatch in impedance, it is very difficult to transfer energy from the transducer to air without significant loss. This physical limitation was eventually addressed with a different mode of vibration. Instead of generating sound pulse within a *bulk* material such as piezo-based actuation, a design much like that of a condenser microphone can be used to displace the air through thin plate vibration. However, to move a thin plate at ultrasonic frequency would require a very precise dimension and the emergence of micro-electro-mechanical-systems (MEMS) fabrication in the latter part of twentieth century provided the solution for it. Using microfabrication, sub-micrometer thick capacitor plates with submicron vacuum gaps could be made. Since the physics of energy transfer is no longer based on creating waves inside the bulk material, impedance matching is no longer impeding the energy transfer of energy. The actuation physics of CMUTs will be discussed in detail in Section 3.2.

Research in capacitive micromachined ultrasonic transducers (CMUTs) has demonstrated promising progress as they can be made in much smaller scale with astonishing precision as shown in Figure 3-1. The MEMS-based transducer was first constructed by Haller and Khuri-Yakub [3.1] from Stanford University in 1994. These researchers envisioned a new type of transducer, fabricated using MEMS technology, for detecting cracks on aircrafts. These transducers demonstrated excellent sensitivity and were able to offer superior resolution than traditional PZT transducers. It was soon realized that an even higher performance resulted when the transducer was immersed [3.2][3.3]. As the imaging resolution is generally limited by the transducer, this had led to an incredible growth of interest toward CMUT research for medical imaging.

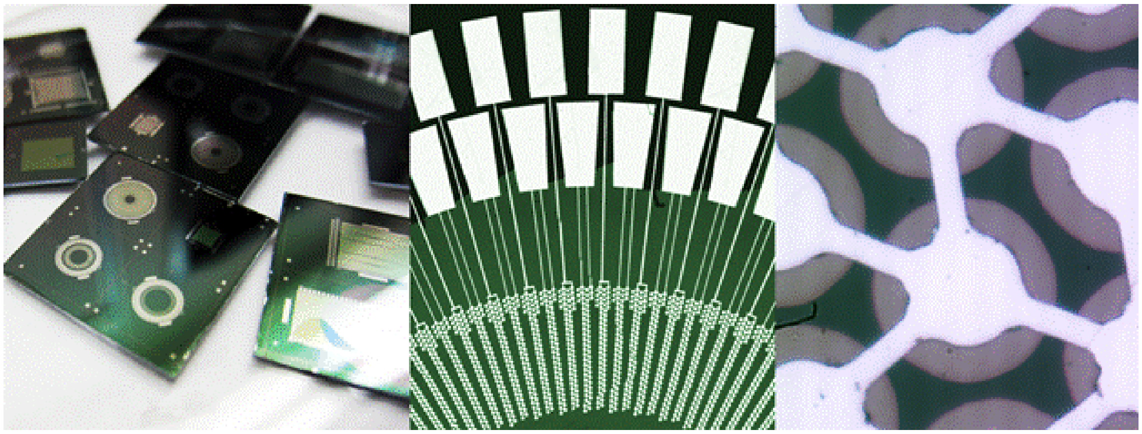

Figure 3-1: (Left) Different CMUT designs for different applications. (Middle) Large number of CMUTs with are connected to 100-µm by 200-µm contact pads. (Right) Electrodes are connected together to short several cells into a single element.

A cross section schematic of a CMUT is shown in Figure 3-2. The CMUT structure can be seen as a parallel plate capacitor, with the top electrode and the membrane forming the top plate and the bottom electrode and the substrate forming the bottom plate. A CMUT cell consists of a vibrating membrane, a vacuum cavity, an insulation layer and top and bottom electrodes. A layer of insulator material is required to prevent the two electrodes from shorting. The cavity is vacuum-sealed to eliminate squeeze-dampening effect. Due to the atmospheric pressure, the membrane is naturally pulled towards the bottom electrode which increases the electrostatic force. In turn, this increases sensitivity and lowers the required bias voltage. When provided with a voltage pulse, the top plate vibrates and hence transmits a burst of sound wave. Conversely, when sound waves hit the top plate, the membrane displaces and, in turn, changes the capacitance between the plates. During this *receive* event, the voltage across the electrodes is held fixed so as capacitance changes, electrical current is produced. From this step onwards, the rest of the imaging system varies little from a conventional ultrasound imager.

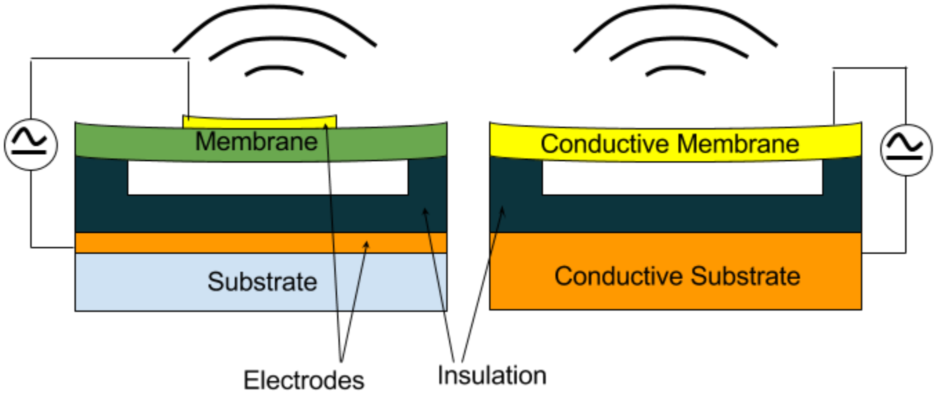

Figure 3-2: Cross-section schematic of two versions of CMUT cell.

CMUTs are fabricated using the same techniques as the common integrated circuit (IC) production. As a result, these novel transducers can be manufactured at a lower cost and with a higher yield. More importantly, standardized micromachining techniques allow CMUTs to be fabricated on ICs (CMUT-on-CMOS) which means integration with microelectronic circuits can be made with micro-level control. For devices that require minimum foot-print in packaging such as *in-vivo* imaging probes, integration with electronics is of great importance.

3.2 CMUT Modeling

The acoustic pressure is generated by the CMUT's membrane displacement. More specifically, the magnitude of the generated pressure wave is mainly dependent on the volume velocity, or the rate of change of the fluid volume that the membrane displaces during vibration [3.4]. A 1-D model of CMUT will presented as it helps explain how its physical design affects its mechanical, acoustics, and electrical behavior. Performance metric such as CMUT's output pressure can be calculated. Pressure governs how powerful the pulse is and how far the sound can travel. Consequently, a strong output pressure leads to a stronger reflected sound, which gives a higher received signal-to-noise ratio. The natural frequency can also be determined through modelling. Determining frequency is essential as it defines the application of interest. In this chapter, a 1-D CMUT model will be presented to study the behavior of CMUT.

Figure 3-3 depicts a rigid CMUT cell with a vacuum cavity supporting a membrane that is fixed at the circumference while the center is free to vibrate parallel to the centre axis. In the early stages of CMUT modelling, the membrane vibration is simplified to a piston-like motion where every point on the surface is assumed to have the same displacement. The more updated model [3.5] adjusts for the fact that the displacement, *w*, varies with radius.

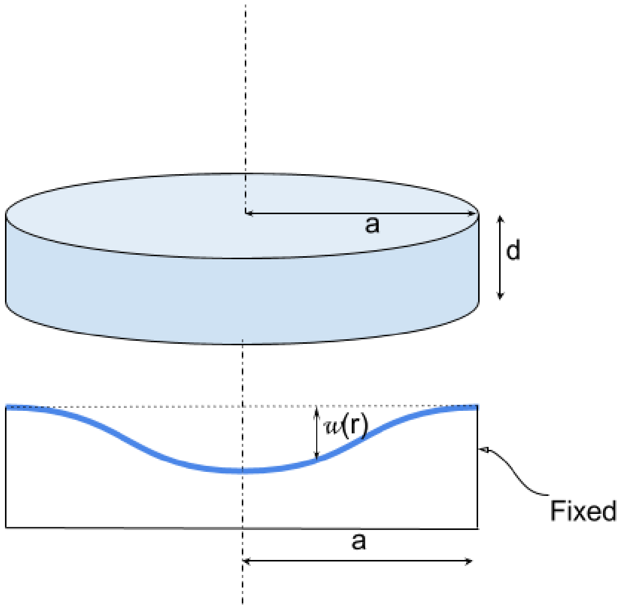

Figure 3-3: 1-D model of the vibrating CMUT membrane.

To calculate the acoustic pressure, which is an essential parameter that governs not only how far a strong pulse can travel but also the signal-to-noise ratio, the membrane displacement is considered non-uniform about the radius. Using a shape function based on plate theory [3.5], the membrane deflection across the membrane can be described as,

$$w(r) = w_{max}(1 - \frac{r^2}{a^2})^2 \tag{3.1}$$

where w_{max} is the maximum displacement, which is also at the center of the membrane, and *a* is the radius of the membrane. Since operating near pull-in yields the highest efficiency, the volume displaced by the membrane at this instance is

$$\int_0^a 2\pi r w_{max}(1 - \frac{r^2}{a^2})^2 dr = \frac{w_{max}}{3}\pi a^2 \tag{3.2}$$

Where *d* is the gap height with no deflection. In [3.5], it can be proved that the peak displacement, w_{max}, is 46% of the gap height, assuming the ratio of gap height to membrane thickness is small [3.5]. The standard CMUT lumped element model treats the CMUT as a vibrating piston with equal displacement across the surface. Therefore, some sort of conversion must be made to determine the equivalent (effective) piston radius, a_{eff}. The pull-in of a piston occurs at one third of the vacuum gap height, hence the volume displaced is equal to $\pi a_{eff} 2d/3$. Equating with (3.2), we find

$$a_{eff} = 0.68a \tag{3.3}$$

Compared with piezoelectric crystals where the whole surface can vibrate, CMUTs only have about 68% of surface responsible for vibrating. In practice, hundreds of CMUTs are used for a single transducer element to generate a stronger pulse. Yet, the space in between CMUTs and almost a third of the total CMUTs aperture are not responsible for generating pressure. As a result, factors such as effective surface area and fill-factor are important design concerns when designing a CMUT aperture.

The dynamics of CMUT in lumped model consists of a mass, a spring, and a damper. Assuming no external force, the equation of motion is expressed as

$$m\frac{d^2x}{dt^2} + b\frac{dx}{dt} + kx + f_e = 0 \tag{3.4}$$

where x is the displacement of the membrane, m is the mass of the piston, b is the damping coefficient, k is the spring constant, and f_e is the electrostatic force acting on the piston. Since CMUT consists of a top and bottom electrode, it can be seen as a capacitor that stores an electric energy

$$W = \frac{CV^2}{2} = \frac{\epsilon SV^2}{2(d+x)} \tag{3.5}$$

where C is the capacitance, V is the potentiation difference between the electrode, S is the area of the piston ($S = 0.46\,\pi a^2$), and ϵ is the permittivity of the medium between the electrodes. Thus, the electrostatic force can be seen as

$$f_e = \frac{dW}{dx} = \frac{\epsilon SV^2}{2(d+x)^2} \tag{3.6}$$

Substituting (3.6) into (3.4) yields a steady state equation of

$$kx + \frac{\varepsilon SV^2}{2(d+x)^2} = 0 \tag{3.7}$$

Since physically, k can only be in the $-d \leq x \leq 0$ while at pull-in voltage x = -d/3, the spring constant can be expressed as

$$k = \frac{27\varepsilon SV_{collapse}^2}{8d^3} \tag{3.8}$$

The collapse voltage can be calculated but given the variability in fabrication processes and materials, it is typically measured. We purposely fabricated a single element CMUT through a wafer bonding process with a membrane diameter of 60 µm, and a cavity depth of 240 nm. The membrane thickness is 1.6 µm while the insulation layer is 260 nm. Given a dielectric constant of 3.9 for wet-grown silicon dioxide, $d = 260\,nm + {}^{1}/_{3.9}\,(240\,nm) = 321\,nm$. The piston surface area, $S = 0.46\pi(30\mu m)^2 = 1.3 \times 10^{-9} m^2$. The collapse voltage was measured to be 110 V (using impedance analyzer). The spring constant k is estimated to be 14211 N/m.

In immersion operation, the damping of the system is largely dominated by the radiation impedance as the medium can be seen as a loading to the system. The effect of radiation impedance can be modeled as a complex value and is a function of the frequency. The radiance impedance can be modelled using the Bessel and Struve function. A circular piston in an infinite rigid baffle has a radiation impedance [3.4] of

$$Z_r = \rho_0 c S \left[1 - \frac{J_1\left(\frac{2\omega a_{eff}}{c}\right)}{\frac{2\omega a_{eff}}{c}} + j \frac{H_1\left(\frac{2\omega a_{eff}}{c}\right)}{\frac{2\omega a_{eff}}{c}} \right] \tag{3.9}$$

where ρ_0 is the densitiy of the medium, *c* is the speed of sound in the medium, J_1 is the first order Bessel function, H_1 is the first order Struve function, and *ω* is the angular ultrasound frequency. A first order estimate for the radiation impedance can be found if the operating frequency and aperture of the piston is low relative to the speed of sound (i.e. $\frac{\omega a_{eff}}{c} \ll 1$). Thus, the real (resistance) and imaginary (reactance) part can be found as part is

$$R_r \approx \frac{\omega^2}{2c} \rho_0 {a_{eff}}^4 \tag{3.10}$$

$$X_r \approx \frac{8}{3} \rho_0 \omega {a_{eff}}^3 \tag{3.11}$$

The density of human tissue is ~1000 kg/m^3, speed of sound is ~1500 m/s, and the ultrasound frequency is 2.6 MHz. The damping factor, *b*, can be estimated as the magnitude of the radiation impedance, which is calculated to be 1.5×10^{-5} Ns/m.

The resonant frequency for the lumped model is

$$f = \frac{1}{2\pi} \sqrt{\frac{k}{m}} \tag{3.12}$$

where *m* is the equivalent mass of the membrane. In vacuum or air, this mass would be similar to the mass of the membrane itself. However, in immersion, the radiation reactance also contributes to the vibration. Again, given that $\frac{\omega a_{eff}}{c} \ll 1$ holds true, the mass induced by radiation reactance is [3.4]

$$m_r = \frac{X_r}{\omega} = \frac{8}{3}\rho_0 {a_{eff}}^3 \tag{3.13}$$

The mass induced by radiation reactance is calculated to be 2.26×10^{-11} kg. Including the mass of the membrane itself, the total mass would be 3.64×10^{-11} kg. Since a DC bias is applied to the CMUT, it creates a pre-displaced spring which would weaken the spring, thus creating a spring softening effect. Hence, the k in equation 3.12 needs compensate for this spring

$$k_{soft} = k - \frac{\varepsilon S V^2}{d^3} \tag{3.14}$$

The measured resonant frequency (2.6 MHz) was recorded at 100-V bias voltage so the adjusted spring factor can be found to be 10732 N/m.

The measured (2.6MHz) and calculated (2.7MHz) frequency using (eq. 3.12) are very close. Possible explanation for the minor mismatch could be attributed to minor fabrication deviation from designed parameters. Furthermore, the model was derived from a measured pull-in voltage which is likely smaller than the theoretical pull-in value since the dynamics of the membrane behaves very unstable as the voltage approaches pull-in. This results in a reduced spring factor which would agree with the lowered measured voltage.

3.3 Simulation with Experimental Results

As mentioned in Section 3.2, a one element CMUT array was fabricated and used for the model verification. The fabrication process, which uses a wafer bonding process, will be presented in the Section 3.4. Through lumped modelling, the frequency and collapse-mode voltage can be determined as discussed in Section 3.2. Another method for modelling is the use of COMSOL Multiphysics for finite element analysis (FEA). To simulate the CMUT, an axisymmetric 2D model was developed as depicted in Figure 3-4. The CMUT parameters are identical as Section 3.2.

The model consists of a bottom insulation layer, a vacuum cavity, an inner membrane with equal radius to the physical electrode (15 µm) to apply electrical terminal settings, an outer membrane, and a rectangular fluid domain. For the highly doped silicon membrane model, the inner and outer membrane is set to be electrically shorted. The membrane and substrate material was set to silicon (density 2330 kg/m2, Young’s Modulus 150GPa, Poisson’s Ratio 0.16), cavity material was set to air with relative permittivity 1, and fluid domain set to vegetable oil with modified properties (Density 943kg/m^2, Speed of Sound 1540m/s). Under the physics node, Electromechanics was applied to the solid domains and the cavity, under which Linear Dielectric was assigned to the solid domains enabling structural mechanics calculation. Pressure Acoustics Frequency Domain was applied to the fluid domain. Fixed constraint was applied to all solid domains with the exception of the membrane, which allowed the membrane to vibrate freely. In correspondence to the benchmark simulation model, the top electrode terminal was applied to the bottom surface of the inner membrane, while the top of the insulation layer was grounded. Under Pressure Acoustics, a background pressure field of 1 atm was applied to the fluid domain, symmetry boundaries were applied to the vertical fluid column edges, and plane wave radiation was applied to the absorbing boundary that was placed 1 mm away from the membrane. Appropriate boundary settings were applied to fully couple Electromechanics and Pressure Acoustics. In the study node, a pre-stressed frequency perturbation study was created, which consisted of a stationary study step to bias the CMUT membrane using DC voltage, and a harmonic study step to calculate the CMUT's frequency response based on pre-stressed stationary results.

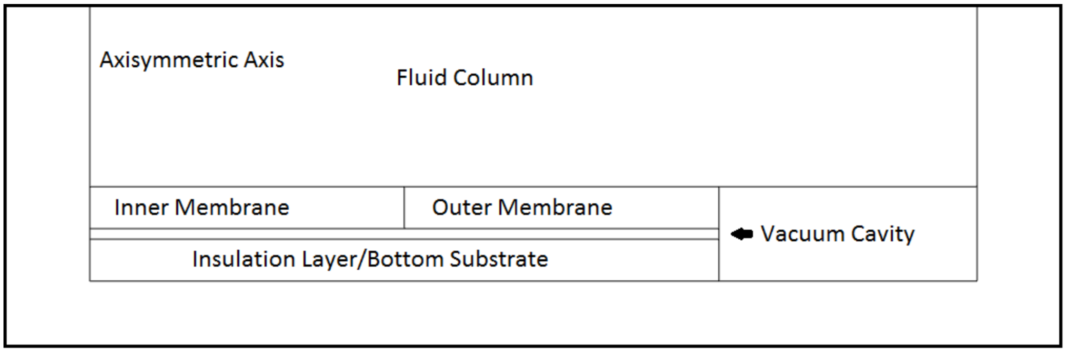

Figure 3-4: COMSOL CMUT definition using axisymmetric 2D model.

The maximum displacement (i.e. at centre) of the membrane is simulated as shown in Figure 3-5 with increasing frequency at 100-V bias voltage. The peak displacement indicates an immersion measurement frequency of 2.65 MHz, which shows agreement with both the measured data (shown in Figure 3-6) and lumped model calculation.

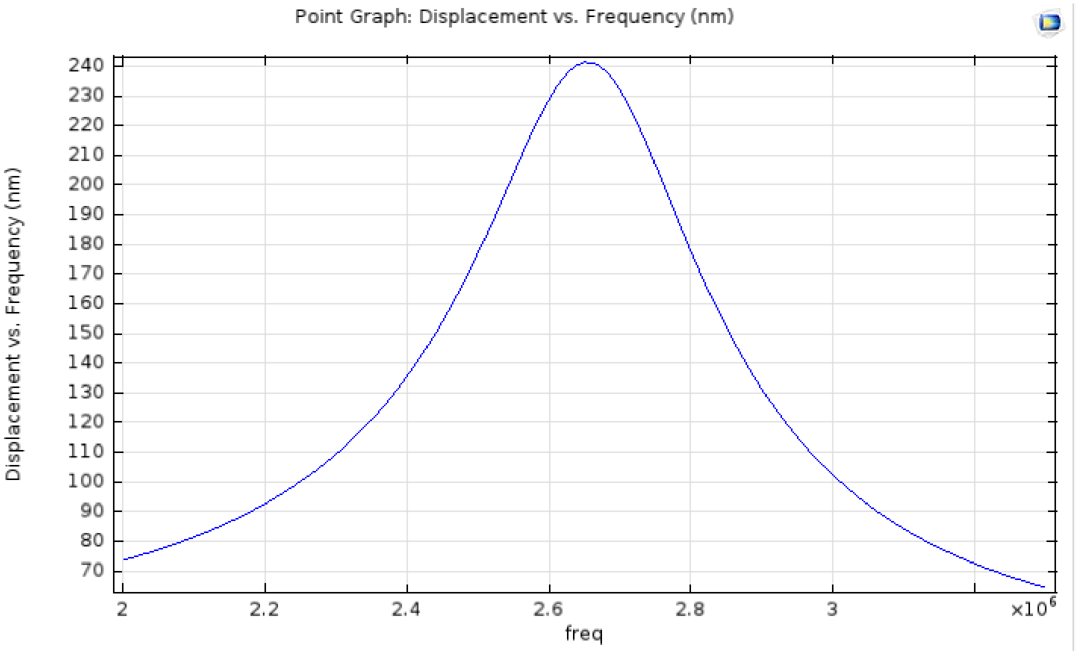

Figure 3-5: Simulated frequency vs. pressure in air with resonant frequency close to 9.1-MHz with.

With hydrophone measurement data, the pressure can be measured. And one can then deduce the displacement and verify it with the simulation. The element consists of 156 CMUT cells and has an aperture of 0.8mm by 0.8mm. To measure the pressure, the CMUTs are placed in vegetable oil with sound speed of 1540m/s. A hydrophone (Onda Corp., Sunnyvale, CA) is positioned in front of the aperture at 5mm away and the received electrical signal is amplified (AG-2010 pre-amplifier) before recording with an oscilloscope. The CMUT is driven with a customized pulsing circuit with a 60ns pulse width and a 30V unipolar pulse height.

Using the calibration data, the pressure can be calculated by dividing the voltage by sensitivity (450nV/Pa). The measured pressure can be compared with the 1-D model calculated far-field pressure, which is given as [3.4]

$$P_{piston} = \frac{\rho_0 c \pi {a_{eff}}^2 U}{2\lambda r} \qquad (3.15)$$

Where U is the velocity of the vibrating surface, and λ is the acoustic wave length, and r is the depth from the aperture. The single element contains 156 cells which can each be consider as a point source since each cell diameter is much less than the wavelength (60 µm:700µm). Hence, the combined pressure generated by the multiple cells, in the far field, is given as

$$P_{piston} = 156\frac{\rho_0 c \pi {a_{eff}}^2 U}{2\lambda r} \qquad (3.16)$$

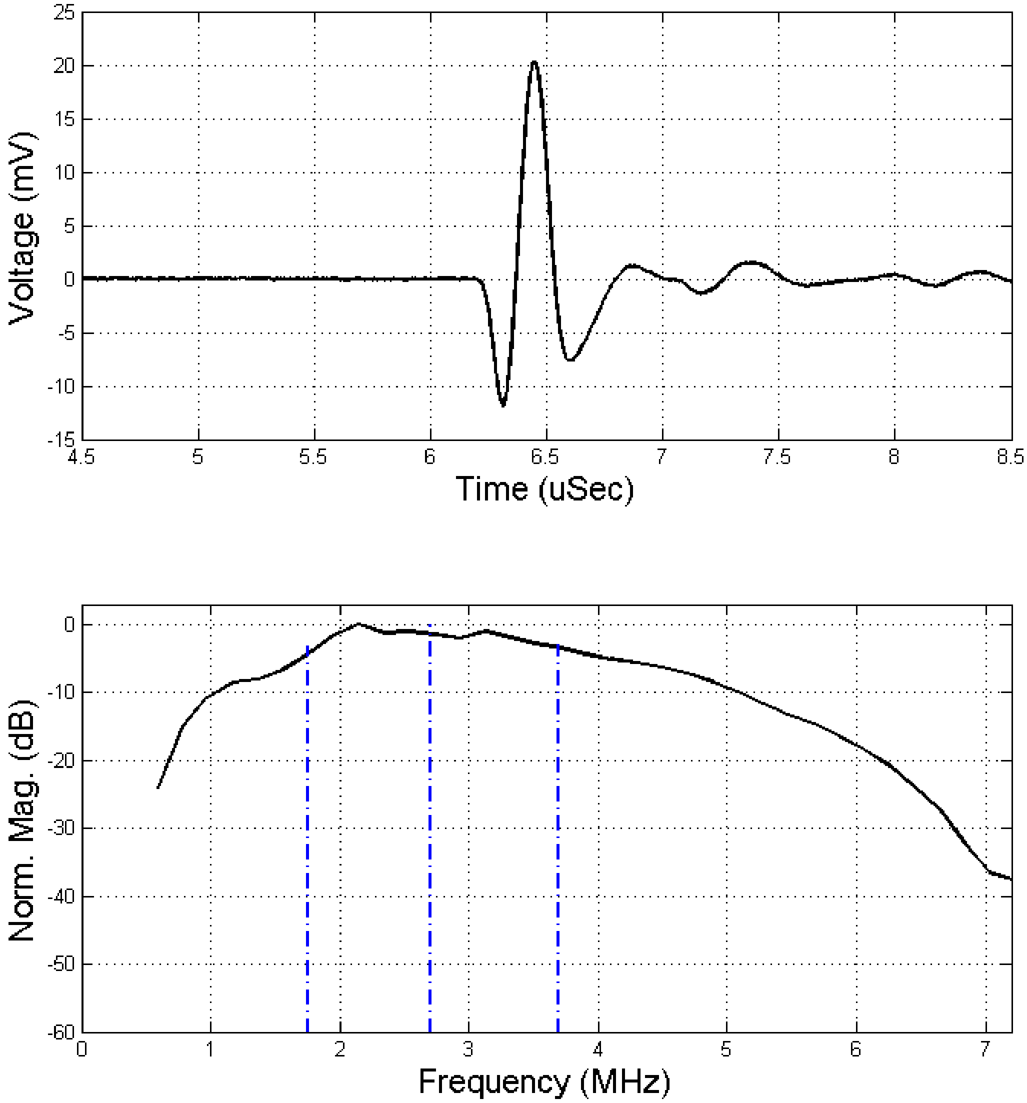

Figure 3-6: Hydrophone measurement of the single element.

3.4 Design and Fabrication

Given the similarities between a condenser microphone and a CMUT, one might wonder why the CMUT was not developed sooner. In fact, the main problem researchers faced was related one of the main CMUT design parameters, the depth of the cavity or gap height. In order to generate an electric field large enough for the CMUT to be useful and avoid damaging the device, a small gap height in the range of micro or nanometer is required. Thanks to the advances in micromachining technologies, such a small gap (<1µm) can now be easily achievable. When designing a CMUT, one should choose a small gap height to generate a large electrostatic force yet keep the bias voltage reasonable. On the other hand, the gap height should be large enough to allow room for the membrane to vibrate.

3.4.1 Membrane (Vibrating Plate):

The vibrating membrane diameter and thickness largely governs the frequency. The frequency is important because a higher frequency means a higher axial resolution in the resulting images. However, at higher frequency, the attenuation quickly increases thus reducing penetrability. The size of the CMUT membrane is usually in the micrometer range for typical medical ultrasound frequency, which is in the MHz range. In order to generate sufficient energy, many CMUT cells are connected in parallel to form an element. The shape of the CMUT membrane is another key factor to be considered. Square and hexagon shaped membranes were reported to produce the maximum fill-factor of the device; but circular membrane is most often used in CMUTs because it generates the lowest local stress [3.6]. The materials used to construct the membrane also affect the device performance. A stiff membrane results in a higher ultrasound frequency but takes more energy to vibrate. Silicon nitride and crystalline Silicon are two common materials for the CMUT membrane and dielectric layer. They are used because of their mechanical properties and the fact that they can be easily grown using standard fabrication processes. One of the most important CMUT fabrication step is the formation of the membrane on top of a vacuum cavity. Different methods were proposed to form the membranes on a vacuum cavity and they can be categorized into two types: surface micromachining and wafer bonding.

3.4.2 Surface micromachining CMUT fabrication

Surface micromachining involves depositing and etching the layers of the CMUT structure from the bottom to the top [3.1]~[3.3]. The cavity is initially occupied by a sacrificial layer, which is then removed upon the completion of the structure. A general method for making CMUTs through surface micromachining method, or sacrificial releasing method, is as shown in Figure 3-7. (a) First, an insulation is deposited; it also acts as an etch stop layer. (b) Next, a sacrificial layer is deposited. (c) Channels are etched define etch channels. (d) An additional layer of sacrificial layer is deposited to define membrane and cell cavities. (e) membrane material is deposited. (f) Release holes are etched to opened. (g) membrane is released by wet-etching of the sacrificial layer. (h) Etch holes are filled. Finally, (i) electrodes are deposited.

The surface micromachining process has several shortcomings. First, stiction often occurs given the high surface area to volume ratio of CMUT structures. The membranes can easily collapse on the cavity during release or drying process due to large capillary forces. Furthermore, the primary bottleneck for CMUTs to be widely adopted by the industry is its weaker output pressure. As such, the fill factor of a CMUT array is important. Surface micromachining, in particular, requires release holes for the removal process of the sacrificial layer and releasing the membrane.

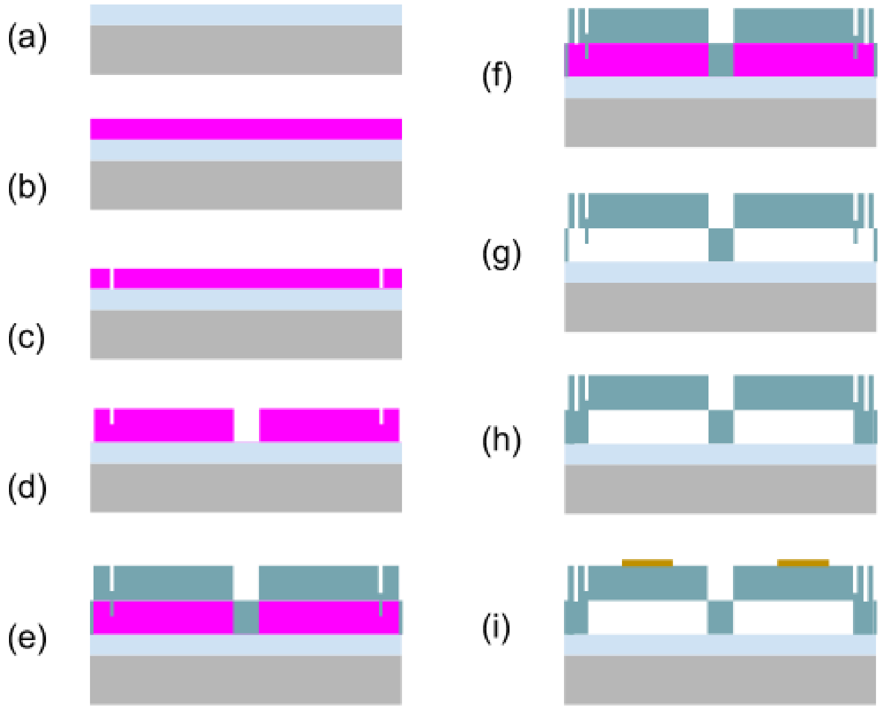

Figure 3-7: Basic process steps for the sacrificial release fabrication method.

3.4.3 Wafer Bonding Method

The second method, typically referred to as wafer bonding fabrication, involves fabricating the cavities/bottom electrode on one wafer and the membrane/top electrode on a second wafer [3.6]. The wafers are then bonded together with high force and elevated temperature. The fabrication process is shown in Figure 3-8. (a) First, an insulation layer is grown on a highly doped substrate. (b) cavities are then etched on the insulation layer. (c) A separate silicon-on-insulator (SOI) wafer is bonded together with the (b) wafer. (d) An etch-back process is done to release the substrate and buried-oxide (BOX) layer of the SOI wafer. (e) A two-step etching process is done to expose bottom substrate. (f) Metal electrodes are deposited. Because the cavities and membranes can be fabricated separately, it decouples design constraints so each structure can be optimized individually. With wafer bonding, sacrificial layers, and thus holes, are not required hence improving the fill-factor. Also, without the constraints of releasing, cavity depths can be made shallower which further improves electrical stability as actuation voltages can be reduced and insulating thickness can be increased instead. Furthermore, fabrication repeatability and controllability is generally better with the wafer bonding process as the number of lithography steps and masks are typically fewer.

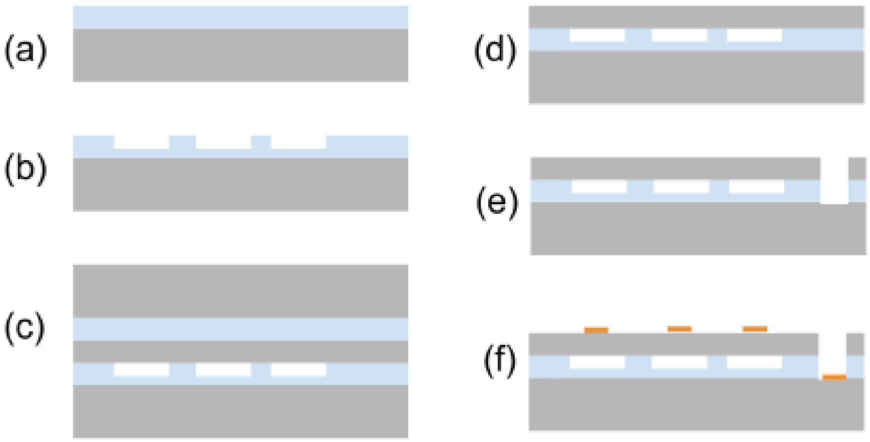

Figure 3-8: Wafer Bonding Process for CMUT fabrication.

3.4.4 Encapsulation

Since the membrane and top-electrode are susceptible to abrasion and can cause electrical short to nearby conductors, an encapsulation layer is required to protect the device. This layer should insulate the electrical components from the environment while complying with certain biocompatibility standards. More importantly, the insulating material should minimize any adverse impact on the CMUT's acoustic performance. In its working environment, an ideal encapsulating material will have a static Young's modulus low enough to allow the CMUT elements to pull in during DC excitation as well as a Young's modulus high enough to allow acoustic matching with water at ultrasonic frequencies.

The two most prevalent materials used for acoustic transducer encapsulation are Parylene and Polydimethylsiloxane (PDMS). Both of these materials meet the specifications necessary for electrical insulation and biocompatibility [3.7]. For coating, Parylene is vapor deposited whereas PDMS is spin-coated for thin layers and mold casted for thicker layers [3.7][3.14]. Thin coatings offer minimal acoustic impact but are also impractical for in vivo applications where the encapsulating coating will come in contact with ablative forces and should thus provide some degree of physical protection [3.8]. At the other extreme, thick coatings of PDMS can significantly hamper acoustic performance [3.8][3.9]. Other biocompatible silicone and polyurethane compounds exist for acoustic transducer encapsulation, but these are primarily used for acoustic lenses which require specific molding [3.10].

Several finite element models have been constructed to examine the acoustic performance of Parylene- and PDMS-encapsulated CMUTs [3.8, 3.11-14]. The primary issues uncovered by these models are acoustic crosstalk, loss of attenuation, and reflection at the coating-water interface. Overall, PDMS appears to be the preferred encapsulation compound due to its acoustic performance. Its thermal stability at elevated temperatures also makes it compatible with flip-chip bonding [3.15].

More recent research has examined the viscoelasticity of PDMS and its effects on acoustic performance [3.8]. In its working environment, an ideal encapsulating material will have a static Young's modulus low enough to allow the CMUT elements to pull in during DC excitation as well as a dynamic Young's modulus high enough to allow acoustic matching with water at ultrasonic frequencies. PDMS is found to share these characteristics, whereas Parylene is found to have too high of a static Young's modulus. In addition, this research demonstrates variation between the acoustic performance of different types of PDMS: a denser PDMS compound will provide better acoustic matching with water, but may also reduce the acoustic signal amplitude due to its increased mass load on the CMUT array.

3.5 Benefits

3.5.1 Wider-bandwidth

Compared to a PZT transducer, the vibrating membrane of a CMUT is substantially thinner. As a result, a CMUT experiences a much higher damping which leads to a wider bandwidth, or less *ringing*. Imagine if ringing effect was significant in our ears, we would be constantly hearing echoes and distorted sounds and be unable to appreciate a symphony. In short, it is extremely important to have a wider bandwidth in order to resolve spatially.

One reason PZT transducers are bulky, relative to CMUTs, is that the thickness of the crystal must be half-wave length of the vibrating frequency. So for medical imaging purposes, the thickness of the PZT is typically in the range of several hundred microns. Furthermore, an acoustic impedance matching layer is required. A structure's acoustic impedance is dependent on the material composite and also geometry. For any vibration energy to transfer efficiently between mediums, the impedance of the source medium should match the impedance of the medium of interest. An impedance mismatch creates inefficiency in the acoustic energy transfer and will introduce artefacts and heat. Although an impedance matching layer can be designed to minimize the inefficiency, any extra thickness will contribute to additional ringing effect. Last but not least, a backing layer is needed to absorb the acoustic energy that penetrates the PZT to prevent the penetrated acoustic wave from reflecting back to the transducer. Although this does not necessary weaken the bandwidth, it can reduce efficiency and also add bulkiness to the probe.

3.5.2 Smaller-pitch

In modern medical ultrasound imaging, an array of transducer elements is typically used instead of a single element. In Section 2.4, we discussed how phased array can be used to steer and focus the sound beam. Eliminating mechanical movements is beneficial but phased array introduces an important design constraint: in order to eliminate aliasing (also known as grating-lobes in ultrasound terminology) the *array pitch must be less than half of the operating wavelength.* The concept of grating-lobes is illustrated in Figure 3-9. When the elements are too far apart, constructive interference would happen too frequently. The centre red line indicates the primary lobe, where most of the acoustic energy is concentrated. The immediate lines neighbouring the primary lobe is called secondary lobes. If the secondary lobes are caused by pitch sizes, it is referred to as grating lobe. For a 90° sector scan, the pitch has to be within half-wavelength apart to ensure grating lobe is outside of the sector scan. For high frequency imaging, which is typically greater than 25 MHz, the pitch is required to be less than 30 μm. For PZT transducer fabrication, it is very difficult to achieve less than 40 μm in pitch due to the size of the dicing blade. In contrast, micrometer-level feature size can be easily achieved in microfabrication.

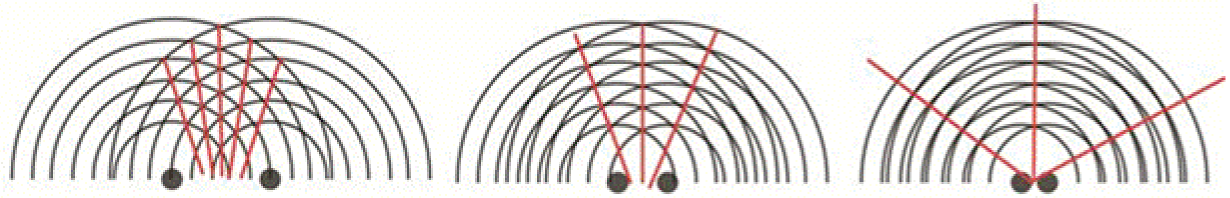

Figure 3-9: Pitch vs. Grating lobe effect.

3.5.3 IC integration

Most medical ultrasonic imaging systems can be broken down into four parts: the ultrasonic transducers, the front-end circuitry, the cable, and the back-end processing unit. Since the transducers are typically encased in a housing that is typically at least meter away from the processing unit, the raw signal received by the transducers can be significantly degraded due to parasitic effects. Therefore, receiver circuit, and sometimes the transmit circuit, is placed in close proximity to the transducers to maintain the signal integrity. Each transducer element has a dedicated transmitter and receiver circuit. The transmitter circuit sometimes includes a high-voltage switch to generate a large pulse, while the receiver includes an amplifier to enhance the measured signal.

It is difficult to package both the electronics and the high-density transducer array. Even though the complementary metal-oxide-semiconductor (CMOS) technology can provide tiny integrated circuits, it is still challenging to make the interconnections between individual elements and corresponding transmitter and receiver circuitry. Consider a large array with 128x128 transducer elements, over 16,000 interconnections are needed to address each element individually, meanwhile the pitch size is constrained by the frequency. In catheter applications, although the element count is not high, interfacing the electronics is still challenging given the tiny workable area of < 3mm diameter.

Traditionally, PZTs are diced into arrays with fine saws followed by the deposition of electrodes. The front-end components are fabricated separately and eventually soldered with the electrodes. However, at high densities and small surface areas, it becomes incredibly challenging to work with the traditional method. Thus, when the CMUT-on-CMOS process was demonstrated, it gave great hope to the future of ultrasound technology. Figure 3-10, Figure 3-11, Figure 3-12 shows some CMUT and CMOS integration techniques.

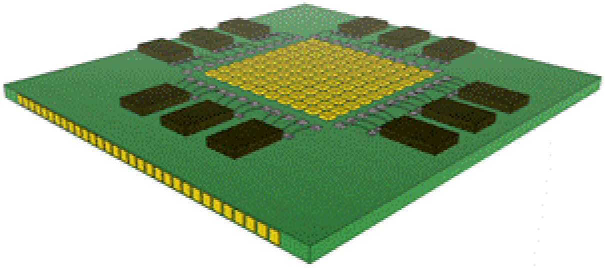

Figure 3-10: CMUT-in-CMOS refers to the process where CMUTs and CMOS are fabricated on a single wafer in parallel.

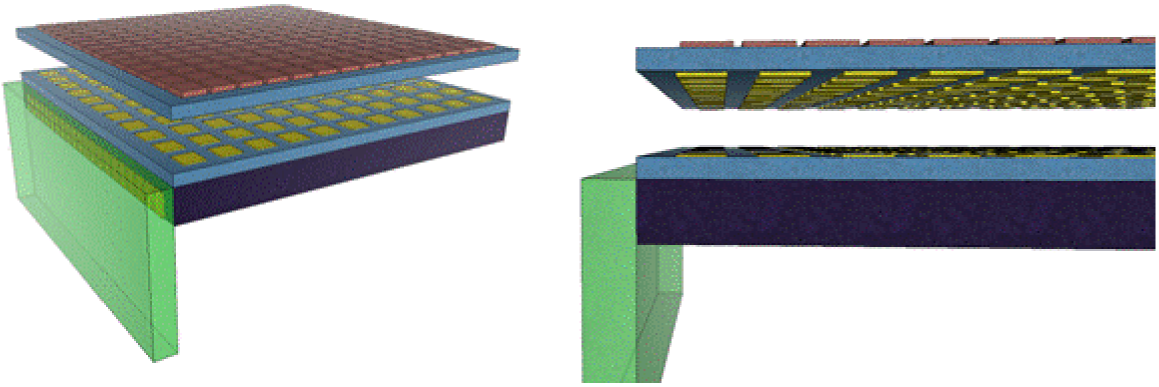

Figure 3-11: Flip-chip Integration: CMUT fabrication and CMOS process can be fabricated seperately

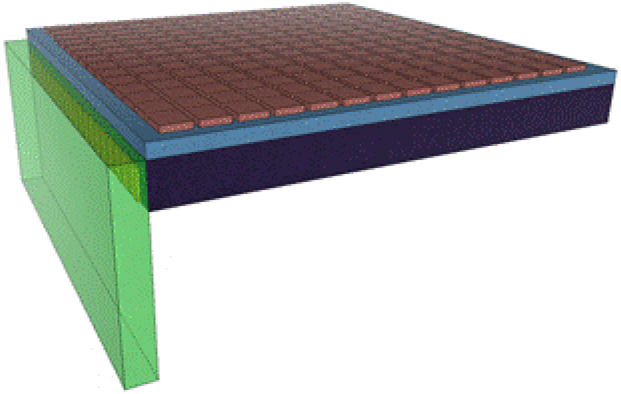

Figure 3-12: CMUTs can be built on-top of CMOS. This creates a very tight packaging.

3.6 Arrays

The advantages of CMUT have shaped the technology to evolve into two main branches in terms of medical imaging applications. The first branch of research revolves around in-vivo application where CMUTs are typically placed on the tip of catheters or endoscopes for intravascular/intracardiac-like ultrasound imaging. Within this branch, packaging and interface-engineering are the key factors in research. The second branch involves developing large and high density 2-D arrays to image large volumes, typically from outside the body. This second branch also closely couples with electronics simplification schemes. In this section, we will discuss the two branches, followed by the latest development in CMUT systems.

3.6.1 SMALL 1-D/Ring Array

Intravascular ultrasound/Intracardiac echocardiography (IVUS/ICE) imaging has been commercially available for over a decade. Angiography, the most widely used vascular imaging technique, cannot provide close-up anatomy of the lumen. By attaching ultrasonic transducers at the distal end of a catheter, the anatomy near the tip can be better perceived. Traditionally, IVUS and ICE have side-looking apertures; therefore, imaging is performed in the radial direction. In recent years, engineers have been trying to develop forward-looking IVUS catheters which provide much more useful information such as obstructions that occlude the blood vessel. Most of the methods involves a single piezoelectric transducer and some sort of mechanical actuators to redirect the sound beam. As discussed previously, mechanical actuation limits the frame rate and also introduces noise. In contrast, microfabrication means a high-frequency CMUT array can be easily placed at the face of the tip instead of around the tip, eliminating the need for mechanical movement during a scan. In fact, several research groups have demonstrated 1-D CMUT array for catheters. Some have even demonstrated a ring array where a hollow center is kept (see Figure 3-13Figure 3-12) for fitting an ablation device capable of burning the plaque that is occluding the vessels using high-intensity focused ultrasound (HIFU).

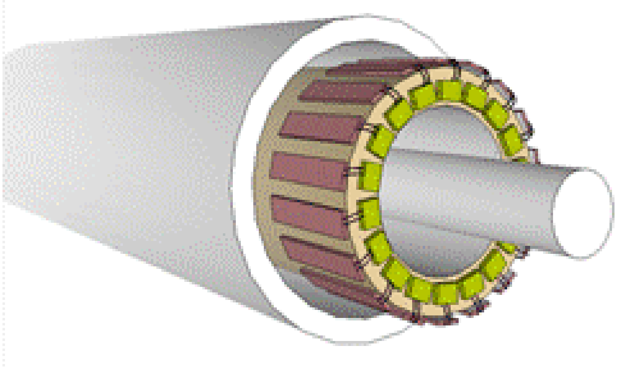

Figure 3-13: Ring array designs are very popular in IVUS applications since they allow a hollow center for guide wires or the possible integration of a thermal ablation tool.

The rate of growth of CMUT catheters has been quite noteworthy. The Edward L. Ginzton Laboratory of Stanford University and General Electric have recently reported in-vivo testing of a 9F (3mm in diameter) CMUT catheter [3.16]. The device contains a linear 24-

element array and has an imaging depth of penetration of around 30 mm. Using an ultrasound frequency of 8MHz, the CMUT catheter is capable of producing high-resolution real-time 2-D images. Real-time volumetric imaging, with a catheter-size 64-element CMUT ring array, has also been demonstrated by the same team [3.17] and shown in Figure 3-13. The research group from the Georgia Institute of Technology also reported a catheter-based CMUT system [3.18]. Their setup also features a forward looking ring array, but the main difference in their design is the use of CMUT-on-CMOS integration. The CMUT-on-CMOS approach reduces the parasitic capacitance of interconnects and eliminates a lot of wires, making it a very attractive option for CMUT catheter integration. Increasing the element count and the density of the transducer will result in a better signal-to-noise ratio and a better image resolution. However, as the element count increases, more front-end electronic components and cables are required. Given the current state-of-the-art interconnect and cabling solution, the number of elements that can be used on a catheter is currently still limited to 64 -elements.

3.6.2 LARGE/HIGH-DENSITY 2-D ARRAY

Large or High-density 2-D arrays are typically designed with the goal of imaging large volumes and/or achieving a high signal-to-noise ratio. Current 3D ultrasound applications include facilitating ultrasound-guided biopsy, screening for breast and rectal cancer, and also for prenatal imaging [3.19]~[3.21]. Currently, most of the large/high-density 2-D array CMUT research is conducted in parallel with solutions that simplifies the interfaces. Although the actual size of the array can vary from millimeters to centimeters, the element count can vary from 1,000 to more than 1,000,000. There are two main problems that arise from this: interfacing with a large quantity of elements and ensuring the amount of data can be processed in real-time. With the CMOS process, a large number of electronic circuits can be packaged into a single chip. However, at high ultrasound frequencies where the pitch size of the phased array is less than 25 μm, the area constraint placed on the electronic circuits becomes much more difficult to meet. Assuming that the area required by the electronic circuits can be small, cabling solutions that connect the probe to the processing system can only support a finite quantity of micro-coaxial cables (typically less than 128 lines) before the cable becomes too bulky and stiff. As a result, some kind of simplification scheme using multiplexing or simplified phased array algorithm is necessary. Some ongoing research techniques are briefly mentioned in the following.

3.6.3 *Sparse Array*

This simplification technique is based on an optimization problem whereby the least amount of transducer elements is used to recreate a sound beam that can otherwise be achieved by using all the elements. Depending on the array configuration, the acoustic field can be calculated by convoluting the acoustic responses of transmit aperture with that of the receive aperture. Sparse array researchers have come up with different sparse patterns to tackle the optimization problem. Several sparse array patterns are shown in Figure 3-14Figure 3-14. One obvious trade-off, however, is that with fewer elements, the signal-to-noise ratio decreases [3.22].

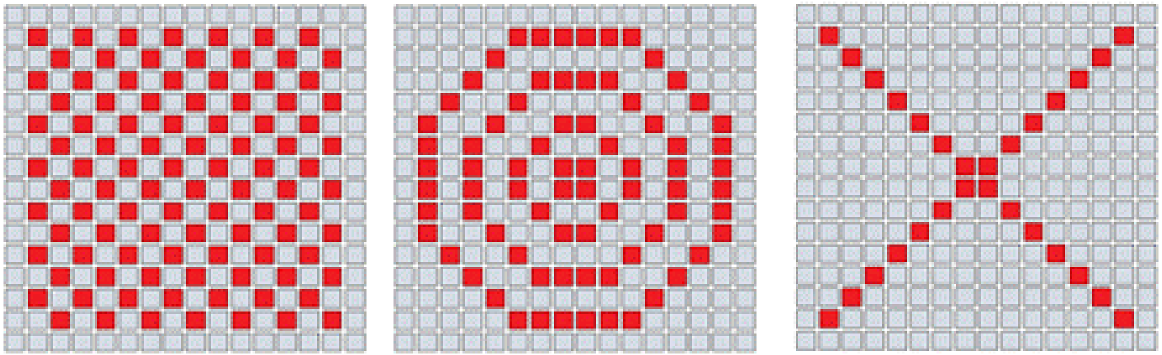

Figure 3-14: Some sparse array patters. Darker coloured pixels represent transmit elements and lighter pixels represent receive elements.

3.6.4 *Synthetic Array*

Synthetic array breaks down the transmit and/or receive aperture to sub-apertures at the cost of increasing the number of transmit/receive events. An analogy can be made where multiple low-resolution images are taken to form a high-resolution image. This technique is quite popular in high-speed blood-flow imaging. In this instance, a large data sample is stored and fast volumetric reconstruction is depicted using post-processing techniques. Since image quality is typically of prime concern over real-time to investigate diseases, synthetic array approach remains popular in 2-D arrays [3.23].

3.6.5 *Row-Column (AKA crossed electrodes)*

Row-Column (RC) focusing employs all elements to transmit and receive, and thus maintaining a signal-to-noise ratio comparable to that of a full-matrix phase-array method. In addition, only 2N leads, pulsers, amplifiers are used instead of N by N. This dramatically reduces the bulkiness of the system and makes the system extremely easy to implement. Also, the time it takes to complete a volume scan is comparable to a 1-D array. These three properties address all the shortcomings associated with the sparse and synthetic array. The RC method works by virtually rotating the aperture of an elongated 1-D array between transmit and receive events. Imagine a 1-D array overlaying another 1-D array at an orthogonal rotation about the center. As depicted in the Figure 3-15, each transducer is connected to a column bus on the top while connected to a row bus on the bottom. At transmit mode, a column of beam is focused at each event while at receive mode, the 2-D information containing the plane intersecting the column of beam and the aperture is received (Figure 3-16). This simplification scheme will be investigated in detail in the next chapter.

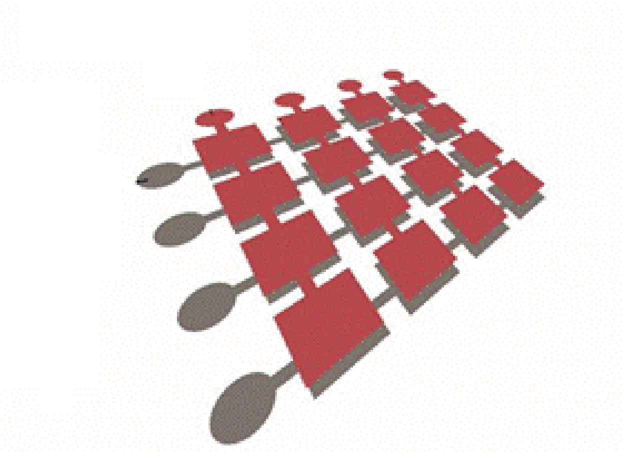

Figure 3-15: Row-column connection scheme. The top electrode are connected in columns while bottom are in rows.

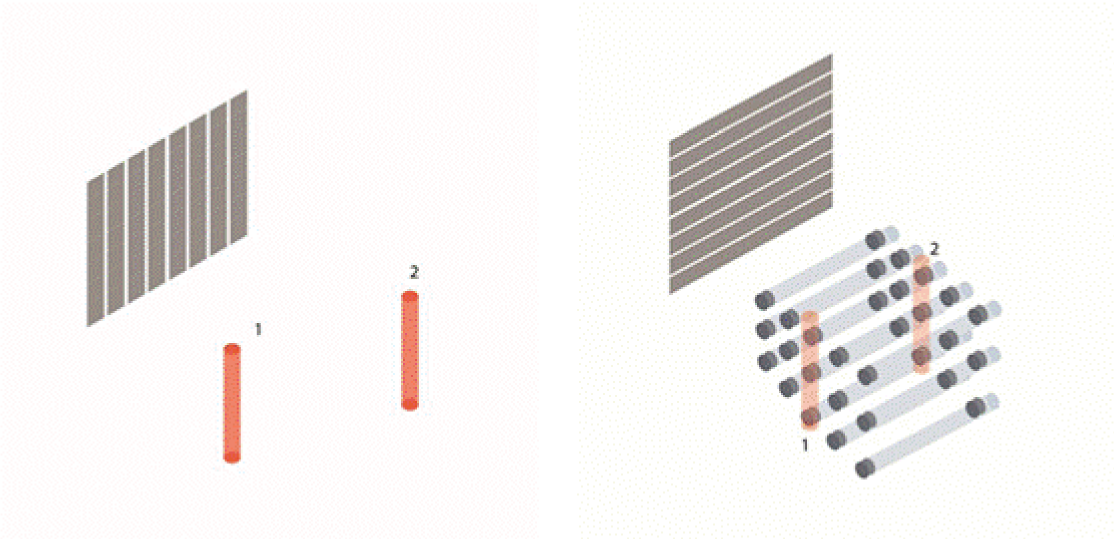

Figure 3-16: A single transmit column beam is formed at the transmit event. During receive event, a 2D section (dark pixels) are recorded.

3.7 Challenges

CMUT offers many benefits over the traditional PZT transducer, yet there are several challenges that the CMUT technology needs to overcome before it can be widely adopted. The weaker output pressure due to effective aperture and fill-factor, compared with PZTs, is already discussed. In addition, dielectric charging is also a well-known problem. When a large electric field is applied to the device, electric charges could get trapped in the insulating dielectric layer. The trapped charges create a shift in the CMUT internal electric field, causing the CMUT resonant frequency, and the resulting ultrasound frequency, to change. If different elements in a phased-array experience different frequency change, image quality will suffer. In addition, a shift in the electric field could reduce the CMUT efficiency or cause the device to collapse. Novel CMUT structures have been proposed to mitigate the dielectric charging [3.24], but more research still needs to be done in this area.

Another limitation of the CMUT technology is the cross-talk between transducer elements. Because all elements are situated on the same substrate, vibration of one element could spread to neighbouring elements. The result of the cross-talk is the degradation of image quality, because the unintended vibration of elements generates ultrasound that becomes noise. Models have been developed to help researchers understand the mechanism of cross-talk in CMUTs [3.25][3.26].

Perhaps the biggest obstacle that prevents CMUTs from achieving early success is the reliability of the CMUT device. Unlike PZT transducers that are rigid, CMUTs employ the vibration of thin membranes that can be easily damaged. Encapsulation layers have been used to protect the CMUTs, but there is always a trade-off between image quality and reliability, because while a thicker encapsulation layer provides a better protection, it reduces the efficiency of the CMUT. Fortunately, device longevity is not the biggest concern for catheter-based CMUTs because the catheter is discarded after each use. Therefore, one of the research objectives for catheter-based CMUTs is to minimize the manufacturing cost of the CMUTs and the associated front-end electronic circuits

Chapter 4 ROW-COLUMN BEAMFORMING

4.1 Revisiting Motivation

Given the powerful modern computation power, the frame-rate of medical ultrasound system is currently limited by the speed of sound. In a 1-D array case, a single pulse-echo event that generates a line-of-sight, or A-line, would take about the same time for the sound pulse to travel to the focusing point and back. As an example, if the sound were to travel for 10 cm in depth, it would take 10 cm ÷ 1540 m/s × 2 =130 µs. For a real-time frame rate of 20 frames-per-second (fps), this means an image must be created within 0.05 s. This yields 0.05 s ÷ 130 µs = 384 pulse-echo events, which can translate into several array/beamforming scenarios. For example, over 350 elements can be used to perform linear imaging although the number of channels would make cabling thick and not practical for a handheld operation. Most often, 128 elements are used and dynamic focusing can also be employed where multiple elements with fixed focus are used to scan linearly. In contrast to linear focusing, phased arrays are often used to image objects further away and of a larger focal depth. Since resolving power decreases away from the focus point, multiple focusing depths are used to improve the focusing at different depths. For example, if a 5cm~15cm depth, 90° imaging sector were to be scanned, a focusing depth of 7.5cm, 10cm, and 12.5 cm would be used with approximately 100 scan lines which can be done within the real-time frame rate.

An N×N 2-D array would be highly restricted by the frame-rate limitation. Given a 60°×60° scan volume and 384 pulse-echo events, one transmission would have to cover a 3°×3° volume which would yield a rather low resolution at 10cm focusing depth. This is why existing 3D imaging systems have very low frame rate. Another limitation in 2-D array is the bulkiness of the electrical addressing lines. If all the elements within a 2-D array are addressed individually, it would be extremely difficult to fabricate the interconnects and build the cabling lines. The size of the individual elements is determined largely by the wavelength of sound. As an example, medical imaging in the 5Mhz~10MHz range typically have elemental width around 150 µm. A 32×32 fully addressed, or full matrix, array would require over a thousand traces around or under the transducers. In theory, microfabrication can achieve submicron in trace width to overcome this problem although the process would be extremely costly with low yield. Typically, the ultrasound probe, which includes the transducer array and front-end circuit, and the computing system are connected by a cable assembly. Ultrasound cable design does not receive much glamour but can easily become the size bottleneck of an imaging system. Design concerns can include proper RF shielding, impedance matching, weight and size reduction, cable flexibility, ultras-high density coaxial, thermal management. With over a thousand elements to address, the physical connection from the transducer probe to the external computer would be massive as it would contain over a thousand micro-coaxial cable, which would demand a great amount of innovation and engineering itself. Also, the communication and signal processing resulting from thousands of channels would result in a very expensive and bulky system, therefore distancing the merits of using ultrasound imaging modality, which are fast, portable, and low-cost. In this chapter, we explain why row-column addressing is a practical solution to resolve many of the aforementioned problems associated with 2-D arrays.

4.2 Generalized Operation of RC-Array (Planar)

RC-array can be seen as a pair of stacked, orthogonal pair of elongated 1-D array. Although each of the orthogonal pair can be used as either transmit or receive aperture, the arrays are assigned as follows to avoid confusion: the array elements will run in the azimuth (x) direction during transmit and elevation (y) direction during receive as shown in Figure 4-1.

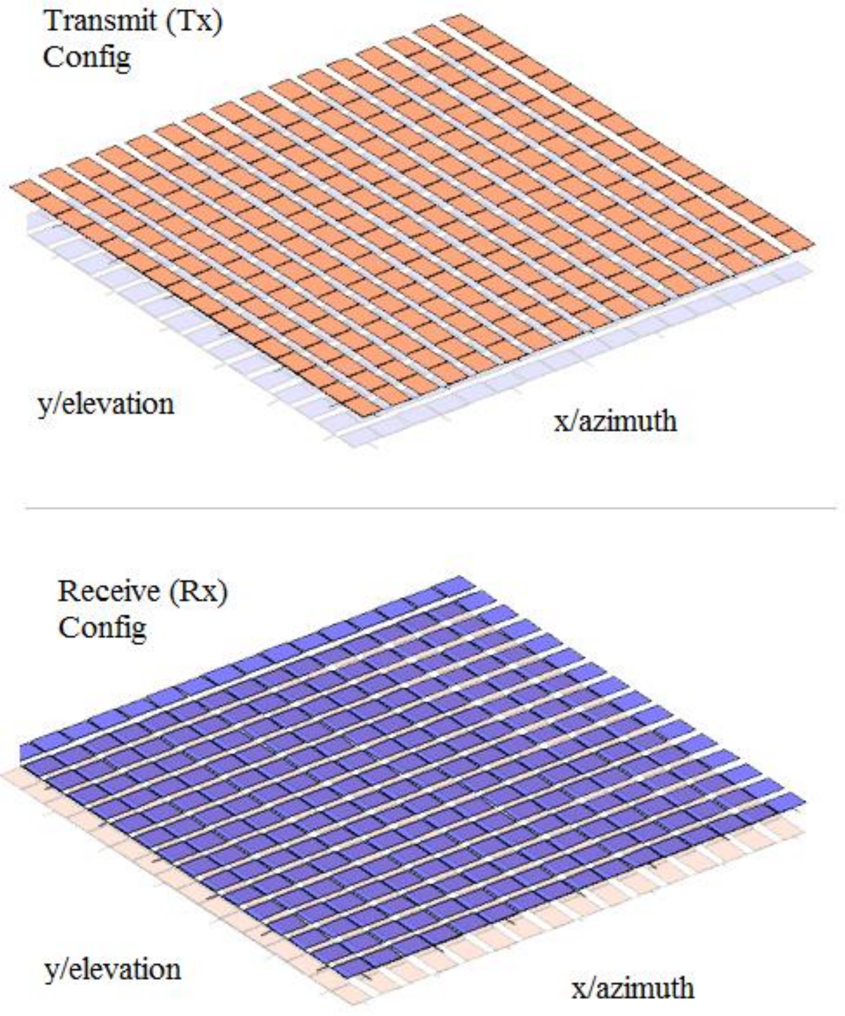

Figure 4-1: Row-Column addressing: transmit vs receive

A single transmit-receive event can result in a sector, or B-mode, image. First, a ‘line’ of focused ultrasound beam, which is focused by a subset of the transmit array, is transmitted as depicted in Figure 4-2. Steering can be done in the azimuth direction and a y-direction elongated beam can be created. For the corresponding receive event, the elements composed of row-line elements can receive-beamform in the elevation direction. The received signal from each channel can then be processed to reconstruct a B-mode image. This transmit-receive event can be iterated in the azimuth direction to achieve a volumetric scan.

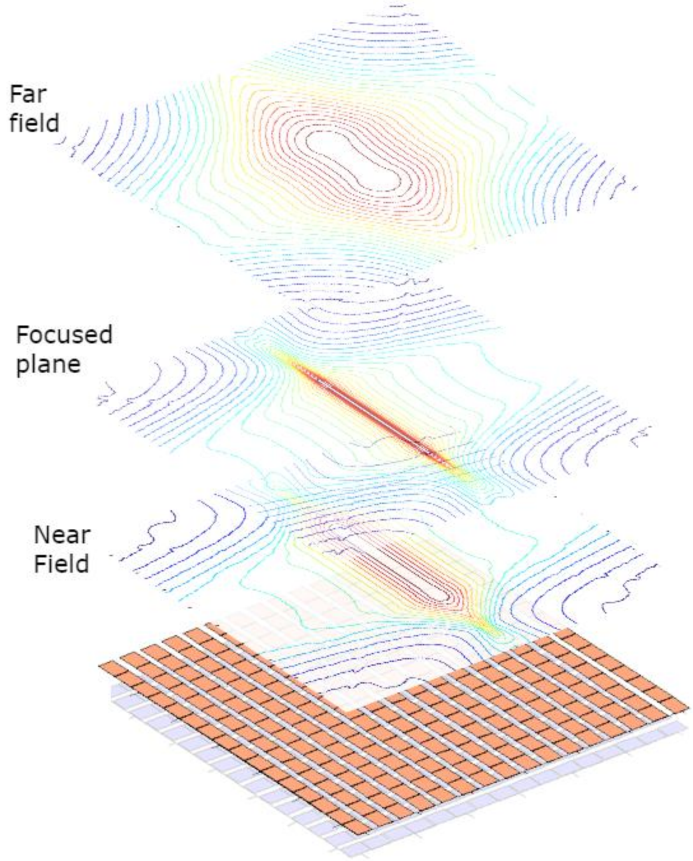

Figure 4-2: Transmit focusing using RC array

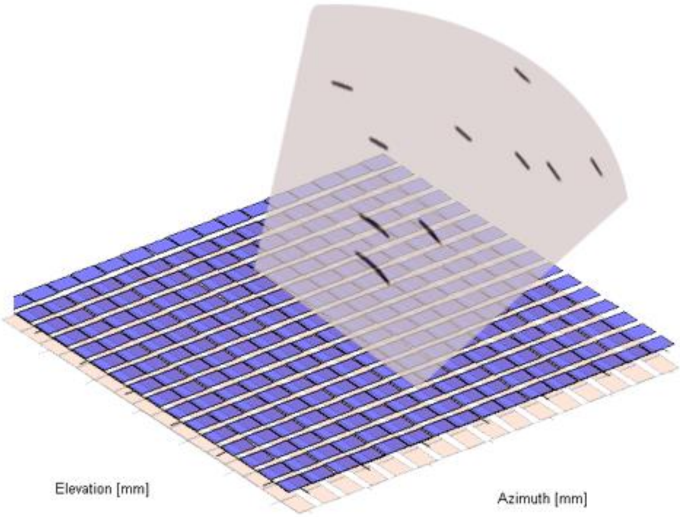

Figure 4-3: For each transmit event, a 2-D scan information can be reconstructed in the elevation and depth direction.

4.3 Fabrication of Row-Column CMUTs

Row-column CMUTs can be fabricated using the wafer-bonding process. The process is an extension based on the 1-D CMUT array wafer bonding process presented in Section 3.4.3. The RC-CMUT fabrication process can be separated into three phases as indicated in Figure 4-4. The first phase involves patterning the bottom wafer. The second phase is the wafer bonding process. The third phase involves patterning and adding electrodes to the top layer. (1) An oxide insulating layer is grown on the device layer of an SOI wafer. (2) Trenches are etched through to the BOX layer to separate the row electrodes. (3) Cavities are etched into the insulation layer. (4) The two SOIs are brought into contact followed by (5) etching the handling wafer. Since the bottom SOI has oxide grown on both sides, the back side of the bottom handling layer is protected against the etching solution. (6) The BOX layer is removed using hydrofluoric (HF) acid. (7) The top device layer is etched through to isolate column elements and to expose the oxide layer for the subsequent (8) bottom electrode exposure. (9) Metal electrode pads are added. The detail fabrication process for the RC-CMUT fabricated will be presented in Section 6.4.

It is important that the oxide layer in Step 1 is free of any contamination as dielectric breakdown is a common problem in CMUT fabrication. Failures are often associated with furnaces that are contaminated with metal ions. The oxide furnace used should be exclusively prepared for oxide and only oxide growth. Cleaning process is also extremely important and will be presented in Chapter 7. Step 2 and 7 can be tricky as long and narrow trenches are required. Contamination or photoresist irregularities can easily prevent proper etching which result in improper electrical isolation and inter-elemental electrical shorts. Phase II is typically the most sensitive to fabrication failure as any small contamination can cause the wafers debond and unusable. The bonding failures will be discussed in detail in Chapter 7.

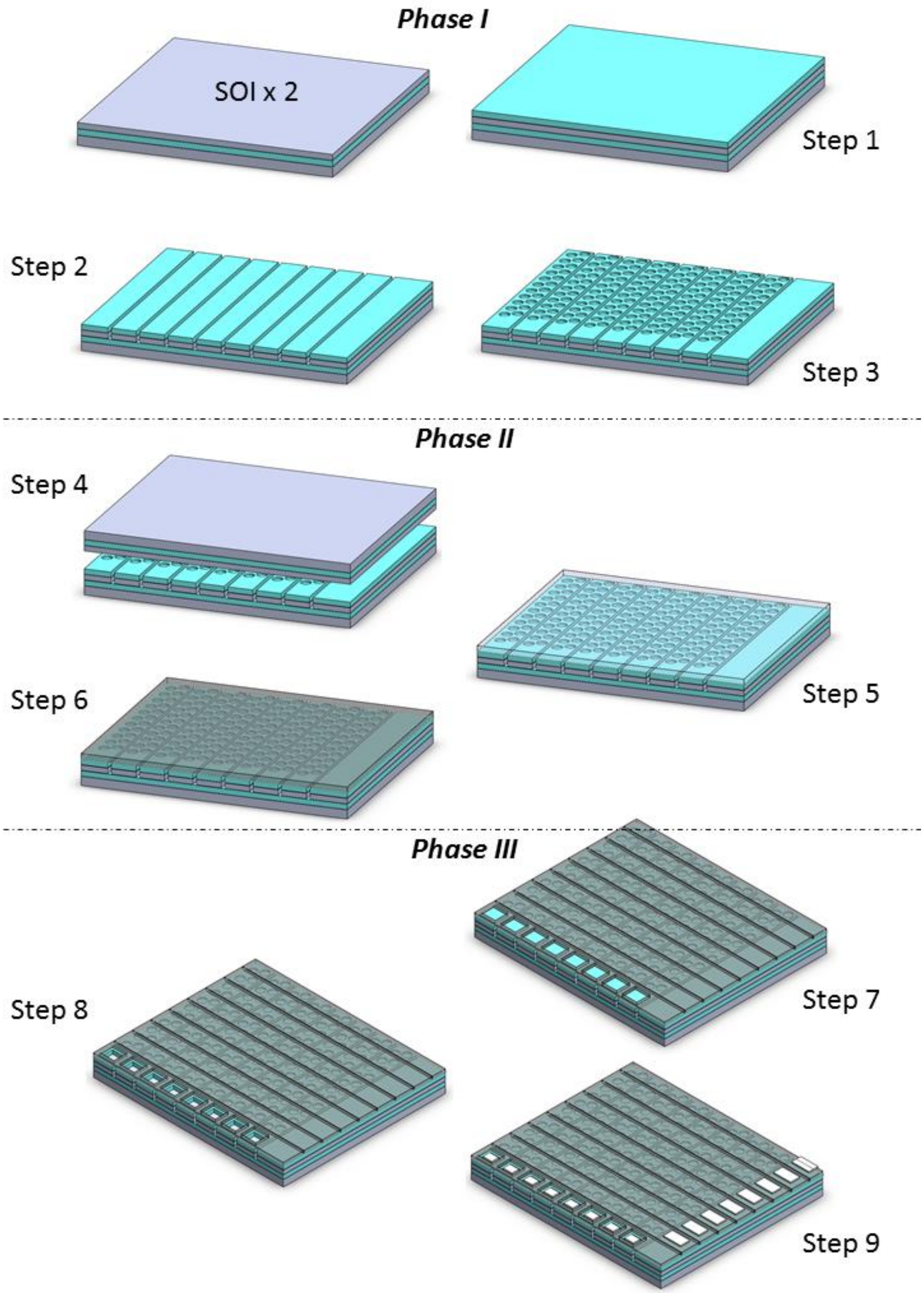

Figure 4-4: Fabrication of RC-CMUT array

4.4 Literature Review

Prior to the proposed imaging method, ultrasound scientists had spent years looking for ways to improve transmit power and resolution of simplified 2-D arrays. Since the inception, the RC-array technology has seen from a theoretical proposal and simulation works to a fully integrated imaging system.

2003

The concept of using row-column array, also known as *crossed-electrodes* and *top-orthogonal-bottom-electrode* (TOBE) array, for 3-D imaging was first proposed by Morton and Lockwood (Queen's University) in 2003 [4.1]. Soon after, Daher and Yen from the University of Southern California (USC) investigated row-column addressed 2-D arrays for synthetic imaging [4.2][4.3]. This study modelled various combinations of columns and rows as transmit and receive aperture to optimize image quality for real-time 3-D imaging. The reported transducer array is essentially a 1-3 composite with horizontal and vertical electrodes on the top and bottom.

2009

A few years later, the first CMUT implementation of an RC array was presented. Logan *et al.* from the University of Waterloo (U of W) reported the fabrication of RC-CMUT array using a novel CMUT fabrication process that involves a nitride-to-nitride wafer-bonding technique to achieve higher quality CMUTs [4.4]. Concurrently, Awad and Yen (USC) reported a 3-D spatial compounding scheme suitable for row-column array [4.5]. Seo and Yen (USC) from the same group built and reported the experimental results from a 5-MHz, 256 × 256 row-column array based on piezoelectric crystal [4.6]. The aperture size was 38 mm × 38 mm and B-scan and C-scans were provided for an 8-mm diameter cylindrical anechoic cyst phantom. The array is constructed with a dual-layer of perpendicular 1-D piezoelectric transducer arrays. The imaging is done by recording each channel across 256 rows which resulted in a very long and tedious recording time (>200hrs). Meanwhile, Demore *et al* (Queen's University) presented a study that compared the transmit power and resolution between RC-array and a fully addressed 2-D array [4.7]. In this study, it was determined that RC beamforming increases the transmit intensity as it doubles the imaging aperture when compared with a conventional two dimensional array with the same element count which balances the loss in signal-to-noise and resolution that would otherwise accompany this imaging technique. This argument will be revisited in the next section. The same study also did acoustic simulation on a spherical row-column array and presented B-mode images. However, as fabricating a curved array is difficult, a spherical RC array has yet been realized.

2011

Zemp *et al.* from the University of Alberta (U of A) fabricated an RC-CMUT array using a sacrificial CMUT fabrication process. The emphasis along with the fabrication method was to produce a ground top-electrode which is beneficial for patient safety. In the same year, Logan *et al.* demonstrated volumetric imaging with the RC-CMUT array. Since CMUTs require biasing, the row-column array can perform dynamic focusing by toggling and controlling the number of active rows. As a result, near-field depth can be controlled without the use of a lens. The transducer has a center frequency of 5.9 MHz and a relative bandwidth of 110%.

2013

Two years later, Zemp *et al*. modified the fabrication process to incorporate SOI wafers and used the RC-array for photoacoustic imaging [4.10]. Furthermore, they adopted rectilinear scanning and also incorporated S-sequence aperture encoding to improve signal-to-noise without adding additional imaging time. Christiansen *et al.* from the Technical University of Denmark (DTU) fabricated a RC CMUT array with an open-grid support structure which used a double-SOI wafer-bonding process [4.11]. The open-grid design was investigated as it may lead to a highly insulating post structure. Although it did deliver better breakdown voltage, the open grid support structure for the membrane is not ideally rigid and does not offer good clamping of the vibrating membrane.

2014

Later, Sampaleanu *et al.* (U of A) reported another operation scheme for imaging with RC-array [4.12]. The front-end circuit is set-up in such a way that it can achieve single-element actuation to provide 2-way transmit focusing, thus improving resolution and side lobe suppression – however, this is at the cost of an increased number (N^2) of transmit event. Chee *et al.* (U of A) demonstrated the first 3-D photoacoustic imaging with RC-array using N laser pulses and N receive channels [4.13]. By moving smaller aperture in two translational axes, a hair phantom was imaged at high-resolution images. Meanwhile, Christiansen *et al.* (DTU) found that the elongated elements in RC-array impose a noticeable edge effect which can cause ghost artefacts [4.14]. These edge effects can be reduced by implementing an integrated apodization design while fabricating the CMUT arrays. The first non-destructive testing application for RC-arrays was demonstrated by Wong *et al.* (U of W) and the efficacy of using RC-array for surface scanning was presented [4.15].

2015

As mentioned, edge effects of RC-arrays can lower the image quality, software compensation schemes are also of interest. As the PSF of RC beamforming is highly spatially dependent, Ben Daya *et al.* used the Fisher Tippett Multilayered Conditional Random Field Model [4.16] to correct the artefacts. The approach incorporates a reconstruction framework that compensates for the intrinsic limitations of row-column. The use of multilayered conditional random fields (MCRF) to account for data sparsity, speckle noise, and a spatialy varying PSF with inherent ghosting artifacts has shown promising results. This improved image reconstruction algorithm outperforms the previously published system when evaluated with metrics such as peak signal to noise ratio, coefficient of correlation, and effective number of looks. Christiansen et al. (DTU) built a 62 × 62 element, 26.3 mm × 26.3 mm array with custom front-electronics that interfaces with a commercial medical imaging system [4.17]. Rasmussen *et al.* (DTU) gave a more accurate beamforming method to account for the elongated element [4.18]. It is geometrically corrected such that distortion due to traditional point-source based time-of-flight calculation is avoided. Detail modelling and simulation results were given to characterize the ghost effect in the point spread function caused by edge waves. In the same year, Bouzari *et al.* applied spatial matched filter beamforming on RC-array and increased spatial resolution since the traditional delay-and-sum beamforming are limited by the aperture size and by the operating frequency [4.19]. Engholm *et al.* implanted the same RC-array design into a hand-held probe with clinical-grade features and demonstrated a volume scan [4.20]. In addition, the acoustical cross-talk in the RC array was investigated by Christiansen *et al.* and it was found that element-to-element cross-talk can be reduced significantly given the orthogonal operation [4.21].

2016

Bouzari *et al.* (DTU) revisited piezoelectric RC-array and performed volumetric synthetic aperture imaging. The system boasts a volume rate of 90 Hz (Single element transmit events) down to 14 cm deep [4.22]. The array they used were 3-MHz, half-wave length pitch, 62 + 62 element piezoelectric RC array. The RC array was well packaged for clinical testing and was designed to be driven by the experimental ultrasound scanner SARUS.

4.5 Row-column resolution vs. Full-Matrix operation

As discussed in 4.1, using a full-matrix 2-D array for real-time volumetric imaging is impractical due to sound speed limitation. Yet, full-matrix can still be treated as the golden standard for 2-D array imaging. In this chapter, the widely accepted comparison of row-column imaging and full-matrix array is presented. From a practical operation standpoint, the number of addressing element is limited to 256 channels. At the same time, a larger array aperture is typically desired if resolution is of great importance. Transmitting power is also directly proportional to the aperture size. A larger array leads to improved resolution, which can be derived using the Fresnel approximation. In this section, this approximation will be used to understand the image performance of row-column imaging.

The Fresnel approximation states that in the far field of the aperture, or in this case the transducer array, the pressure field may be described by the Fourier transform of the transducer aperture. To describe the pressure field of an aperture, a simple *rect* function can be used to describe the aperture's function spatially. The pressure field of the aperture can be described by the Fourier transform of the *rect* function, which results in a *sinc* function. The transmit aperture of the RC-array is simply a 1-D array with elongated element in the elevation direction. The pressure field at depth z can be described as,

$$P_{x,one-way} = \mathcal{F}\{A\} = \frac{L_x\sqrt{\rho_a}}{\sqrt{\lambda z}} sinc\left(\frac{L_x x}{\lambda z}\right) \tag{4.1}$$

Where L_x denotes the size of the array along the x-dimension, the size of this array in the x-direction Lx, ρ_a denotes the mass density of the medium, and $\mathcal{F}\{A\}$ denotes the Fouirer transform of the aperture *A*. The FWHM of the corresponding sinc function is

$$FWHM_{one-way} = \frac{1.2\lambda z}{L_x} = 1.21\lambda f\# \tag{4.2}$$

Consequently, the lateral resolution is proportional to the array size. Equation 4.2 describes the one-way focusing lateral profile of an aperture for either transmit or receive. It is important to realize that since transmit and receive focusing for RC-arrays are done orthogonally, the FWHM is only as good as a 1-D array and also limited by Equation 4.2. In other words, transmit focusing is done only in the azimuth direction while the receive focusing is done only in the elevation direction. The 3-D focusing spot-size is therefore, the overlap of the transmit azimuth and receive elevation focusing. In contrast, full-matrix arrays can perform focusing in both directions during both transmit and receive. Therefore, the pulse-echo field along one dimension is describe by

$$P_{x,one-way} \propto \mathcal{F}\{A * A\} = \mathcal{F}\{A\}\mathcal{F}\{A\} = (\mathcal{F}\{A\})^2 \qquad (4.3)$$

and subsequently,

$$FWHM_{two-way} = \frac{0.89\lambda z}{L_x} = 0.89\lambda f\# \qquad (4.4)$$

So ratio, in terms of resolution, of RC-array and full-matrix is

$$\frac{FWHM_{one-way}}{FWHM_{two-way}} = \frac{1.21\lambda f\#}{0.89\lambda f\#} = 1.36 \qquad (4.5)$$

Equation 4.5 explains that for the same aperture size, the FWHM of an RC-array is 36% larger than that of a full-matrix array with two-way focusing. If a FWHM is fixed, an RC-array should be 36% larger than that of a full-matrix array.

4.6 A graphical look at RC beamforming

Modeling of RC CMUTs is done to aid in verifying the imaging performance of the presented system. In particular, the resolution and field of view are investigated through simulations of radiation patterns and wire target imaging. A 5.9-MHz, 32 × 32 elements (4.8mm × 4.8mm) transducer array is modeled using Field II. To simulate the transducer, a 1-D linear array is used to transmit and focus in the azimuth direction. Kerf, element width, and element height are set to 0.03mm, 0.12mm, and 4.8mm, respectively, to mimic the actual RC-CMUT layout. Sub-element count is configured to 3 in the x-direction (i.e. azimuth) and 20 in the y-direction (i.e. elevation) in order increase accuracy. The same configuration is used to model receive aperture, except the 1-D array is rotated orthogonally. A single cycle sinusoidal pulse with a center frequency of 5.9MHz excites the transducers. Phased-array focusing is done to focus 5-mm away from the aperture on the center axis. The one-way radiation pattern was generated by finding the maximum value of the demodulated signal detected by an ideal point receiver scanned at a plane that is parallel to the aperture at a distance of 5 mm. Figure 4-5 shows the one-way transmit beam profile. As expected, the simulated focused beam is elongated in the elevation direction, as shown in Figure 4-5. The 4.8mm aperture height yields a -3dB beam with height and width of 3.1mm and 1.3mm respectively. The -6dB beam height and width are calculated to be 4.5mm and 1.6mm. The range secondary lobe is approximately 40dB below the peak. For a larger aperture size, we would expect to see improvements in the height-to-width ratio of the beam.

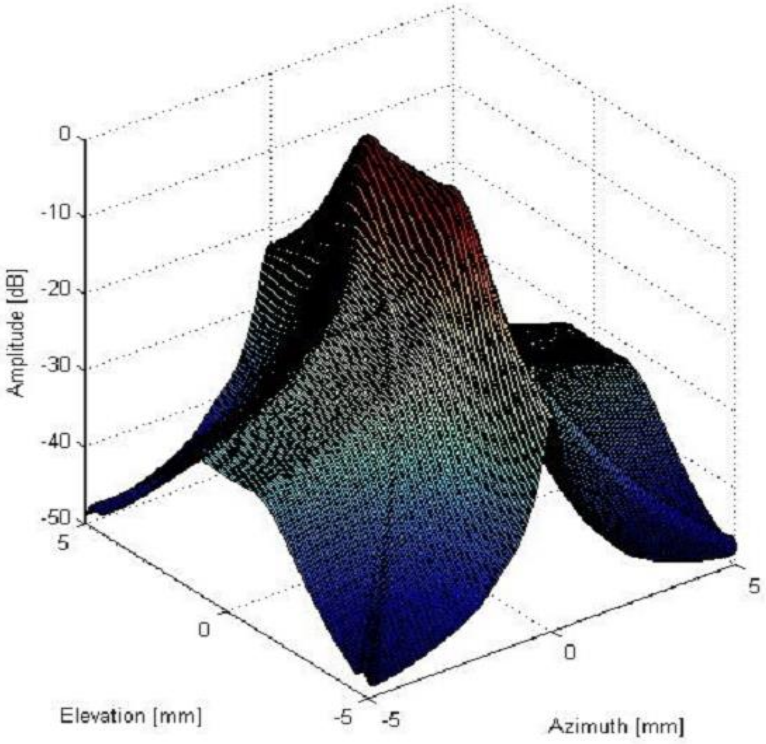

Figure 4-5: Transmit (one-way) acoustic field

The simulated aperture has a size of 4.8mm height by 4.8 mm width, 5.9-MHz centre frequency, 32 by 32 elements, half wave-length pitch, and a focusing depth of 5mm. Dynamic range is set to 80dB and no apodization is used. The two-way on-axis pattern, or the point spread function (PSF), is merely a convolution of two orthogonal one ways spatial function and is shown in Figure 4-6.

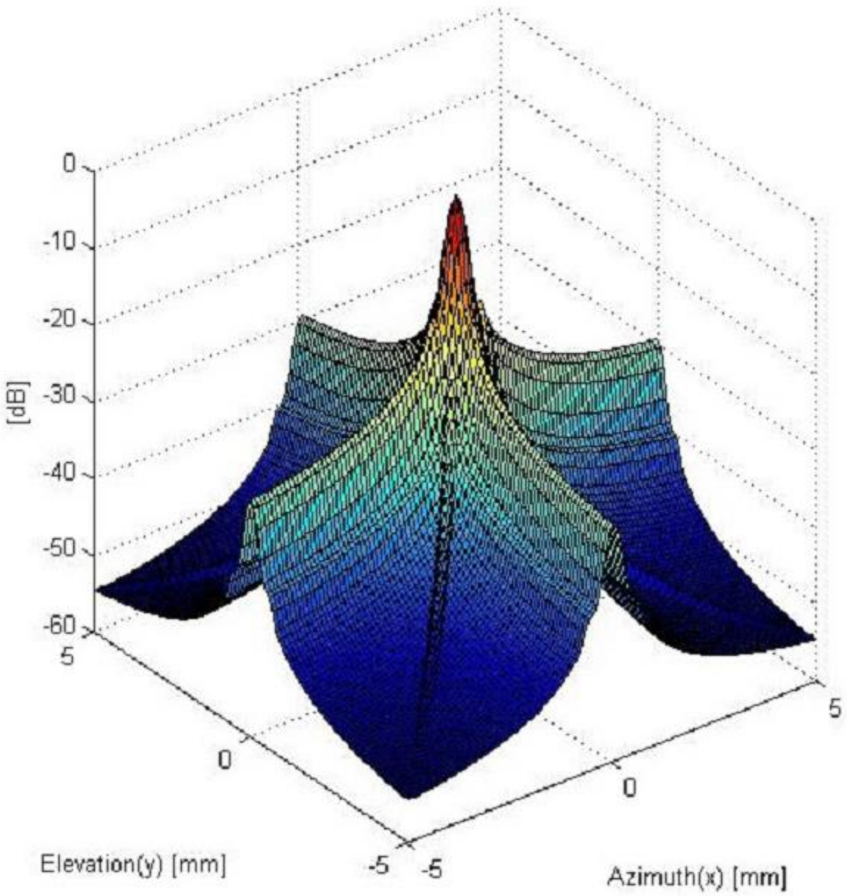

Figure 4-6: Two-way beam profile (PSF)

If we assign the one-way radiation pattern in Figure 4-5 to be that of the transmit focus (the orthogonal pattern would correspond to receive focus), one may be able to observe that natural focusing controls the height of the beam in the elevation direction. This factor is extremely important to understand because the effective scanning volume is highly limited by the aperture size. Since a PSF can be viewed as the orthogonal pixel multiplication of the radiation pattern, once the point-of-interest is outside of the natural focusing height, a weak radiation pressure will result due to the multiplication with the weaker point of the one-way beam. Figure 4-6 illustrates three scatterers being place at [0,0,5]mm, [-1,-1,5]mm, and [3,3,5]mm at a focal plane 5-mm parallel to the aperture. The latter scatterer, which is outside the aperture height has a much weaker PSF compared to the scatterers within aperture height and width.

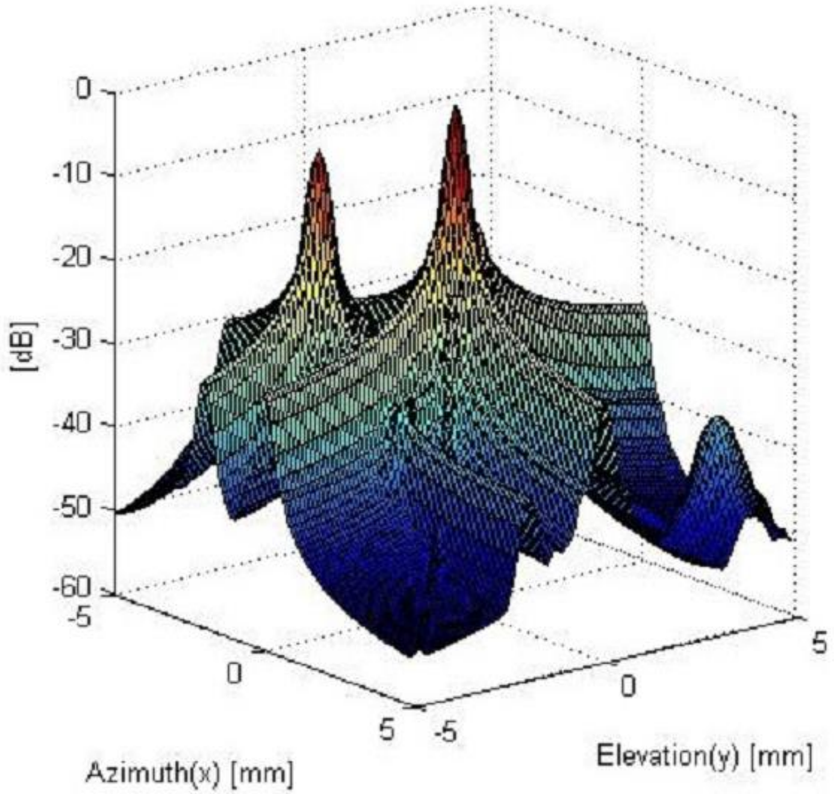

Figure 4-7: Pulse echo response of three scatters located at on axis, [-1,-1]mm off axis, and also [3,3] mm off axis are presented here. Aperture size is 4.8 mm and focusing depth if 5 mm. The off-axis peaks are approimately 6-dB and 36-dB below the center peak.

Reliance on natural focusing also introduces another problem. During transmit, the elevation profile will start narrowing. Figure 4-8 illustrate a two-way diagram where point scatterers are placed 0.5-mm apart across the y-axis focused at 2.5-mm away from the aperture. At 5-mm away, the contrast decreases as expected since the sound beam will experience defocusing as a function of distance as seen in Figure 4-9. At 10-mm away, the 5 points become indistinguishable in Figure 4-10 as PSF simulation resulted in a -6dB spot size of 1.3-mm in diameter. If a 1-mm resolution threshold is desired for imaging using a 4.8-mm by 4.8-mm RC array, the scanning volume would be roughly 5 mm by 5 mm by 10 mm. One potential action for improving the mentioned RC array is to design a curved array such as the one described by Demore et al [4.7].

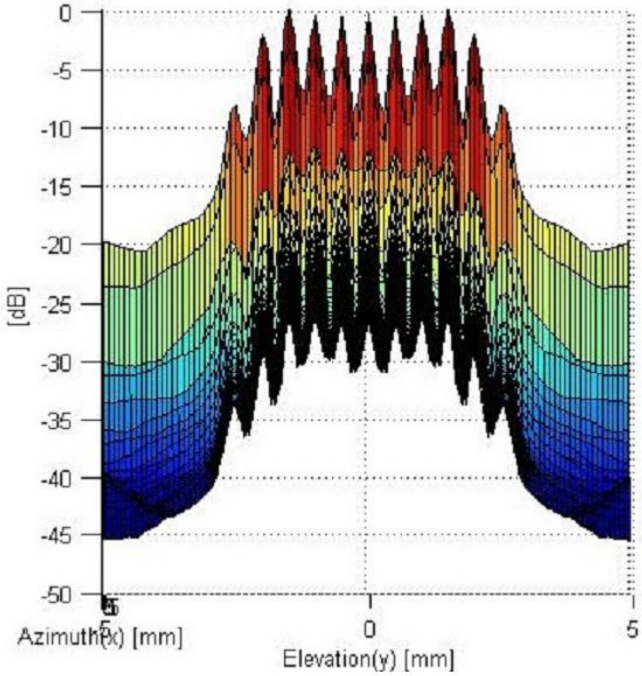

Figure 4-8: 2.5 mm depth focusing of scatterers distributed 0.5 mm apart parallel to the y-axis.

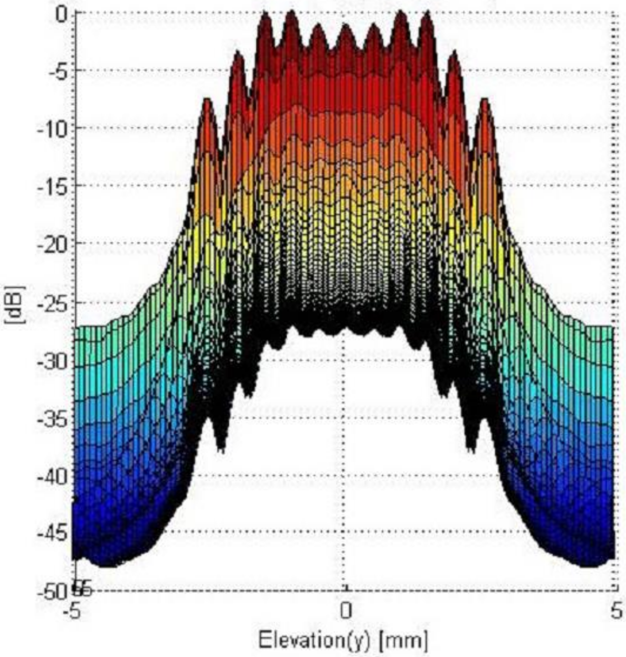

Figure 4-9: 5 mm depth focusing of scatterers distributed 0.5mm apart parallel to the y-axis

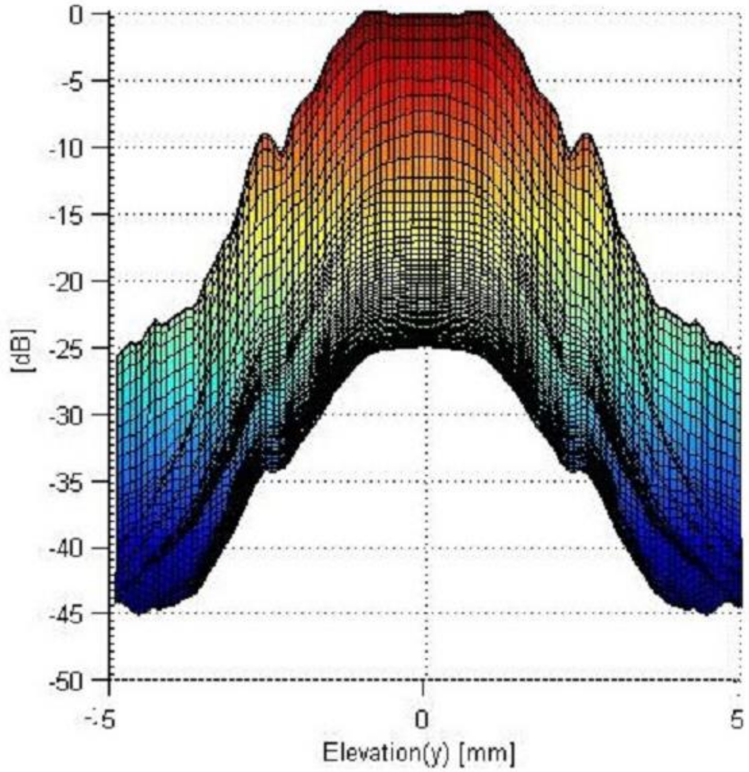

Figure 4-10: 10 mm depth focusing of scatterers distributed 0.5mm apart parallel to the y-axis

4.7 Limitations of RC Focusing

The general operation of RC beamforming may sound like a lucrative choice for volumetric scan since a complete volume scan can be acquired at a 1-D array scanning rate. However, there exists several shortcomings that stems from the use of elongated elements. First, at the two edges of the focused line wave can cause apparent ghost effects. Figure 4-11 shows a simulated pressure profile of the RC-array. The edges of the elongated elements contribute to a higher pressure concentration at each side which produces side lobes in the elevation direction.

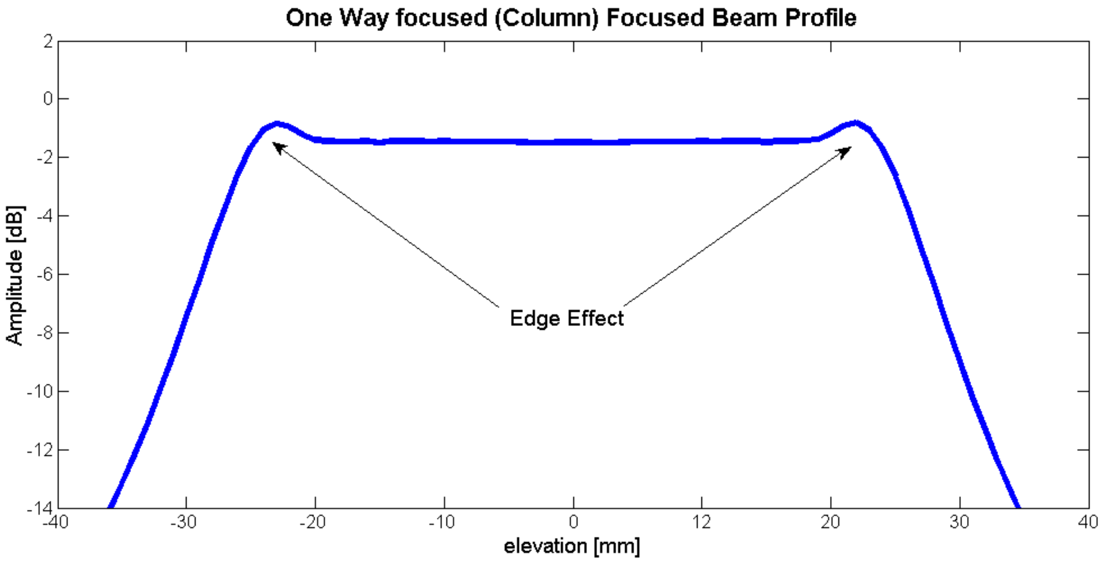

Figure 4-11: Edge effects of RC-Arrays

The sidelobes can result in artefacts in the reconstructed image and this ghost effect can be obvious at higher frequencies. Standard Hanning apodization can be implemented on the array to reduce the sidelobes at the cost of further reducing the FOV. However, a Roll-off design is proven to keep a flat receive signal across the elevation (column) direction but the aperture will have to be increased [4.18].

A very critical limitation is the field-of-view mentioned in Section 4.6. To improve the field-of-view, the level of defocusing must be increased. Although an acoustic lens could be used, it would be very difficult to perform beamforming through an acoustic lens as delay distances of the lens would need to be carefully measured. Nevertheless, this investigation would make a very interesting study. For this thesis work, a curved RC array is fabricated to address the limitation in FOV. A curved array would increase the defocusing ability of the transmit beam. A simulation is presented next to visualize the defocusing.

4.8 Simulation of Curved Array

The simulated RC array parameters are identical to the actual array presented in Chapter 6. The pitch of the 32 by 32 element RC array is 0.4 mm. The aperture is 12.8 mm by 12.8 mm. The radius of curvature is 10 mm. Although Field-II library has many predefined array configurations, there were no functions to create 2-D curved arrays. As a result, the vertices of each element in the RC-Array was pre-calculated and imported into the corresponding function. The transmit and receive aperture must be defined separately since element assignment to the vertices coordinates are completely different. The Matlab code is provided in Appendix B. The simulated aperture is shown in Figure 4-12. The simulated acoustic beam profile at the focus depth with respect to time is depicted in Figure 4-13. Numerous wire targets were also imaged in the B-mode shown in Figure 4-14. In the B-mode image, it can be clearly seen that the field-of-view is increased dramatically. The blurring of the wire targets further form the aperture can be easily corrected with multiple depth focusing through beamforming or dynamic focusing.

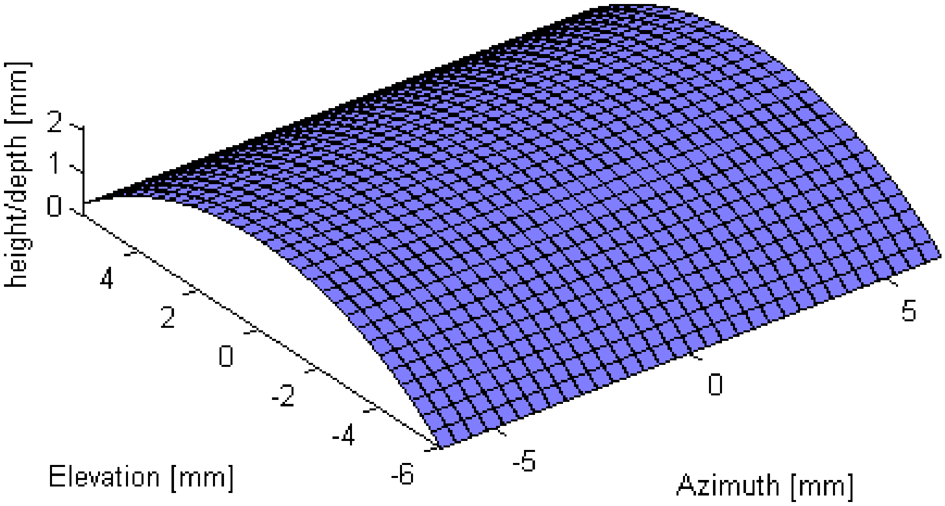

Figure 4-12: Curved RC-array Aperture

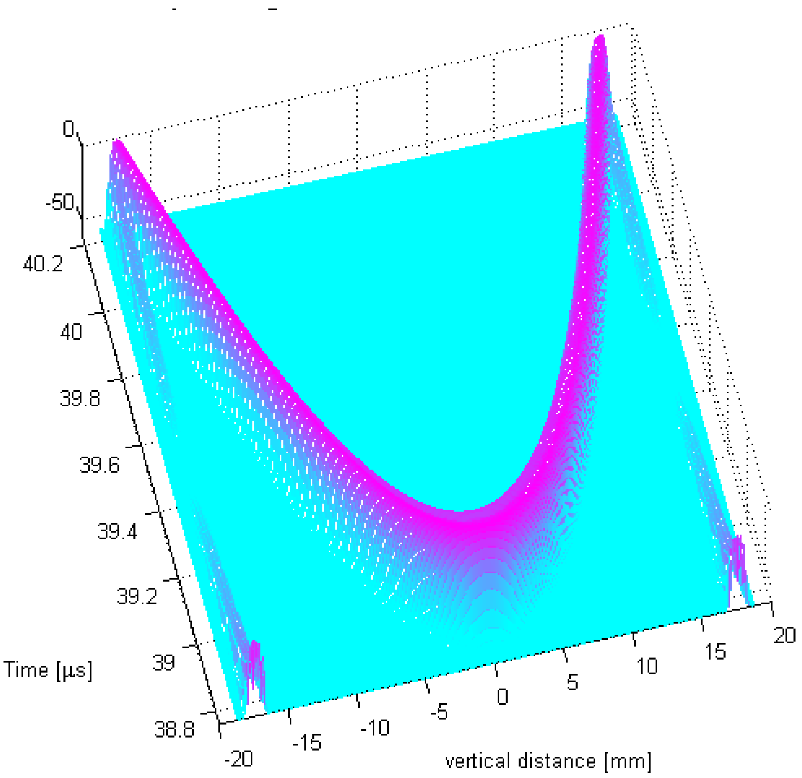

Figure 4-13: One way acoustic profile (in elevation) of curved RC-array

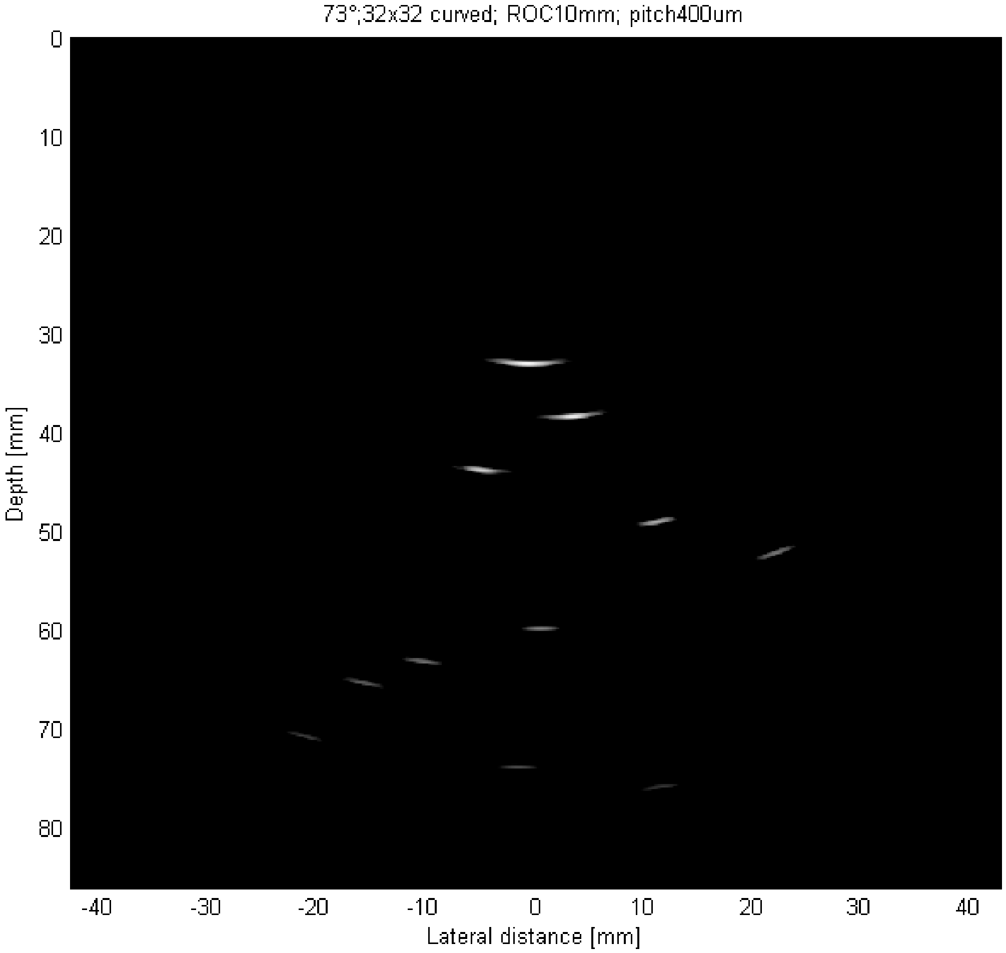

Figure 4-14: B-mode image with the curved array.

Chapter 5 QUASI-REAL-TIME 3D ULTRASOUND IMAGING

5.1 Need for Customizable Ultrasound System

From its initial intended application in non-destructive testing [5.1], the majority of CMUTs technology research efforts have branched towards medical diagnostic and therapeutic use [5.2]. A notable milestone was presented by Stephens et al. in 2013 where the group reported the first in-vivo use of a CMUT-based catheter for imaging and ablation [5.3]. While CMUT designs for intravascular ultrasound (IVUS) and intracardiac echocardiography (ICE) have been popular [5.4]-[5.6], the efforts dedicated to large high-density 2D arrays [5.7]-[5.9] and photoacoustic imaging (PAI) [5.10][5.11] are also gaining momentum. In a synergistic manner, large high-density 2D arrays, which can provide large volume scans, can also work well with PAI to obtain optical contrast and ultrasonic resolutions that are crucial to applications such as breast and prostate cancer diagnosis [5.11][5.12].

In a 1D-array CMUT system, aside from the front-end electronics and the transducer fabrication, the rest of the imaging system can remain identical to conventional systems [5.13]. Meanwhile, despite the fact that the fabrication and packaging of CMUT-based large high-density 2D arrays has matured greatly, it is still difficult to construct a real-time volumetric (RT3D) imaging system due to two primary design challenges [5.14]. First of all, for large high-density 2D array-based RT3D imaging, the number of transmitting (Tx) and receiving (Rx) events can be limited by the speed of sound and the requirements for fast frame-rate (>20 fps). Therefore, using each element for both Tx and Rx, (also known as full-matrix addressing) is not practical. Hence, the first design challenge involves optimizing beamforming through finding a subset of Tx and Rx elements where the image quality approaches to that of a full-matrix array. Sparse array and synthetic aperture techniques [5.15]-[5.21] are amongst the most popular beamforming methods and there exists ongoing research on discovering optimal layouts using random approaches [5.22]-[5.24], genetic algorithm [5.25], and linear programming [5.26]. Generally, however, a reduction in the number of transmit elements will decrease the transmitted energy and signal-to-noise ratio while increasing the side lobes. Furthermore, many of the optimization algorithms under-perform in off-axis beamforming [5.27]-[5.30]. The second design challenge stems from the backend imaging system where the large number of transducers in a large high-density 2D array also demands high Tx and Rx channel count. The resulting RF data would also require a large system throughput to transfer data to a processing unit such as a field-programmable gate array (FPGA), central processing unit (CPU), or graphics processing unit (GPU). Currently, very few systems have reported being able to support 2D arrays. Some of those examples include Choe et al. who recently demonstrated RT3D imaging for a 64-elements ring array [5.31] that displays three cross-sectional images at 45 frames per second and Bhuyan et al. who demonstrated a 32 × 32 elements CMUT RT3D system with 5 volume frames per second. It is important to note that this rate is limited by the data-transfer rate between the data acquisition system and the PC [5.32]. Both systems were developed using a Verasonics™ imaging system.

With the first design challenge in mind, our group fabricated Row-Column Addressing CMUTs (RC-CMUTs) [5.33]. The Row-Column (RC) addressing scheme achieves RT3D while using all elements for transmitting and receiving. More importantly, at high frequency and for large arrays, this scheme excels at reducing the number of electrical leads and computational complexity. Upon investigating a suitable prototyping platform for driving the RC-CMUTs, we considered adopting the Verasonics™ Vantage system. This system offers up to 256 Tx and 256 Rx channels and 14 bit A/D converters (ADCs) with programmable sample rate up to 62.5MHz, which allowed the use of transducers operating from 0.5 to 30MHz [5.34]. A recent upgrade provides a data transfer rate of 6.6 GB/s is also critical in ensuring a real-time frame-rate. This system satisfies our current requirements for driving our 32x32 CMUTs, centered at 5.9MHz as we only need 32 Tx and 32 Rx channels. However, as we intend to fabricate higher frequency RC CMUTs in the future, we may require sampling rate beyond 62.5MSamples/s. For PAI application where transducers can operate beyond 40MHz [5.35], a higher sampling rate would be necessary. Furthermore, as the channel count increases, the system throughput must increase as well. While the newest Verasonics™ system can maintain our current demand of 3.2GB/s of throughput with 32 Rx channels, once the channel count increases beyond 100 receiving channels, the system throughput would likely be a limiting factor in frame-rate. An alternative prototyping platform we considered was the PCI eXtensions for Instrumentation (PXI) as it better addressed some of these aforementioned problems. The PXI’s modular, reconfigurable, and plug-and-play nature are suitable for prototyping an ultrasound machine. PXI systems are also commonly used for building automation systems and laboratory instruments that require communication buses, data acquisition, instrument control, machine vision, and motion control. With respect to data acquisition, a wide range of digitizer modules are available depending on the operating frequency. Given that some digitizers are intended for transducers operating at beyond 200MHz, high frequency ultrasound operation can be fulfilled. With respect to system throughput, chasses offering beyond 12 Gb/s are available and can be synchronized such that multiple chassis can be used. Recently, Ohbayahi *et al*. used a PXI platform to achieve real-time optical coherence tomography [5.36]. 320 transducers were sampled simultaneously at 50 MS/s while FPGAs and a GPU were used to perform signal processing and real-time image reconstruction. Software details of the system can be found in [5.37]. Our group reports a similar architecture customized for RC-CMUT-based RT3D ultrasound imaging.

5.2 System Design

The Row-Column (RC) addressing scheme achieves RT3D while using all elements for transmitting and receiving. More importantly, at high frequency and for large arrays, this scheme excels at reducing the number of electrical leads and computational complexity. The system design will be explained in two parts: the front-end system that contains the interfacing electronics, and the back-end system, which is responsible for beamforming and image reconstruction. For detailed reference of the firmware design, which is developed with LabVIEW FPGA, please refer to the application note written by our group [5.43][5.43]. The RC CMUT array used in this system is fabricated by our lab. Figure 5-1 shows an SEM image of the 5.9MHz 32×32 RC CMUT array fabricated using a wafer-bonding [5.40]. The corresponding point spread function can be found in [5.42]. The aperture size is 4.8mm×4.8mm with a 150μm pitch.

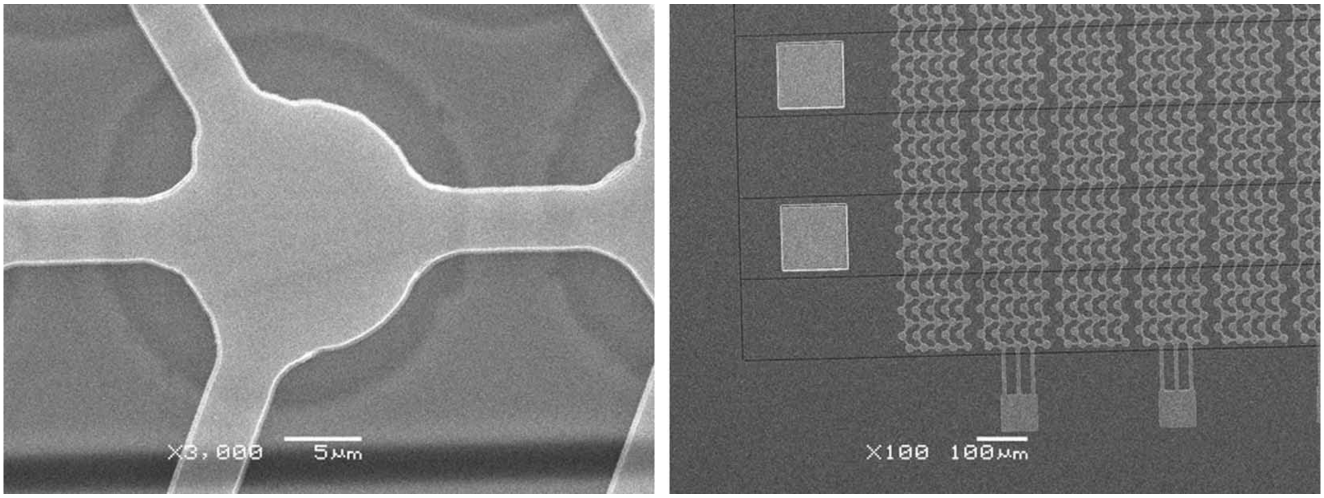

Figure 5-1: SEM images of a 32 × 32 element CMUT array.

5.2.1 Front-end System

A typical ultrasound system includes front-end electronics such as time-gain compensators (TGC), pulsers, and amplifiers. A custom built circuit board shown in Figure 5-2 is designed to house the front-end components without the TGCs. The basic Tx and Rx circuitry for this system is very similar to the 1D CMUT system and can be found [5.44]. In fact, the RC CMUT circuitry is simpler than the 1D circuitry. The switches for toggling between the transimpedance amplifiers and pulsers are not required because the Tx and Rx circuitry are separated.

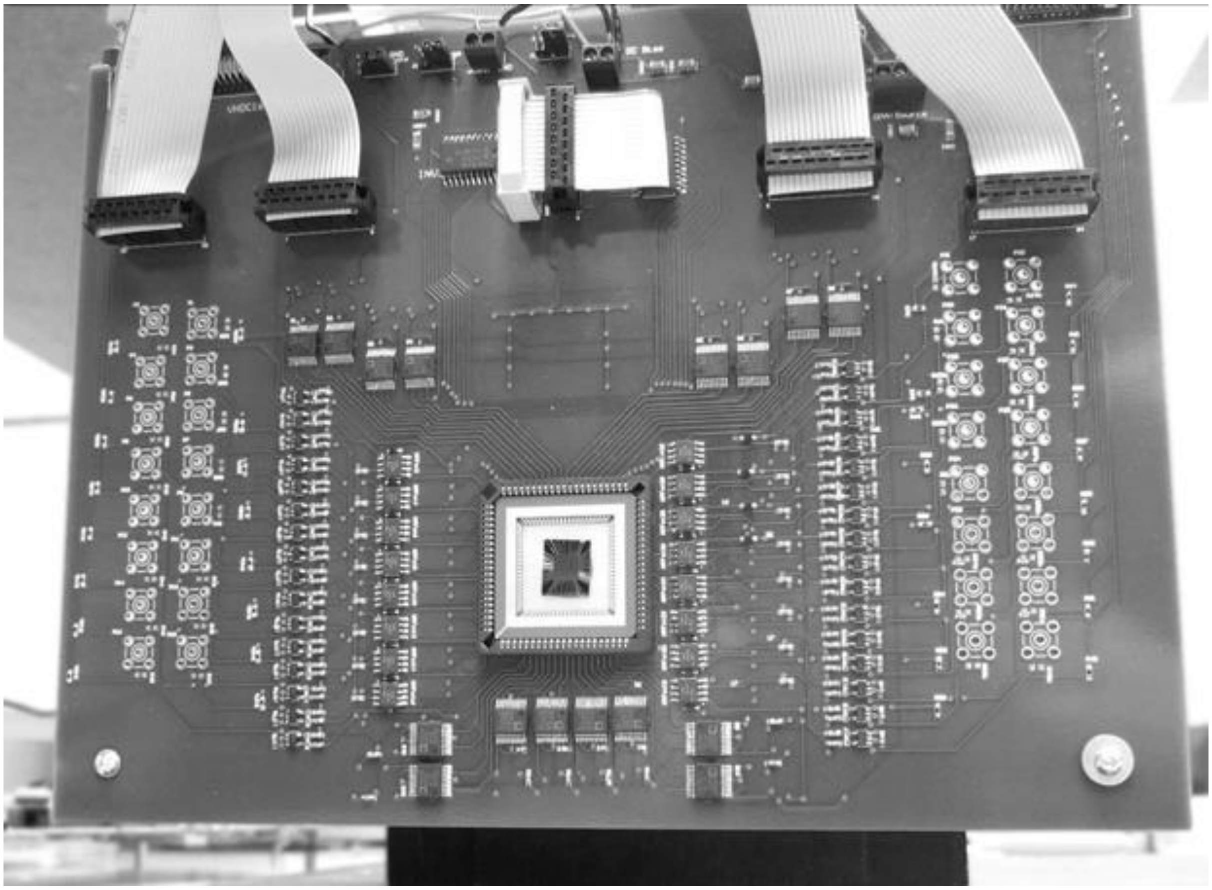

Figure 5-2: Customized PCB for interfacing the CMUT with the front-end circuitry. Analog components (i.e. amplifiers) are connected to the sides/rows of the CMUT. Pulsers are connected to the top and bottom.

5.2.2 PXI-based Back-end System

The PXI-based system includes 4 main components: the analog-to-digital (ADC) adapter module, the FPGA module, the embedded controller module, and the chassis, which serves as the backplane of the system. The embedded controller module includes an Intel Core 2 Quad 2.26GHz CPU and a Windows 7 operating system. The FPGA module and the embedded controllers are card-based modules that can be fitted onto the slots of a PXI chassis (NI PXI-1042) while the ADC adapter module is connected externally to the FPGA card. The ADC module, NI 5752 (National Instruments, Austin Texas), contains 32 channels of 12-bit ADCs, which sample at 50Ms/s. The PXI chassis can synchronize with multiple NI 5752 modules to increase the channel count for future development. Figure 5-3 shows the system diagram of the imager. The section at the left, separated by the dotted lines, shows the components that dock within the PXI system. The middle section shows an external FPGA that was used for sending delay instructions for Tx beamforming. The section at the right shows the front-end system, which was implemented on a custom designed printed circuit board (PCB).

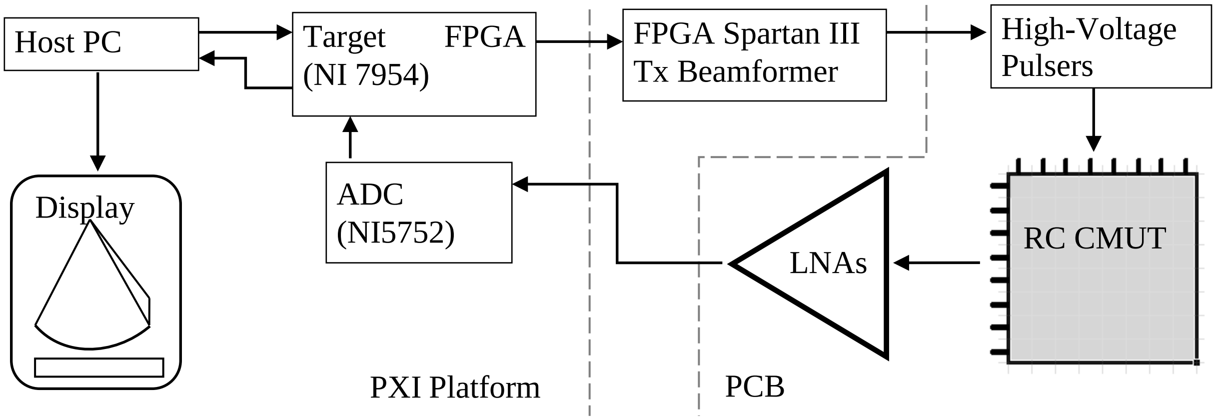

Figure 5-3: Ultrasound system block diagram.

The NI 7954 module contains a Virtex-5 LX110 FPGA and was programmed in hardware description language (HDL) using LabVIEW FPGA development platform. One of the main advantages of using the LabVIEW FPGA is that an understanding of HDL is not needed while all the software implementation can be made in a purely graphical design environment. Users have access to signal processing libraries for customizing functions to aid beamforming programming. Furthermore, MATLAB functions can be called from LabVIEW and used for data post-processing and image reconstruction.

5.2.3 Tx Beamformer

The transmit beamforming operations is done with a 280MHz clock, which results in a 3.57 ns resolution in pulse delays. A limitation with the previous PXI set-up [5.45][5.45] was the lack of a dedicated PXI module which can provide enough digital inputs and outputs (DIOs). After connecting the ADC adapter module, the NI 7954 FPGA module is limited to only 16 digital output channels. As a result, only 16 transmit columns were used for the previous system. This limitation can be overcome by adding an additional PXI module that provides more DIO pins and setting the added module to communicate with the NI 7954 module. As a temporary solution for this study, we used a readily available external Xilinx Spartan-3FPGA development board to provide sufficient Tx channels. DIOs were assigned as follows: 32 pins were used for toggling pulsers, 7 pins for obtaining the azimuth angle specified by NI 7954, and 1 pin for signalling between Tx and Rx mode. A 17-bit counter was declared along with a lookup table containing delays for performing focusing. When the Spartan-3 FPGA receives the input of the azimuth angle and a signal to start Tx event, the counter starts to increment.

5.2.4 Target FPGA

The target FPGA is designed to toggle between Tx/Rx events, read from ADCs, and transfer data to the Host PC. When the Host PC specifies a scanning angle, the target FPGA signals the Spartan-3 FPGA to start sending out pulses by toggling the Tx/Rx switch. Once the transmit event is completed, the target FPGA's first-in-first-out (FIFOs) starts reading from the ADCs. The FIFOs are configured in 64 bits with a 1024-element capacity. 4 ADC channels are stored to each FIFO and a total of 8 FIFOs were used. The FIFO memory size allows 1000 samples to be collected at 50Ms/s. The transfer of data from the target FPGA FIFO to the host FIFO requires Direct Memory Access (DMA) FIFOs. Although all the ADC channels are read simultaneously, the target FPGA FIFOs are appended into the DMA FIFO sequentially which takes a total of 80µs (4 FIFO × 1000 elements) to complete. Once the DMA FIFO writing event completes, the target FPGA goes into an idle mode and waits for the Host PC to signal for additional azimuth angle scanning.

5.2.5 Host PC

The Rx beamformer and image reconstruction firmware is written in LabVIEW. The flowchart of the firmware processes is presented in Figure 5-4. Prior to beamforming and visualization, several initialization steps are made to ensure a proper Host-PC-to-Target-FPGA connection. The firmware first checks if the chassis, embedded module, and Target FPGA modules are compatible. Next, the firmware configures and selects which targets to run. Here, the Target FPGA also notifies the host that an external IO module (i.e. ADC adapter module) is connected. A component-level-intellectual-property (CLIP), which provides information of the adapter module's inputs and outputs, must be detected by the firmware. Once the clocks between the modules are synchronized, the target module sends a CLIP-ready signal, which indicates that the configured modules are synchronized and thus ending the initialization sequences.

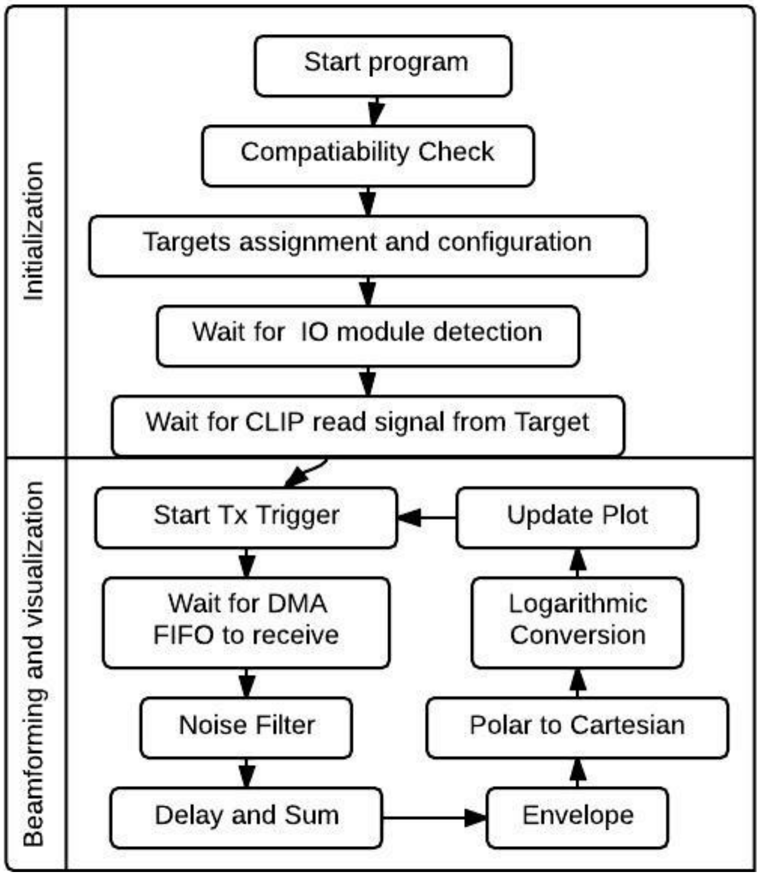

Figure 5-4: Flowchart of firmware within the Host PC.

After the initialization, the Tx trigger and the focusing angle are sent by the Host to the Target FPGA; this marks the start of the Tx beamforming in the Target FPGA. Immediately, the firmware waits for the DMA-FIFO to populate with the data read from the ADCs. Next, the concatenated DMA data are split into 32 arrays with 1000 sampled points each. The receive beamforming is done by limiting the sampled points based on the delay instructions associated with the angles. The reduced data set contains 660 sampled points which corresponds to 10 to 30mm in range, assuming a speed of sound of 1497m/s. The time-of-flight data are fed into delay-and-sum operators follow by envelope detection employing the Hilbert transform. Once all angles in the elevation are subjected to beamforming, linear interpolation and polar-to-Cartesian operations are applied to the data prior to plotting as B-mode images in LabVIEW using the NI IMAQ library at 60dB dynamic range. This interface allows user to specify which planes to view.

5.3 Imaging Results

In order to compare and evaluate the actual result, a 5.9MHz, 32 × 32 elements (4.8mm × 4.8mm) transducer array is modeled using Field II. To simulate the transducer, a 1D linear array is used to transmit and focus in the azimuth direction. Kerf, element width, and element height are set to 0.03mm, 0.12mm, and 4.8mm, respectively, to mimic the actual RC-CMUT layout. Sub-elements are configured to 3 in the *x*-direction (i.e. azimuth) and 20 in the *y*-direction (i.e. elevation) in order to mimic the actual array configuration. The same configuration is used to model receive aperture, except the 1D array is rotated orthogonally. A single cycle sinusoidal pulse with a center frequency of 5.9MHz excites the transducers. Phased-array focusing is done to focus 20mm away from the aperture on the center axis. The one-way radiation pattern was generated by finding the maximum value of the demodulated signal detected by an ideal point receiver scanned at a plane that is parallel to the aperture at a distance of 20mm. The point spread function was generated by scanning an ideal point target located at [x, y, z] = [0, 0, 20] mm. The maximum value of the demodulated received beamformed signal was plotted as a function of the lateral distance in the azimuth and elevation direction 20 mm away from the aperture. The demodulated signals are normalized and presented with an 80 dB dynamic range.

A B-mode image is generated for wire targets parallel to the aperture. The wires run in the azimuth direction. The 90° sector plane in Figure 5-5 is taken in the elevation dimension perpendicular to the aperture. The beam is focused at 20mm (z). The three wires on the right are positioned at coordinates (-0.5mm, 15mm), (0mm, 20mm), and (0.5mm, 25mm) in the y-z plane while the left most wire is positioned close to (-1.5mm, 27.5mm). As expected, the left most wire, positioned near the edge of the transmitted beam’s focal height shows more defocusing than the wires closer to the center.

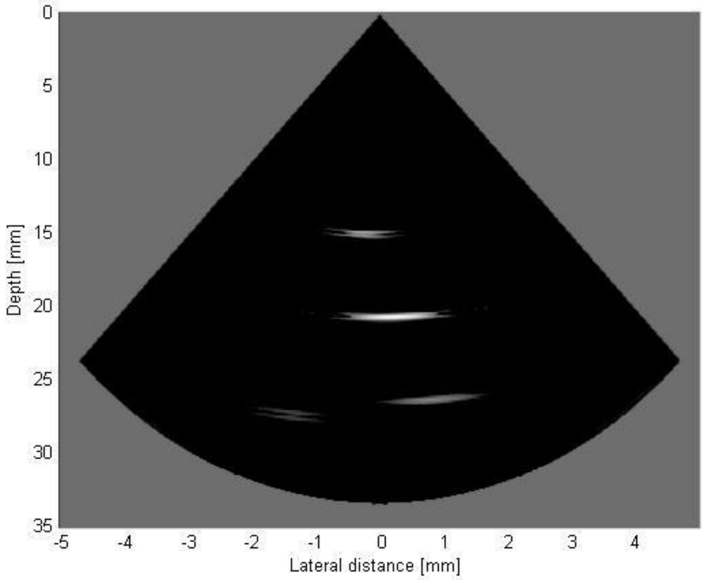

Figure 5-5: Simulated B-Mode of wire targets.

The actual wire targets under the same configuration as simulated are imaged and shown in Figure 5-6. Acquired RF data were averaged over 32 times to remove noise and enhance image.

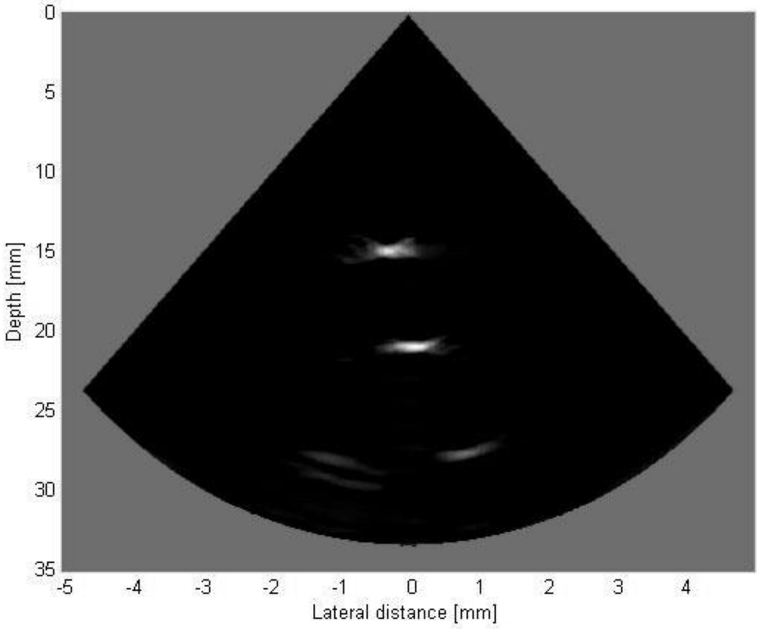

Figure 5-6: Measured and reconstructed B-mode image of actual wire targets. Unfocused wire is seen on the bottom left.

The set-up of the pinheads is shown in Figure 5-7. Three 1/16 inch (1.59mm) pinheads are laid out ~2mm apart in both x- and y-direction and 4mm apart in depth. The bottom pin is tilted to better direct sound to the aperture. Figure 5-8 illustrates nine sequential B-modes planes acquired over the volume that confines the pinheads. Each B-mode shows the reconstructed data from a single Tx event acquired with the PXI imager. Here, 0° is defined as the orthogonal plane that intersects the aperture at the center. Since the reflected signals are weaker when further away from the focal spot (20mm), software equivalent of time-gain-compensation (TGC) is applied. The pinheads are connected to a sponge that absorbed sound to reduce reflection. The sponge is supported by a stage while being submerged in a vegetable oil-filled tank.

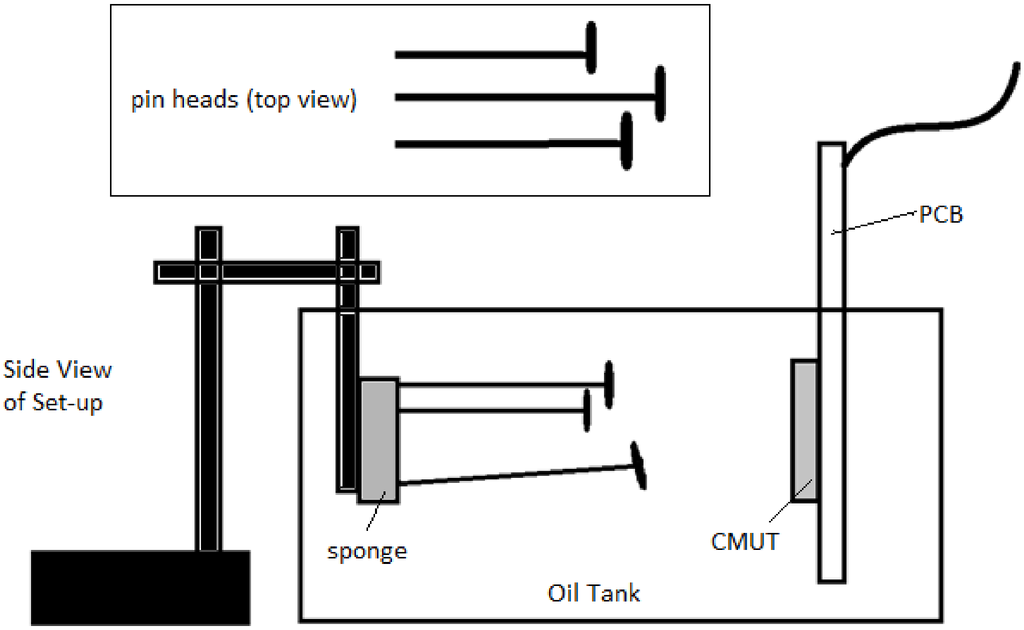

Figure 5-7: Side view of the oil-tank set-up. The top view of the 3 pins is also shown.

The total time for each Tx/Rx event, including the time it takes for data to transfer from the FPGA to Host PC, is 5ms. It takes 205ms to complete a single ± 20° volume scan with no averaging. An additional 20ms is required for the image reconstruction. Figure 5-9 is a 3D rendered image created from the data set shown in Figure 5-8. The rendered image is processed by the 3D Ultrasound Visualization (UltraVis) platform developed by Vision and Image Processing group at the University of Waterloo.

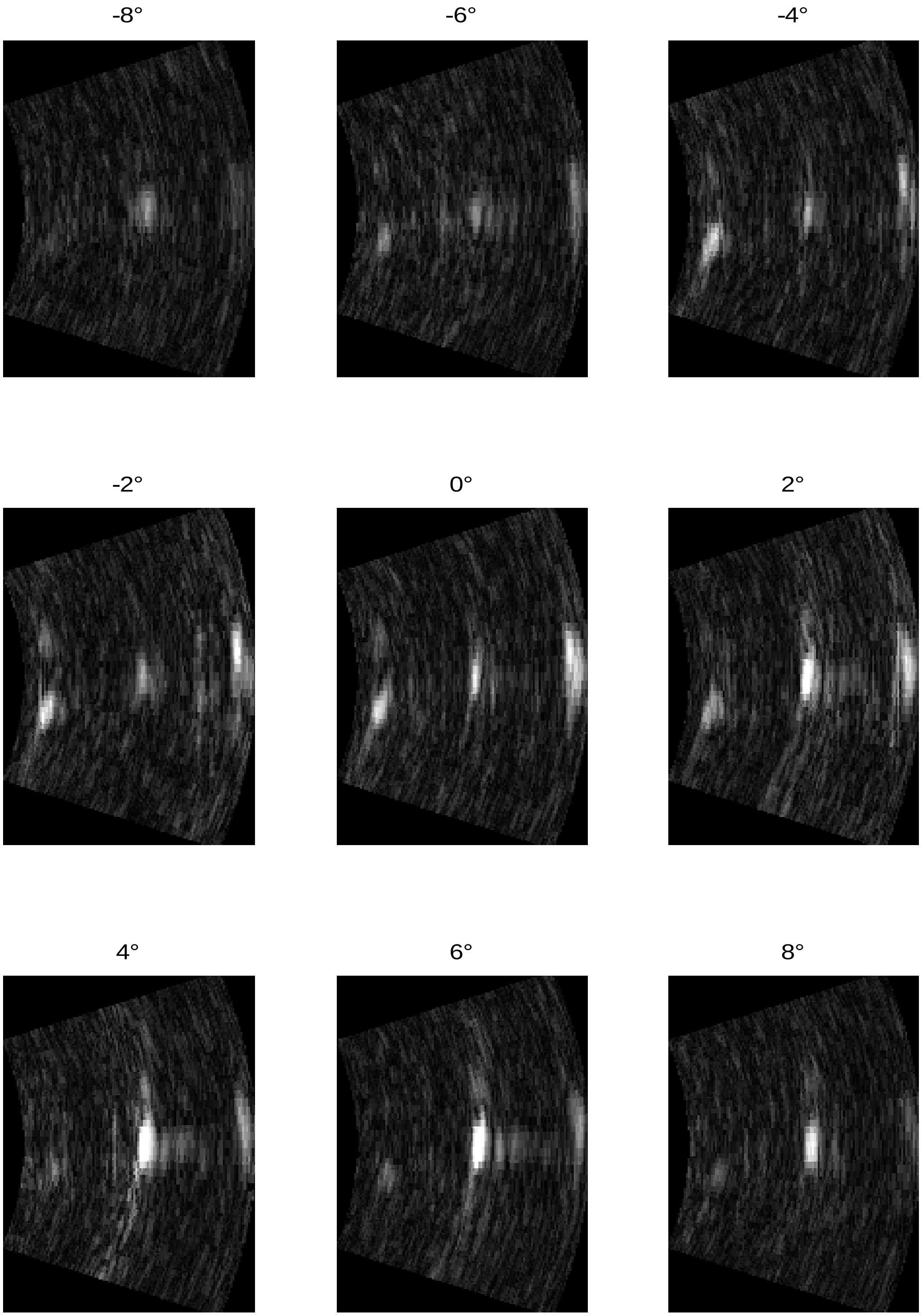

Figure 5-8: Reconstructed image of the pin heads at 8 different azimuth angles.

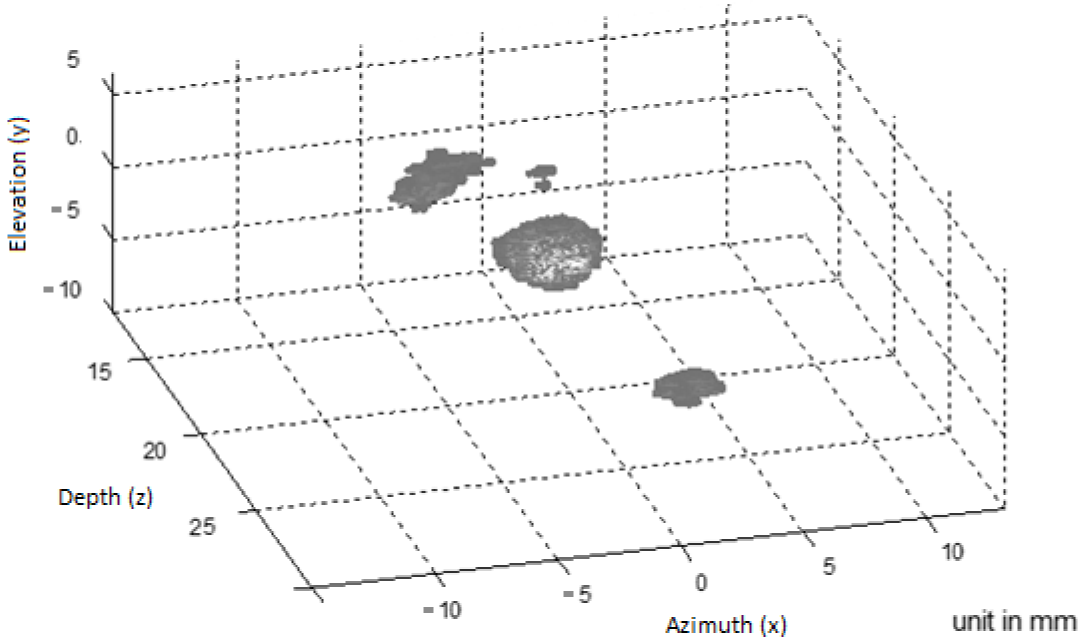

Figure 5-9: 3D Rendered image of the volume created by the 3D Ultrasound Visualization (UltraVis) platform developed by Vision and Image Processing group at UW.

Discussion

5.3.1 Focusing Volume

With the RC method, the cost of achieving a fast scanning rate and minimal connection count is that focusing is lost in one direction during both transmit and receive event. For example, when a wavefront is generated during transmit, phased-array focusing is only applied to the azimuth direction while natural focusing occurs in the elevation direction. As a result, the transmitted pulse weakens immediately outside the natural focal zone, preventing sound from focusing directed above or below the focal height. This phenomenon was verified from the simulation results where the the -12dB beam height at 20mm away is ~5mm, which is approximately the height of the aperture. Thus, it can be concluded that a flat RC array design greatly limits the field of view. Increasing the aperture size would be the most straight forward approach to increase the scan volume and the resolution. As calculated, by increasing the array size from 32x32 to 64x64 elements, the lateral resolution improves from 1.3mm to 0.7mm. Although the aperture size cannot be compromised for IVUS/ICE applications, there is more room for play in applications such as breast or prostate cancer screening. Therefore, using a curved array would be a promising solution to address the limitation.

5.4 Chapter Conclusion and Future Work

A quasi-real-time imaging system is designed and constructed to aid the imaging and characterization experiments involving RC-CMUTs. A customized PCB is designed to drive the RC CMUT array. A PXI platform is chosen for building the beamformer because it can accommodate large numbers of high-sample-rate ADC channels and also Tx channels. In addition, the PXI-based imaging system can be built without extensive digital logic knowledge while providing necessary tools in measurement and acquisition that can be interfaced by LabVIEW. As a result, ultrasound engineers will have more freedom to build their own modularized system. This is the first quasi-real-time volumetric system demonstrated for the RC CMUTs. It is also the first reported medical ultrasound imaging system where a PXI platform is used.

Although the presented platform is designed to be able to conveniently upgrade to a larger RC array size (e.g. 128 × 128 elements), it is not designed to achieve real-time (>20fps) frame-rate. The reported chassis, NI PXI-1042 has a limited backplane throughput of 132MB/s. For an acquisition rate of 50MSample/s/ch, 32 simultaneous channels, and 2 bytes of memory per sample (12 bits of precision may use 16 bits of transfer), the ideal streaming rate from the FPGA to the Host PC would require a throughput of 3.2GB/s. At the ideal streaming rate, data can be transferred to the PC's memory before it is overwritten; therefore, the frame rate will not be limited by the throughput. In order to avoid data being overwritten before transferring to the PC, the presented system does not allow additional Tx/Rx event to occur before the DMA FIFO is finished reading by the PC. As a result, the current pulse repetition rate (i.e. 5ms) is much longer than the time-of-flight (i.e. <50µs for 20mm focus). Fortunately, commercial PXI chassis can currently provide a throughput of up to 12GB/s (i.e. NI PXIe-1085, National Instruments). At 12GB/s, 120 channels can be collected at the ideal streaming rate. Beyond 120 channels, multiple chassis would have to be used for simultaneous acquisition. However, even at the ideal operation streaming rate, delay-and-sum and other post-processing operations can limit the frame-rate, as can the 3D rendering. Therefore, it is highly advisable to incorporate a GPU with many parallel cores for these purposes [5.48].

Chapter 6 FABRICATION OF A CURVED ROW-COLUMN ADDRESSED CMUT

This chapter reports a flexible Capacitive Micromachined Ultrasonic Transducer (CMUT) device that is conformable to convex surfaces. The goal is to produce a device that can be mounted on the fingertip so an operator can benefit from concurrent imaging and palpation. Finger mounted probes can be used to track instruments and guide biopsy during complex medical procedures. Clinical trials have confirmed that finger mounted probes can enhance positional accuracy, feedback, and repeatability [6.1][6.2]. The 2-D CMUT array used in this project adopts an electrode addressing format called row-column (RC) addressing scheme, which has been demonstrated to achieve 3D imaging [6.3]~[6.13]. Although the RC-CMUT approach dramatically reduces the electrical leads and computational complexity, it has been identified that the field-of-view, or scan angle, is very limited as a result of the simplification [6.6][6.7]. The original RC design studied by Morton and Lockwood [6.8] was based on a hemispherical RC array, which emphasized the reliance of a defocused beam during RC transmit beamforming. The field-of-view, which is determined by the extent of the defocusing, is ultimately determined by the curvature of the array. The optimization of pitch, element count, and radius-of-curvature in order to achieve acceptable resolution was determined empirically through simulations [6.3]. The simulated RC array produced a volumetric image with a field-of-view of 60°×60°, while the spatial resolution was comparable to that of a high-quality 1-D array. In reality, however, it is difficult to fabricate curved 2-D arrays and to the best of the authors' knowledge, a curved RC-CMUT array has yet been demonstrated. As such, the focus of this paper is to determine the feasibility of producing a convex RC-CMUT array.

CMUT technology, first introduced by M. Haller and B. T. Khuri-Yakub in 1994 [6.14], has gone from a simple proof-of-concept to a highly invested technology in the next generation of intravascular ultrasonic imaging and intracardiac echocardiography [6.15]. The nanoscale feature size, as provided by MEMS technology, has offered the new transducers an impressive bandwidth compared to conventional piezo-based transducers. Moreover, the microfabrication process offers a new platform for creating various physical and electrical designs that otherwise would be difficult to achieve with conventional transducer machining techniques. As discussed in Section 3.4, the current approaches for fabricating CMUTs are generally divided based on how the plate layer is made. The surface micromachining approach involves depositing thin films and patterning from the bottom up, including the plate layer [6.16]. The wafer bonding approach fusion bonds two separate wafers: one which holds the plate layer and one which has patterned cavities and bottom electrodes. After fusion bonding, the handling layer holding the plate layer is etched away thus exposing the plate layer [6.17][6.18].

While there were a few attempts to fabricate flexible CMUT arrays, these processes generally share similarities to the way flexible optoelectronic displays are built. Modern flexible electronics, including flexible MEMS devices, are typically built with a combination of inorganic and organic electronic materials, whereby thin-layer silicon and metallic-based integrated circuits are deposited on top or embedded within flexible substrate layers. An example is the hemispherical electronic eye camera developed by Ko *et al* [6.19]. The fabrication of this camera was done by first stretching a hemispherical polymer element radially to form a flat substrate. Next, a thin silicon layer, which held the sensor array, was transferred onto the stretched polydimethylsiloxane (PDMS). Once released, the whole device deformed into its original hemispherical shape. Meanwhile, Wong and Ladabaum [6.20] reported the first flexible CMUT array fabricated using a series of precision etching, polishing, and lapping (Method #1). The substrate was eventually thinned to approximately 150 µm and the radius of curvature was made to 40 mm. Zhuang *et al.* [6.21] reported a flexible CMUT array by first etching through-trenches to isolate individual CMUT elements followed by filling the trenches with polydimethylsiloxane (PDMS) to provide bendability between elements (Method #2). Cartoni *et al.* [6.22] presented a flexible array based on a reverse process where cavities, insulating layer, and bottom electrodes were sequentially created using the plate layer as the starting layer. The handling layers were wet etched followed by encapsulation with a flexible material (Method #3). Finally, a flexible micromachined transducer based on a piezo-on-polyimide structure was presented by Wang *et al*. [6.23] (Method #4). Diced PZT ceramics were placed in etched cavities on a polyimide film. The device layer was then covered with PDMS followed by peeling the thin layer off from a silicon substrate.

This chapter reports a novel fabrication process for making a flexible CMUT array. It is also the first reported row-column addressed array that is flexible, hence can be fitted onto a convex probe tip. A convex RC-CMUT can increase the field-of-view which is a critical limitation associated with previously reported RC arrays [6.6][6.7]. Method #1~4 all result in flexible devices but they are not ideal, and in some cases not feasible, for making an RC-CMUT array capable of wrapping around a finger or small probe. Method #1 yields a device thickness of approximately 150μm which cannot offer a small radius-of-curvature. Further thinning to <100 μm using mechanical polishing is extremely difficult without damaging the device [6.24]. Method #2 uses DRIE to etch through trenches to isolate each element before applying PMDS. This is not feasible since the RC-CMUT architecture requires the bottom of the array to be electrically connected in rows and the top be connected in columns as shown in Fig. 1. For Method #3, the reported insulation layer is made of PECVD oxide, which is likely to experience noticeable leakage and dielectric problems. We have chosen to stay with the wafer bonding process as it yields the best performance compared to other micromachining methods [6.18] and the reported insulation materials, such as thermally grown oxide and LPCVD nitride, have significantly higher breakdown voltage. As for Method #4, it is not compatible with wafer bonding nor can it offer vacuum-sealed cavities which are necessary for our CMUTs designs. The reported process incorporates a double SOI wafer bonding process in which the buried oxide (BOX) layer is used as the etch-stop during the bottom substrate thinning process. Since PDMS is resistant to the chemicals for wet-etching, we used it to protect the device side during bottom substrate thinning. The PDMS is then kept as an encapsulation material given its electrical insulation property and also its acoustic matching properties [6.25][6.26]. In the next section, we will present our fabrication process, which can be divided into two parts: the fabrication of a functional 2-D CMUT array followed by the substrate removal process based on wet-etching and PDMS encapsulation.

6.1 Curvature-Stress Consideration

An analytical model was used to study the possibility of fracture due to the bending stress. The stress induced in the CMUT and PDMS encapsulation layer can be modeled with the Moment-Curvature Relation based on Euler–Bernoulli beam theory [6.27]:

$$\sigma = \frac{Ey}{\rho} \tag{6.1}$$

This relation applies to beams with symmetric cross section and that bending takes place only about one of the principal axes of the cross section. Given that the Young's modulus, *E*, of Silicon and PDMS is 170 GPa and 870 kPa [6.26], respectively, the contribution of elasticity is dominated by Silicon. y denotes the distance away from the neutral axis, which is calculated to be 2.56 µm from the bottom of the 5 µm silicon layer. Given a 10-mm radius of curvature, ρ, the maximum compressive stress experienced by the bottom of the silicon is calculated to be 43.6 MPa, which is far from the fracture strength of silicon at 7000 MPa. A more realistic cause to fracturing is from localized stress or cracks that propagate laterally from a flaw at the edge [6.29].

6.2 Fabrication

An RC-CMUT array structure, as shown in Figure 6-1, consists of a pair of orthogonal arrays that define the top and bottom electrodes.

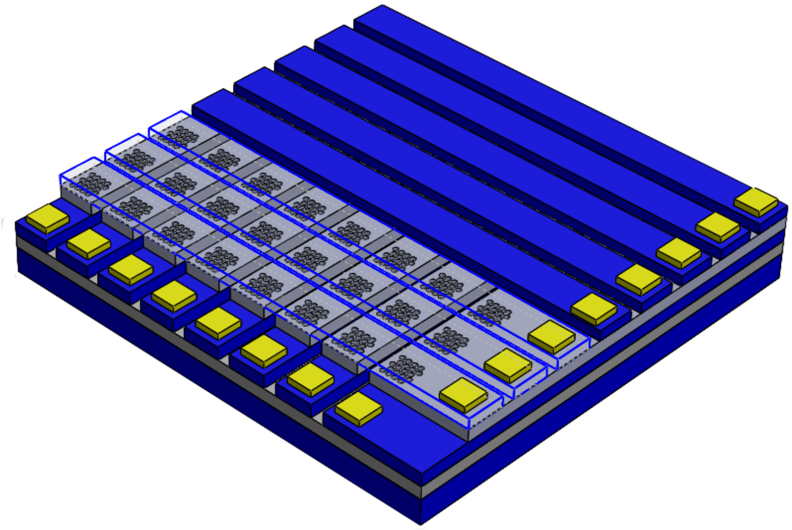

Figure 6-1: RC-CMUT

The fabrication process of the flexible RC-CMUT array is presented in Figure 6-2 and can be separated into two stages. First, an RC-CMUT was made using a double SOI wafer bonding process, which is shown in Step 1~4. Once a single and functional device was made, we proceeded to the thinning processes as shown in Step 5 and 6.

6.3 RC-CMUT

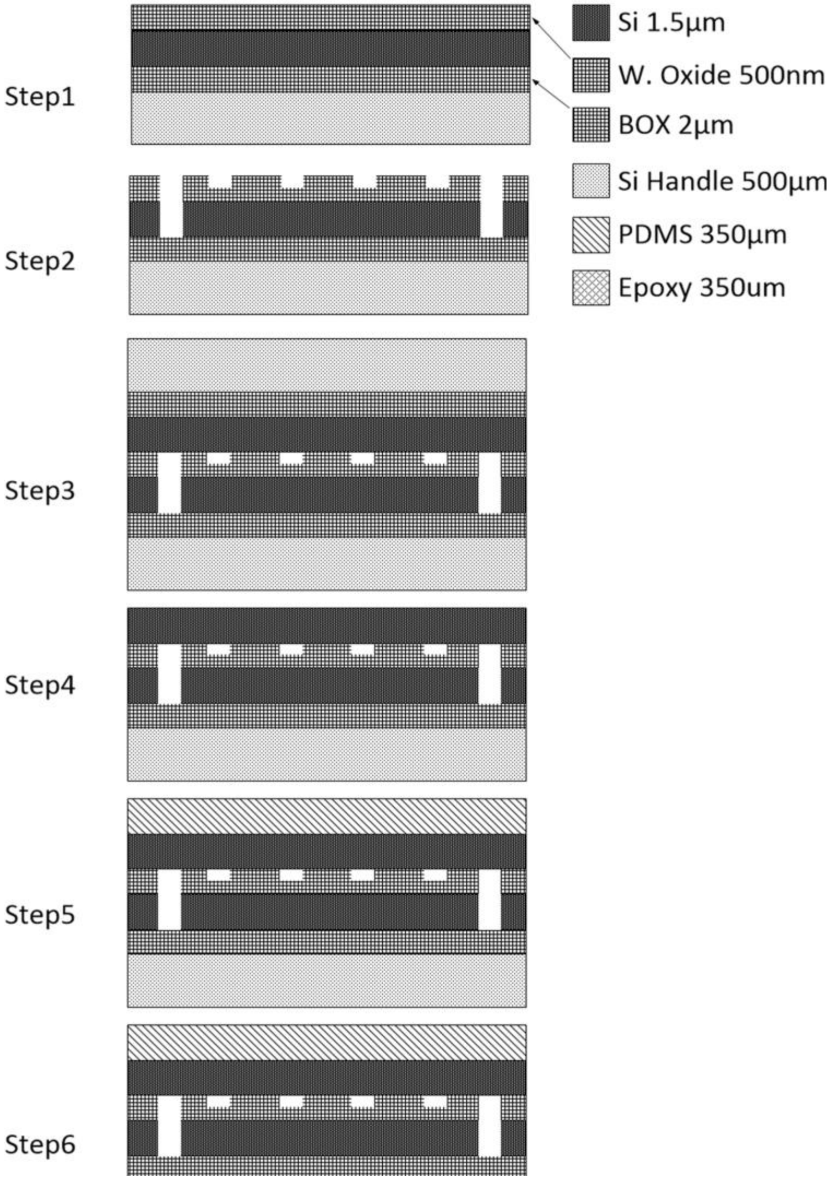

Figure 6-2: Fabrication steps for RC-CMUT and subsequent thinning methods

The first stage of the fabrication process where the bottom and top wafers were bonded is largely similar to the processes reported by Christiansen *et al.* [6.12] and Zhang *et al.* [6.30] with minor differences. 500 nm of silicon dioxide was thermally grown on a 4-inch P-doped 0.001 ohm-cm <100> SOI wafer, purchased from Ultrasil (Step 1). Next, photo-lithography and buffered oxide etch (BOE) were used to pattern and etch the row trenches on the oxide layer. With the same pattern, DRIE was used to etch out the underlying silicon device layer in order to isolate the bottom rows. Next, photo-lithography and RIE were used to etch out the 250-nm deep cavities (Step 2). A standard RCA 1 recipe was used to ensure clean wafer surfaces before direct bonding. Wafer bonding (AWB-04 Aligner Wafer Bonder, AML) was performed between the patterned wafer and a cleaned unpatterned SOI wafer at 3.5-kN downward force followed by 1100-°C annealing in conjunction with thermal oxide growth. As a result, 500 nm of wet oxide was grown on both sides of the wafer. While the bottom handling layer was protected by photoresist, the top handling layer was dipped in 10:1 BOE to remove the oxide on the top handling layer. The handling layer was then removed through wet-etching with tetramethylammonium hydroxide (TMAH) solution (Step 4). There are two subsequent steps not shown in the Fig. 2 to avoid confusion in cross-sectional diagrams and they are as follow: once the handling layer and buried oxide (BOX) layer were removed, the top plate layer was patterned and etched with DRIE to create trenches for column electrode isolation. A combination of wet/dry etching similar to Step 1 was used again to expose the bottom row electrodes. An E-beam metal deposition, followed by a lift-off process was used to create the Al/Cr based metal contact pads. Once the electrodes were formed, the finished wafer was diced into twelve RC CMUT arrays. The final dimension of each array is shown in Table 6.1. On a side note, it is extremely difficult to purchase 4-inch SOI wafers with device layer thinner than 1.5 µm. Manufacturers with Smart Cut™ or Ion Implantation processes that are capable of making sub-micrometer device layers have abandoned the 4-inch diameter wafers. As a result, we had to purchase 4-inch wafers with device layers greater than 2 µm. We then added a wet-thermal oxide layer at the end of step 4 followed by a BOE removal step to thin the plate layer. This method can still yield a smooth and uniform plate. Once the RC device with electrodes was built, a simple characterization step is done with a vibrometer to make sure all elements can vibrate. Micrographs of the device are shown in Figure 6-3.

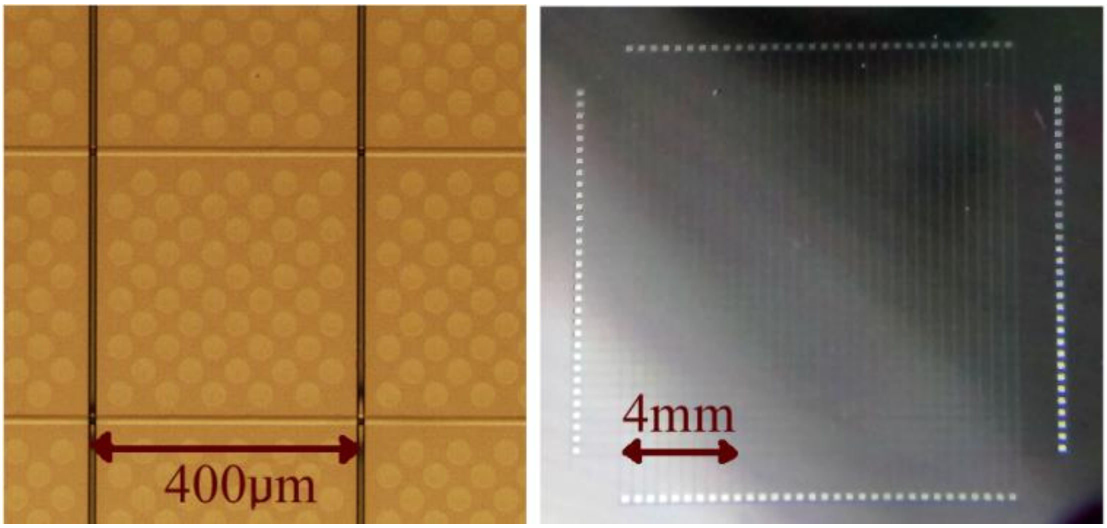

Figure 6-3: Photo of the RC-CMUT array. (Left) Micrograph of with a 400 µm× 400µm sub-element consisting of 50 CMUT cells. The top/plate layer is electrically connected with other elements in columns. Bottom electrode is connected in rows. (Right) Top-view

TABLE 6-1: 32×32 RC-CMUT DIMENSION SUMMARY.

Parameter	*Value*	*Unit*
Array		
Number of elements	32+32	
Element pitch	400	µm
Element width	395	µm
Element length	12.8	mm
Aperture size	12.8×12.8	mm
CMUT cell		
Distance between cells	8.5	µm
Cell diameter	40	µm
Plate thickness	1500	nm
Vacuum gap height	250	nm
Insulating layer thickness	250	nm
Electrode thickness	120	nm

6.4 Thinning

Our group has tried several thinning approaches before we reached our final method. The first approach involved using a wafer grinder/polisher (Ecomet 3 Variable Speed Grinder-Polisher) and chemical mechanical polisher (CMP) (LOGITECH 1CM51-CDP). Although in theory, this should be the fastest way, we did not yield successful results. After a rigorous process development with the polisher and CMP, we could not produce a thickness below 150 µm as wafers can fracture easily. Often times, scratches on the surface from particles on the polishing pad can easily penetrate over 20-µm deep which can become a source of crack propagation. Even after a recipe was developed, wafer handling proved to be too delicate for our capabilities. For example, using wax to mount the four inch wafer onto the chuck of the polisher means that dismounting the wafer through heating the wax can create non-uniform temperature distribution on the thinned wafer leading to fracturing. Some of these problems were also reported by Wong and Ladabaum [6.20]. We have also tried CMP, which is suitable for thinning or planarizing on a submicron level. But it was too slow for bulk wafer thinning. The next method that we tried was using DRIE for fast removal. To thin out a 500-µm handling layer requires approximately 2 hours. The issue associated with this method is that the device layer must be facing downwards which may damage the CMUTs. We did not want to risk this as the plates are extremely thin and fragile. Our final approach was to use a pure wet-etch approach.

TMAH (25% concentration) solution at 80 °C was used to etch the handling layer. Initially, PDMS (Sylgard® 184, Dow Corning) was drop-casted on the top plate layer as the etching mask (Step 5&6). Note that another good option as a protection mask is Brewer Science® ProTEK coating, which can be easily dissolved whereas PDMS can only be peeled off. Nonetheless, we have chosen PDMS since we do not intend to remove it and are using it as an encapsulation layer. The initial drop-casting method led to several processing issues. First, the detachment of the PDMS occurred after only a few hours of wet etching because the TMAH solution would creep under the PDMS layer from the edges. As a result, the TMAH solution would etch the top silicon plate layer which leads to more edge peeling as shown in Figure 6-4. We resolved this issue by ensuring that only the handling layer was exposed to TMAH while the rest of the structure was protected by PDMS. This was achieved by first casting the PDMS onto a 25 µm × 25 mm × 75 mm polyimide (1 Mil Kapton® Tape, DuPont™), which adhered to a standard 75 mm × 25 mm microscope glass slide. Next, the CMUT device was placed carefully, with the handling layer exposed to air, onto a pre-degassed PDMS as shown in Fig. 5. After oven-curing at 80°C for an hour, the cured PDMS thickness was measured to be 350 µm. The slide with the PDMS and CMUT was then secured onto a Teflon wafer holder and submerged into the TMAH solution.

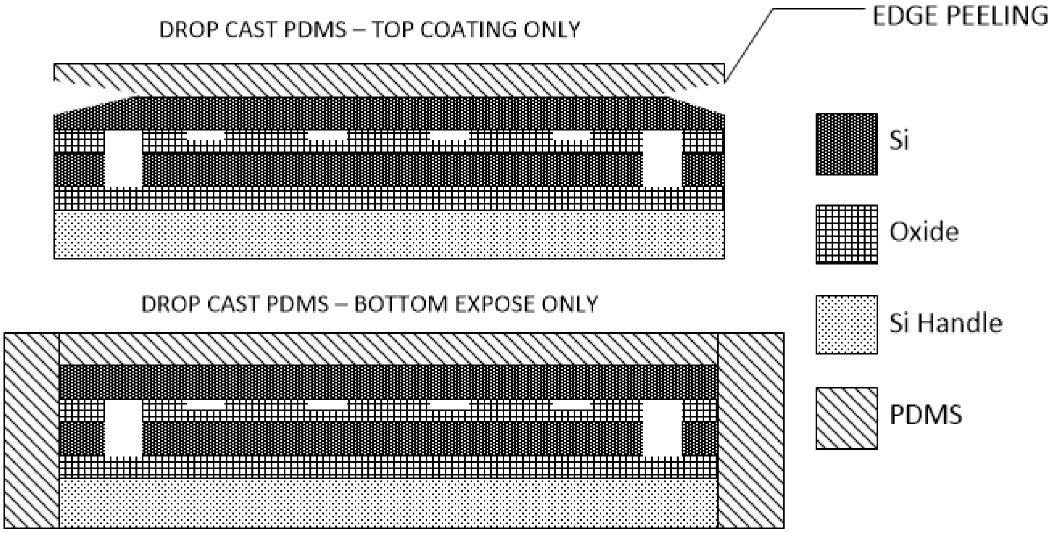

Figure 6-4: Improved PDMS encapsulation method to prevent edge peeling.

The polyimide tape was added for two reasons. First, during etching, it was easy for the PDMS to be lifted off from the glass slide after a long exposure to warm etching solution. In such instance, it was important that the polyimide provided stiffness and kept the device flat. Second, the polyimide tape acted as a good handling layer and can be easily removed by soaking it in IPA and careful peeling. Once the handling layer was etched, a thin layer of epoxy (LePage® Speed Set™) was deposited and evenly pressed to form the backing layer. For characterization purposes, 8 row and 8 column electrodes were shorted and wire-bonded to an external flat cable as shown in Figure 6-6.

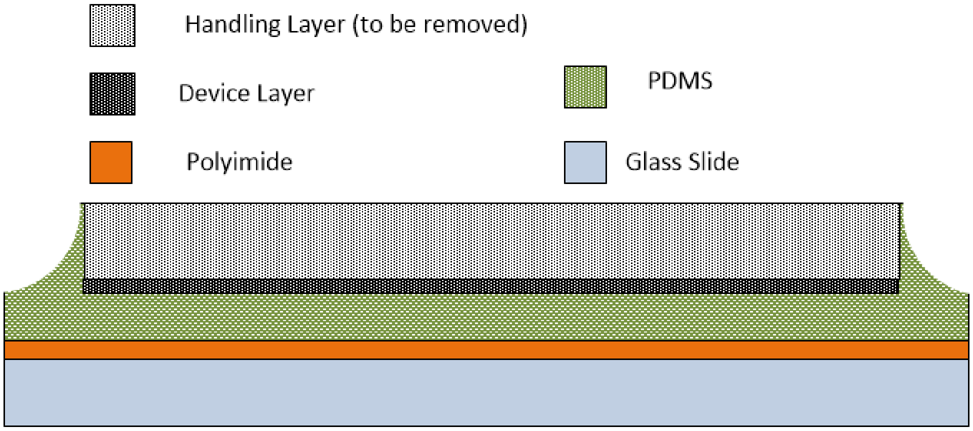

Figure 6-5: Set-up for thinning. CMUT device is carefully placed, exposing the substrate to be etched, onto an uncured 1mm PDMS film. A polyimide (Kapton®) tape is adhered to glass slide before pouring PDMS over it. During etching, adhesive will dissolve; once etching finishes, polyimide can be peeled off leaving a smooth PDMS surface. PDMS thickness in front of device layer is approximately 350 µm.

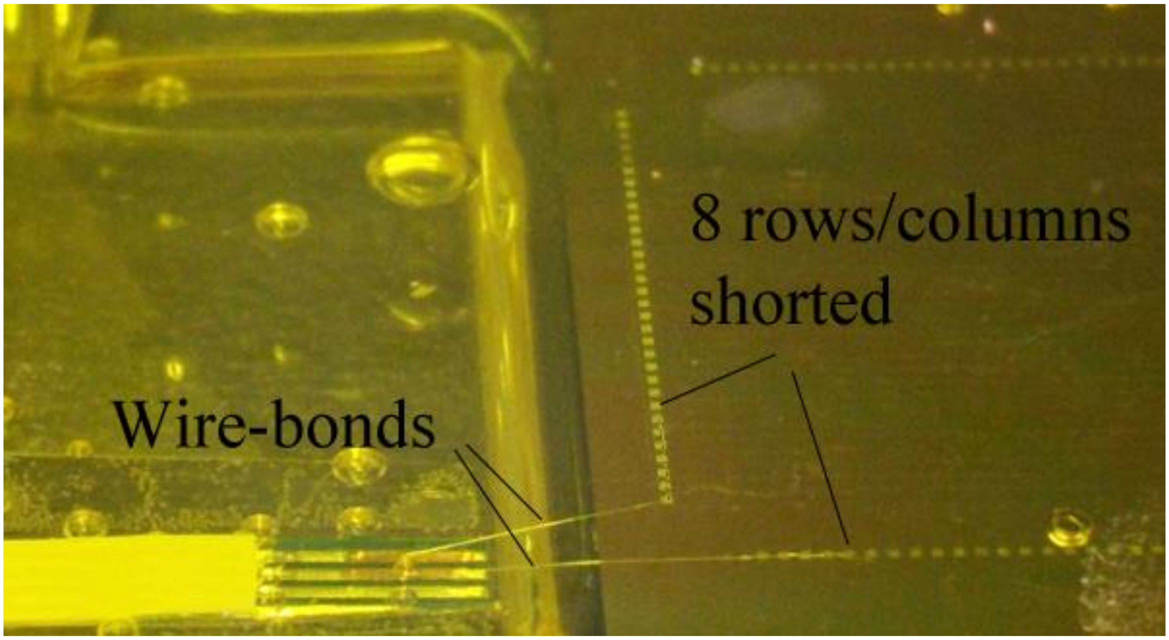

Figure 6-6: Wire-bonds are made between CMUT contact pads and a flat cable prior to PDMS encapsulation. 8 rows and 8 columns were shorted together with a bonder for characterization purposes.

6.5 Results and Discussion

During the fabrication process, a critical design failure was identified: the tearing of the plate. As mentioned in the previous section, the first step of the RC-CMUT fabrication process requires electrical-isolation trenches being etched through the oxide insulating layer and the underlying conductive silicon layer. If the trench width is too wide, a suspending layer, much like the plate, may break during the top handling layer releasing step as shown in Figure 6-7. Fortunately, these plates do not cover the CMUT cells so they do not interfere with the device performance. However, during the wafer thinning step, the same phenomenon could happen to the backside with catastrophic consequences. Figure 6-8 shows that if there is a leak in the bottom layer during etching, the TMAH solution can creep in and dissolve both the silicon layers. Once the etchant dissolves the bottom electrodes, the whole device will become useless. A simple solution would be to decrease the trench width to 10 μm to avoid plate collapse. Alternatively, an additional mask could be used for etching away the plates on top of the trenches so that PDMS can fill in and support the underlying structure.

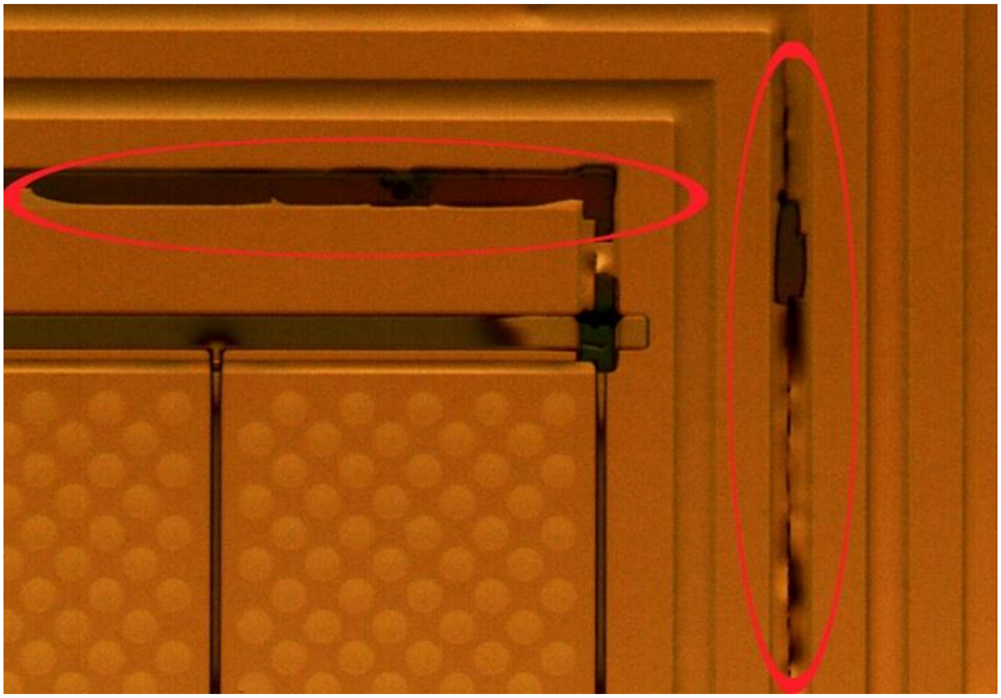

Figure 6-7: Membrane damages occurring at wide trenches using the Vertical-only design.

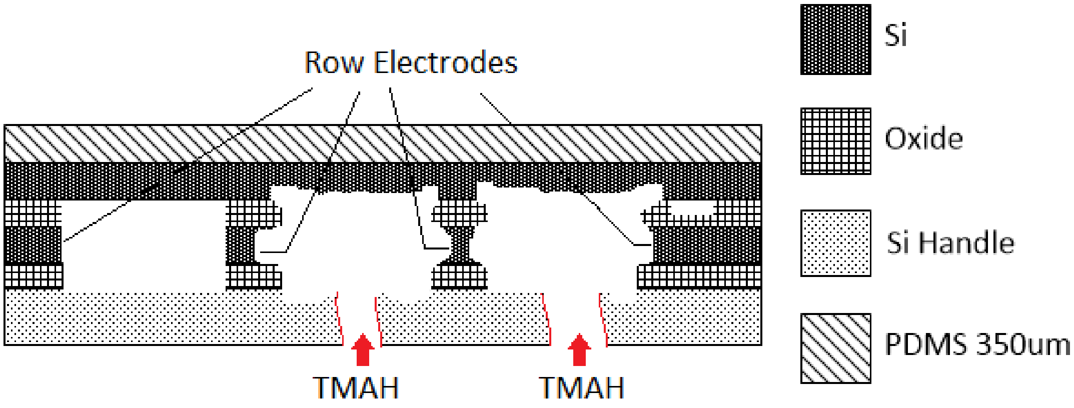

Figure 6-8: Thin plate failure would allow TMAH solution to creep in and etch the silicon row electrodes and cause critical failures.

The final device is shown in Figure 6-9. A small radius of curvature under 10mm can be achieved. Cracks are likely to occur if handled improperly. The flexible device was carefully placed on a curved die with a 10 mm radius of curvature arbitrary picked to demonstrate the possibility of wrapping around a finger. The device yield for designs with 40-µm trench width is zero while the yield for designs with 10-µm trench width is 100%. Some small voids were present from the wafer bonding process but had small impact on the overall yield.

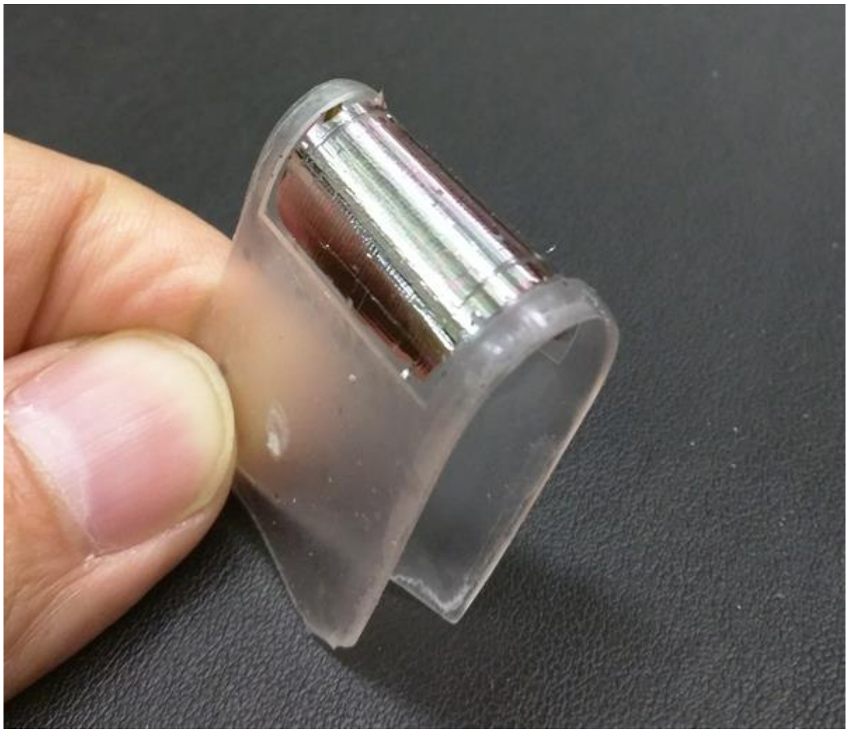

Figure 6-9: CMUT after thinning can be curved.

Prior to thinning, a vibrometer characterization was performed (Polytec OFV-5000, DD-300 displacement decoder). Given a frequency sweep, an in-air resonant frequency of 12.5MHz, where maximum displacement occurs, was measured. Given a 60-V bias and a 15 Vpp AC voltage, the maximum membrane displacement at resonant frequency was measured to be 32 nm. The pull-in voltage was measured to be 72 V. Next, a pitch-catch experiment was conducted in vegetable oil and acoustic signals were captured by a hydrophone (Onda HGL-0200) with signal amplified by a pre-amplifier (Onda AH-2010) before going into the oscilloscope. An 8+8 subset, with a 3.2 mm x 3.2 mm aperture, of the 32+32 array was used to transmit a sound pulse. The elements, biased at 60 V, were pulsed simultaneously with a 15-Vpp single-period 2.5-MHz sinusoidal signal using a function generator (AFG3022B, Tektronix). The hydrophone was placed 15 mm from the transducer, and the time domain signal was recorded using a digital oscilloscope. The discrete Fourier transform of the received signal reveals a centre frequency of 3.1 MHz and a bandwidth of 63%, as shown in Figure 6-10. The receive sensitivity for the 8+8 subset was measured to be 0.87 V/MPa.

After the PDMS film was applied, the same experiment was conducted and the results are shown in Figure 6-11. The measurement results show an increase in centre frequency from 3.1

MHz to 5.7 MHz. The received signal amplitude decreased by 80% while the fractional bandwidth increased to 74%. These losses are mainly attributed to the acoustic impedance mismatch at the PDMS-oil interface and they are reasonable when compared with [6.25]. After thinning, the same measurement, as shown in Figure 6-12, reports a decrease in centre frequency from 5.7 MHz to 4.5 MHz. The received signal decreased by 60% while the fractional bandwidth increased to 82%. A vibrometer check was done after thinning and a fully functional 8+8 array subset was confirmed.

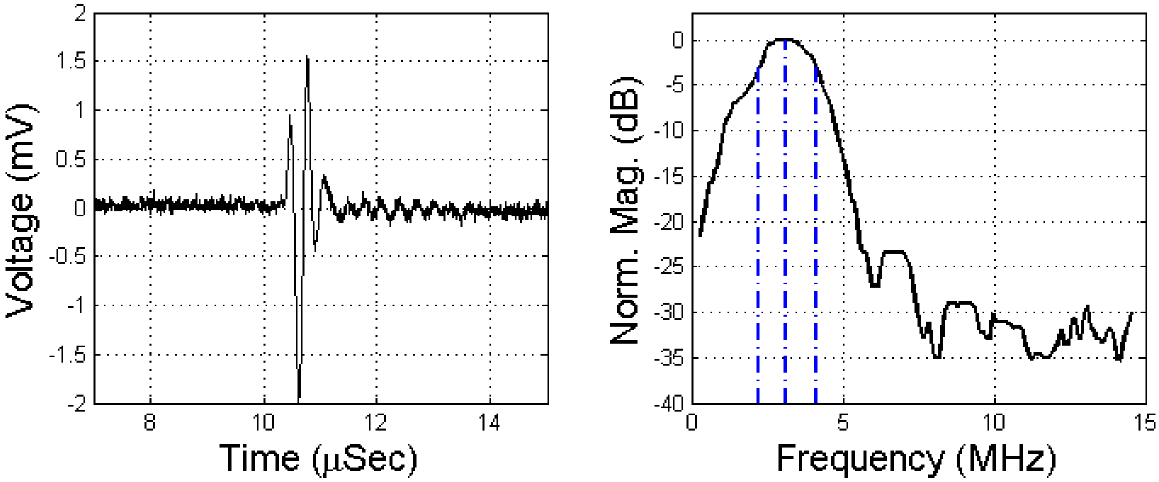

Figure 6-10: Hydrophone measurement and spectrum of a pulse from the simultaneous transmission of 8x8 elements. The centre frequency is 3.1MHz and the bandwidth is 63%.

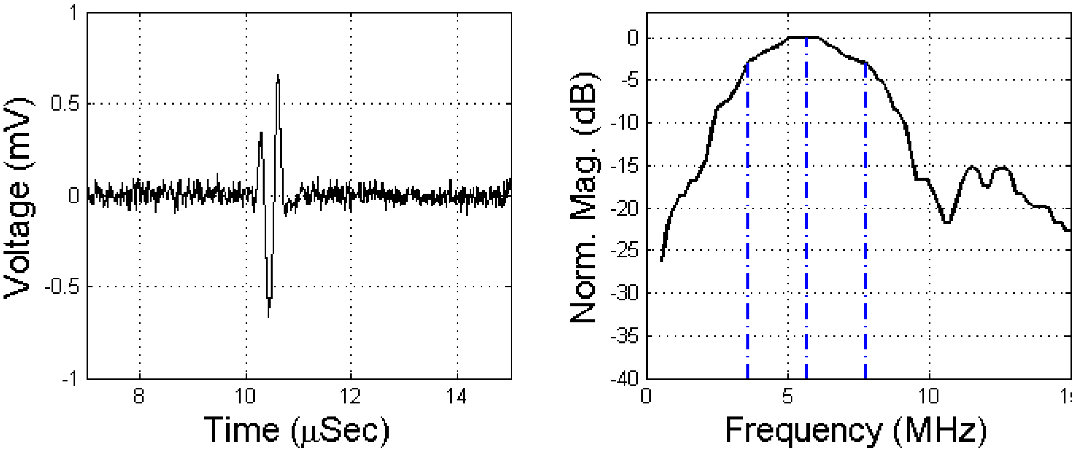

Figure 6-11: Hydrophone experiment after PDMS coating. Transmit power decreased by 80%. Fractional bandwidth is 74%. Centre frequency is 5.7MHz.

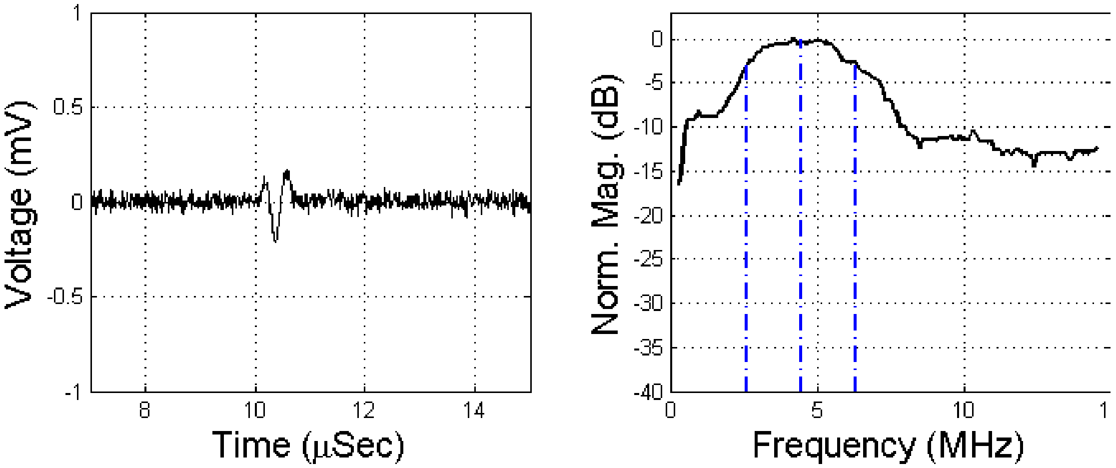

Figure 6-12: Hydrophone experiment after thinning. Centre frequency and fractional bandwidth are 4.5MHz and 82%, respectively.

6.6 Future Work: The Design of a Second Generation Curved CMUT Array

In the first generation transducer fabrication, design consideration for electronics interfacing was minimal since the objective was to thin the CMUT device. Once the device was thinned through wet-etching, it was found that interfacing the device via wire-bonding, even if the bonding was successful, eventually resulted in damaging the contact pads or the substrate given that the substrate was so thin. Even if the contact pads were not damaged, the bonded wires would be damaged under minor deformation.

A second generation design is discussed here: the next iteration should incorporate flip-chip bonding for the interconnection instead of wire-bonds. This new fabrication proposal provides a more robust electrical interfacing solution that can tolerate bending and curving the device. The fabrication process requires the RC-CMUTS to be pre-interfaced to a flex circuit prior to thinning. This is achieved by designing a flexible circuit that matches the contact pad foot-prints of the RC-CMUT with a cut-out that is slightly larger than the underlying CMUT aperture as shown in Figure 6-13. To relief the difficulty in flip-chip bonding, the pitch and contact pads were designed to be rather large (300um+) and the half wave length pitch criterion was not followed. However, considering that the field-of-view for RC-CMUTs is very small, grating lobes are not of primary concern.

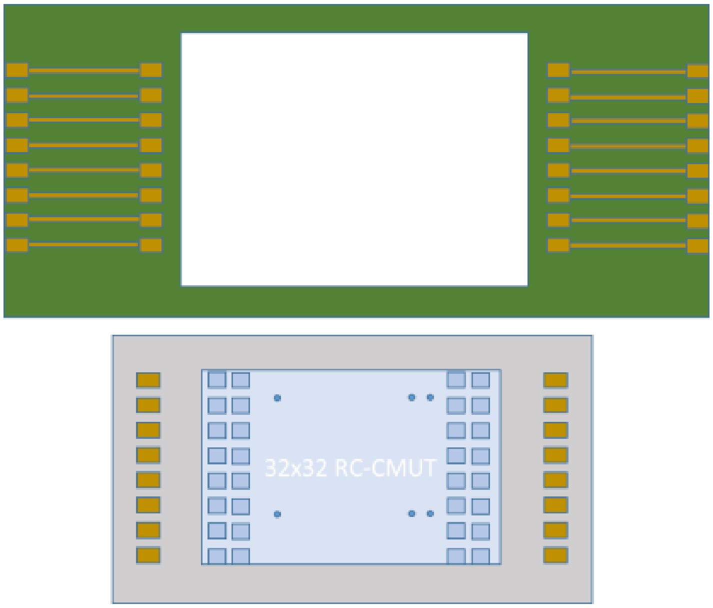

Figure 6-13: (Top) a flexible circuit with matching contact pad footprint as the (bottom) RC-CMUT array is required for flip-chip bonding.

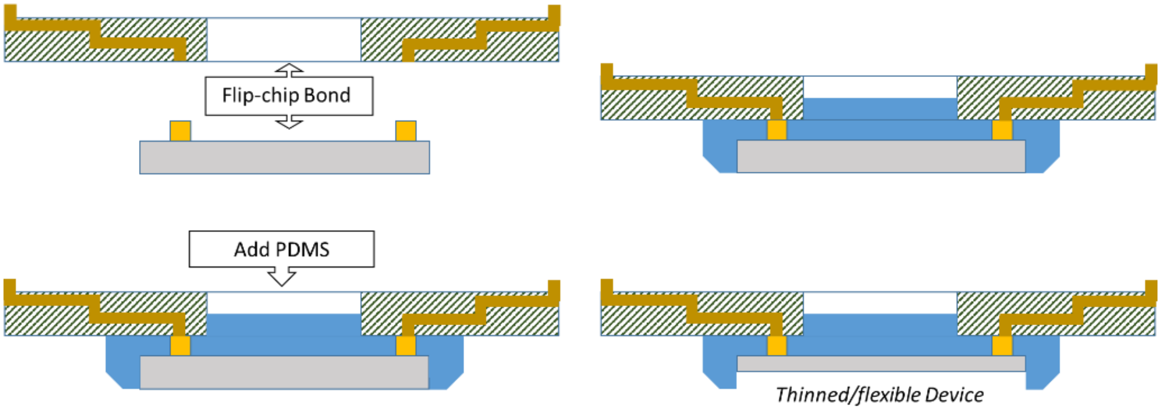

Figure 6-14: A flip-chip bonding can create a more robust device since wire-bond solution are easily damaged.

In the second generation curved RC-CMUT design, several design and process changes were made prior to thinning. First, the row-trench-width was reduced from 30 µm to 10 µm to avoid the back plate collapsing phenomenon. Second, wet-etching of the row-trench during the RC-CMUT fabrication should be avoided as buffered oxide etch (BOE) solution can perforate the photoresist (AZ3312) and attack the underlying oxide layer during prolong etching. More specifically, the BOE creeps through and makes tiny incisions less than 3-µm wide in feature size across the oxide layer. If the incisions intersect the cavities or trenches, they could impact the device performance. One can avoid this issue by using a thick photoresist or switching from wet- to dry-etching. However, in order to etch 500 nm of silicon oxide, one has to be careful of photoresist depletion, especially if an additional 2 µm of silicon needs to be etched with the same lithography step. To minimize photoresist depletion, the oxide RIE recipe (pressure/bias/CF4/O2 = 50mT/-240V/105cc/15cc) can be divided into three 5 minute intervals with additional 5 minute cooling down time between each interval. The added cooling down time dramatically improves photoresist depletion from 200 nm/min to 100 nm/min. Using the same mask and photoresist, the silicon etch can be done using a fast ICP etch recipe (pressure/ICP-power/CF4/SF6 = 50/250V/100/50) where the etch rate is ~1.4 µm/min.

Gold stud bumps can be formed on the aluminum electrode pads on the RC-Array with a ball bonder. The bumping parameters directly affects the bump shape and size. Since height variation between gold stud bumps may cause open circuit, an additional coining process with a flat, or 0-mm-diameter, bonding tool was used to flatten and reduce the height variation to <5um. The RC-CMUT can be picked and placed using a Tresky T-3000-FC3 Die Bonder. A custom-made pick-and-place stainless-steel collet with a 21mmX23mm base is made to ensure an even force distribution. A 15-kg downward force was used to press the RC-Array die against the flex circuit. Thermo- and thermosonic-compression should be avoided since the strong acoustic vibration may damage the CMUT membrane and the flex circuit does not conduct heat well. Next, PDMS (Sylgard 184) is poured into the cut-out of the flex-circuit which exposes the RC-CMUT as shown in Figure 6-14. The PDMS should vacuumed and rested for 3 hrs before heating. This gives time for the PDMS to evenly creep through narrow gap pillared by the stud bumps and also to cover all of the exposed surface except the bottom of the RC-CMUT die as PDMS will inhibit TMAH silicon-etch.

6.7 Chapter Conclusion

Row-column addressing is a simplification scheme that can help accelerate the future of real-time 3D ultrasonic imaging. Yet, without a convex aperture, the performance is highly limited. We have demonstrated a CMUT fabrication and thinning process suitable for row-column addressing. The final device can be fitted on convex probes thus improving the field-of-view, which is highly valued for an RC-CMUT array. The acoustic transmission performance in immersion is measured to verify the functionality of the device. The minimum radius-of-curvature and robustness have yet been determined and will be studied in the future. We are also finding solutions to properly packaging the RC-CMUT for imaging experiment. An extensive acoustic and electrical characterization will also be studied for curved RC-CMUT. Commercial 1-D array finger probes can have a higher frequency (7.5 MHz) than that of the reported. The reported fabrication process should be compatible with higher frequency since element pitch and cell diameter are not critical to the thinning process.

The thinning process is suitable only if there is an inherent masking layer such as the BOX layer used in the double-SOI-wafer bonding process. Processes that use LPCVD nitride as the intermediate layer above the silicon substrate [6.17] may be even more suitable as it is almost completely resistant to KOH and TMAH whereas the BOX layer is still susceptible to being etched during the thinning process. Furthermore, using LPCVD nitride as membrane should improve edge smoothness. Undesirable edge-etching defects are currently visible as some TMAH solution is still able to leak and attack the silicon membrane at the edges as shown in Figure 6-15. Although this manufacturing defect does not extend the aperture, it may lead to crack propagation due to a non-smooth edge. In the next chapter, we introduce a process that is can provide LPCVD nitride as the top layer and will be used which addresses this limitation.

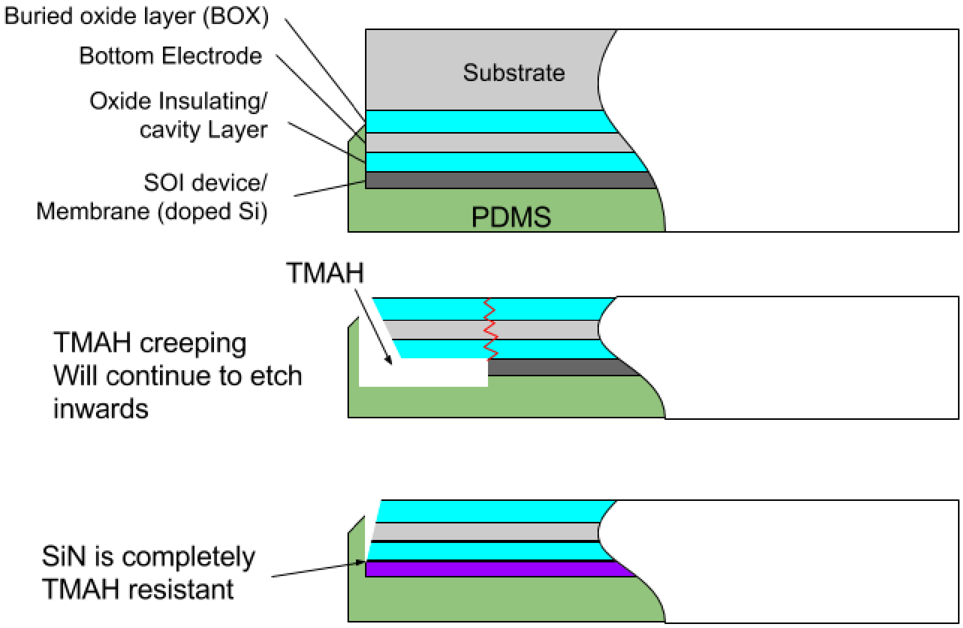

Figure 6-15: Nitride membrane can is resistant from TMAH etch-via-creeping.

Chapter 7 PRACTICAL CMUT FABRICATION WITH A NOVEL NITRIDE-TO-OXIDE BASED WAFER BONDING

At the end of the previous chapter, we introduced the importance of having a nitride membrane for reducing edge defects due to prolong wet-etching. TMAH etch rate for crystalline silicon is typically several hundred nanometers per minute. Given that the thinning procedure takes approximately 20 hrs to etch, it is highly probable to have edge defects that are hundreds of micrometer in size. These edge defects may lead to crack propagation and damage the device especially given the crystalline structure in silicon layer. LPCVD silicon nitride, on the other hand, is completely resistant to wet-etching which should significantly reduce edge defects. In addition, the cost of using two SOI wafers for each fabrication run is rather costly with each wafer costing upwards of 300CAD. LPCVD silicon nitride, on the other hand, can be done through batch process and thus reduce to a fraction of the cost. Unlike CMUTs for catheters, typical imaging probe dimensions run from several millimeters to centimeters. As a result, a single 4-in diameter wafers can yield a dozen or so devices. Although yield is not a priority in research, the thinning process in Chapter 6 does deplete devices rapidly. Also, it is common to have a pair of SOI wafers debond even after high-pressure contact, and the expensive wafers become unusable. This chapter is dedicated to explaining a new process that not only addresses some of the limitations encountered previously but offer a very practical and cost-effective way of making future CMUTs.

7.1 Revisiting Wafer Bonding

Perhaps the most challenging aspect of wafer-bonded capacitive micromachined ultrasonic transducer (CMUT) fabrication is the bonding process, as bonding defects are very common and often lead to device failures. There are various wafer bonding techniques such as direct, anodic, and adhesives-based bonding [7.1]~[7.3]. Given the need for a submicron vacuum gap distance between electrodes and an insulating material with high dielectric strength, direct bonding for CMUT fabrication is the most suitable choice for wafer bonding. The novelty of this paper is to demonstrate a nitride-to-oxide wafer bonding process for CMUT fabrication instead of using the conventional silicon-on-insulator (SOI) wafers as the top bonding wafer (i.e., using the silicon device layer as the vibrating membrane). The objective of this study is to encourage CMUT engineers to consider this process as it is easier and more economical to fabricate compared to the widely-adopted and improved wafer-bonded CMUT process that incorporates local oxidation of silicon (LOCOS) technology [7.4].

One of the earliest reported direct bonded MEMS devices is a pressure sensor with a vacuum cavity [7.5]. Since then, direct bonding processes have gained much popularity with the widespread use of SOI in chip fabrication [7.6]~[7.9]. Direct bonding involves bringing two atomically-clean and flat wafers into contact. This process, often referred to as cold welding or spontaneous bonding, involves the weak force attractions (e.g. hydrogen bonding, Van der Waals forces) at the bonding interface. Direct bonding can become fusion bonding when it is followed by a subsequent annealing process at above 900°C for a prolonged duration to achieve irreversible and covalent bonding [7.10]. Incorporating direct bonding into CMUT fabrication meant that sacrificial layers and holes were not required hence improving the fill-factor and preventing stiction [7.11]~[7.13]. Also, without the constraints of releasing process, cavity depths can be made shallower which improves electrical stability as actuation voltages can be reduced and insulating thicknesses can be increased instead [7.11].

While the conventional wafer bonding with SOI wafer is still a suitable option for fabricating CMUTs, one cannot ignore the advantages of using low-pressure chemical vapor deposition (LPCVD) silicon nitride as a membrane layer. Using a traditional SOI-based wafer bonding process means the breakdown voltage is limited by the thickness of the oxide insulating post. Furthermore, the top silicon plate layer in the area between the cells contributes to parasitic capacitance due to the conductivity of the silicon membrane. Park et al. have incorporated local oxidation of silicon (LOCOS) technology into the CMUT wafer bonding process such that it brilliantly overcomes the two limitations by separating the fixed constraint of gap height and post height. The fabrication complexity of LOCOS process, however, is considerably higher. Many steps are added to the conventional wafer bonding process [7.11] including growing and etching oxide and nitride layers while carefully minimize the impact on roughness on the post surface [7.4].

In 2009, our group reported a nitride-to-nitride wafer bonding CMUT fabrication process [7.14]. The acoustic and electrical results were very promising but much of the fabrication cost was attributed to the chemical mechanical polishing (CMP) process, which is necessary to reduce the nitride surface roughness for direct bonding [7.15]. Moreover, the polishing pads and slurry solution had to be replaced frequently with each batch, which can cost up to several thousand dollars. In addition, polishing quality is typically inversely proportional to pattern density [7.16]. Therefore, polished patterned-wafer (i.e. the bottom wafer) often has a higher surface roughness than unpatterned wafer which contributes to bonding failure [7.15]. Recently, we revisited the nitride wafer bonding process and investigated ways to improve the fabrication process. First, the feasibility of bonding nitride surfaces without CMP was investigated. LPCVD nitride films that are ≤ 10 ÅRMS in roughness should bond as we have previously bonded 8-ÅRMS nitride films [7.15]. Yet, it was not obvious why ≤ 10-ÅRMS nitride films without CMP cannot bond. Second, Usenko and Senawiratne reported nitride-to-glass bonding for making a more reliable barrier against drift or diffusion of impurities for silicon-on-glass substrate. They found that prolonged exposure to oxygen plasma can convert the top part of the silicon nitride film into several nanometers of silicon oxynitride and silicon dioxide while reducing the surface roughness [7.17]. Hence, roughness and ellipsometry studies were conducted (see Section 4) to verify the effects of oxygen plasma on nitride surfaces. Finally, we contracted a specialized CMP lab to outsource the complex and otherwise costly process. It is not rare for academic campuses to have a CMP machine but they are typically for the purpose of planarization of multi-layer CMOS or MEMS devices rather than to promote angstrom level roughness. The final outcome of our studies allowed us to bond a nitride wafer to thermal oxide wafer, which has not yet been reported to the best of our knowledge. The ability to use a nitride membrane and bond to a patterned oxide film promises compatibility with majority of the reported bonding processes [7.18]~[7.25] and can thus benefit many of the existing processes.

In the next section, wafer bonding considerations will be examined. In section 7.3, the novel nitride-to-oxide bonding process will be presented. Section 7.4 includes the results. The discussion and conclusion are given in sections 7.5 and 7.6 respectively.

7.2 Direct Bonding Considerations

Direct bonding is challenging because of the requirement of having smooth and contaminant free surfaces. Even if a micron level particle is present (e.g. contamination), it may lead to a void creation or prevent bonding at the interface. In standard fabrication, smoothness is quantified through root-mean-square (RMS) roughness by scanning with an atomic force microscope. A typical virgin prime silicon or SOI wafer that is polished by the manufacturer will have a surface roughness of 3~7 ÅRMS. If the same wafer undergoes thermal oxide growth in a furnace, the roughness typically stays the same. In most literature, wafer bonding is stated to require a surface roughness of 5~10 ÅRMS [7.6]~[7.9].

7.2.1 Surface Roughness and Nanopillars

Sometimes even when a wafer is thoroughly cleaned, contamination could be introduced during deposition. As an example, we had deposited and attempted to bond a pair of identical wafers with 400-nm-thick, PECVD silicon-rich nitride film that has a roughness of 10 ÅRMS. These nitride wafers debonded immediately even though spontaneous bonding should have occurred given the roughness requirement. It was eventually observed that a few micron-sized contaminating particles were constantly present after the deposition. This is because PECVD is inherently subject to contamination due to the strong electric field within the chamber that can attract charged particles that were settling on the electrode or chamber wall and redeposit them onto the cleaned wafer [7.26][7.27].

Even without contamination, the topography of the deposition film can prevent bonding. As an example, we had deposited a 500-nm LPCVD nitride thin film (Tytan 4600 Mini Fourstack Horizontal Furnace, TYSTAR) and the roughness was measured to be ≤ 10 ÅRMS. After the wafer bonding step, the wafers debonded immediately prior to annealing. A further AFM study showed that 10-nm tall nanopillars were scattered throughout a scan area. When a 200-nm thick silicon rich nitride film was deposited and scanned (see Figure 7-1), the nanopillars are still scarce and short enough such that the nitride wafers can still bond [7.28]~[7.30]. With the same deposition conditions but at 600-nm thick the roughness increased from 7 to 10 ÅRMS. More importantly, the distribution and size of the nanopillars increase drastically as shown in Figure 7-1. Both the size and frequency of the nanopillars can significant reduce the bonding contact area. This explains why, without CMP, it is extremely difficult to bond thicker nitride films even though there is no significant increase in roughness over thinner films.

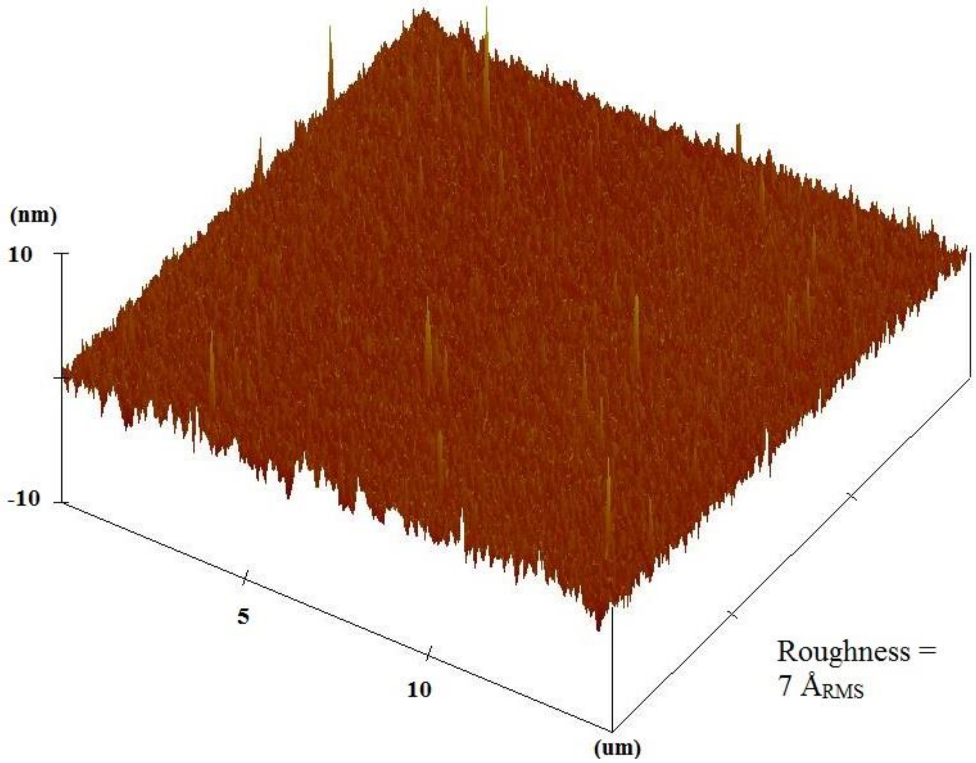

Figure 7-1: The AFM scan shows a surface roughness of < 10 ÅRMS which is acceptable for achieving spontaneous bond. There are very few 10-nm nanopillars but at this thickness it is still bondable.

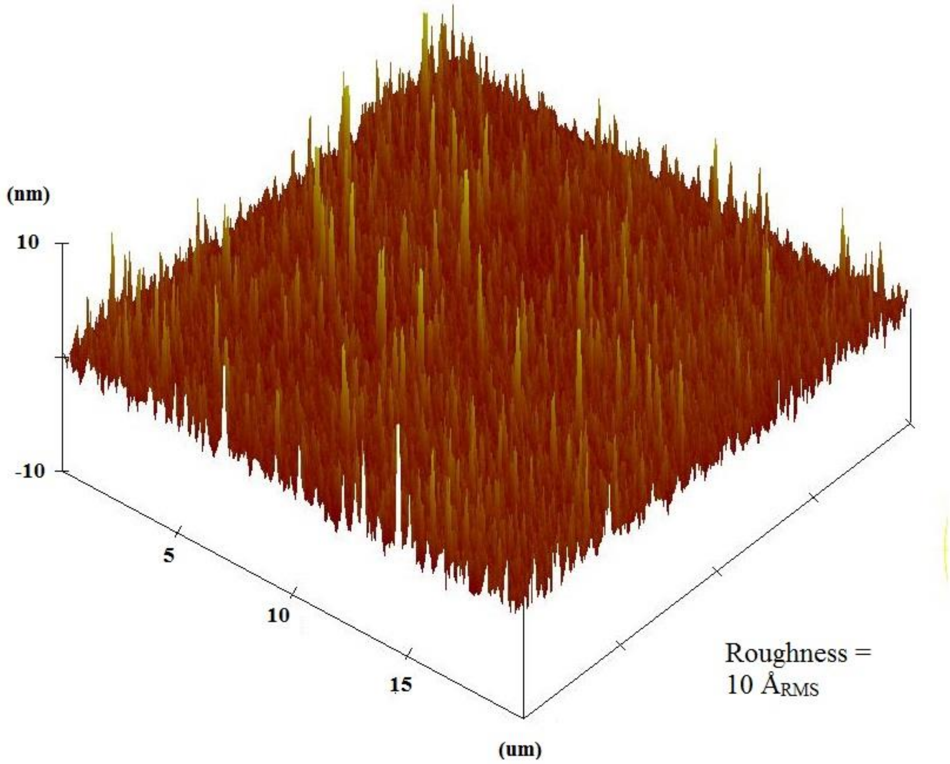

Figure 7-2: Although RMS roughness did not increase significantly at 600-nm thick deposition, the pillars are much more noticeable in size and frequency. These large pillars are attributed to bonding failures of thicker nitride films.

In addition to surface smoothness and flatness, the surface oxide seems to play an important role. Though this concept still requires much investigation, several groups have correlated the mechanism. Usenko and Senawiratne managed to bond nitride to oxide after converting the top silicon nitride layer into silicon oxynitride [7.17]. Reck et al. have noticed a higher bonding strength when two wafers with thin nitride films are purposely oxidized compared to films that are BHF treated [7.29]. Although not mentioned, this phenomenon can be seen in the void-free direct bonding of CMUT array fabricated by Christensen et al. as they bonded two silicon oxide wafers [7.31].

7.2.2 Problem with Current SOIs

The standard wafer bonding process for CMUTs employs SOIs, which are created with traditional wafer bonding techniques where a thin silicon wafer is bonded to a bottom thermal oxide wafer. The backside of the silicon wafer is then grinded and polished with a CMP to achieve a thin and ultra smooth device layer. A problem arises in this polishing process as CMUT fabrication requires a device layer that ranges from several hundred nanometers to less than 3-μm thick. The device layer's thickness uniformity is usually very poor due to the rotational polishing nature of CMP. Ultrasil, one of the world's largest SOI providers specifies an intra-wafer minimum thickness variation of ± 0.5 μm, which is far from ideal. As an example, medical imaging CMUTs typically have a membrane thickness of around 0.5~2 μm and a cavity diameter of 30~60 μm. A minimum thickness variation of ±0.5 μm could mean that within the same batch of CMUTs, some could be 1-MHz higher in resonant frequency than the other while some membranes could be too thin and collapse. Most often, CMUT geometries are designed such that the performance is compromised in order to accommodate the thickness variation. This issue was originally not a problem for researchers until companies like Soitec discontinued SIMOX-based technology for smaller (4”~6”) wafers that can guarantee thin (< 1 μm) and ultra uniform (< 5 %) SOI wafers.

7.2.3 Good Practices for Silicon-to-Oxide Bonding

Since the cleanliness of the wafers is paramount to bonding, utmost care must be taken prior to bonding. There are some minor variations among CMUT academic groups on wafer cleaning. Huang et al. reported using a 4:1 Piranha for 20 minutes, followed by a 50:1 HF 15-seconds dip, then a RCA-1 treatment for 5 minutes [7.11]. Logan et al. reported using a standard RCA-1 and RCA-2 bath, a low power oxygen plasma descum, followed by another RCA 1 [7.14]. Given that metallic contamination should not be present in the early process and only virgin prime wafers were used, our group uses RCA 1 cleaning for 5 minutes followed by 5 minutes of continuous rinsing with DI water. In most cases, the likely cause of voids is the environment exposure between RCA cleaning and bonding. Even drying with a nitrogen gun at the bench could introduce micron level particulate to land. In our group, the wafers are immediately spin dried at high speed (one can use a standard spinner) after the DI-water rinse, then sealed in a thoroughly cleaned wafer holder to reduce exposure to air particulate. The bonding chamber (AWB 04, AML) is pre-cleaned by a thorough IPA wipe. Wafers are then carefully and swiftly secured in the chamber with visual inspection to ensure that no dust has landed on the wafer (one must wear a mask). Once the lid is closed, an in-situ radical activation (i.e. oxygen plasma) was activated for 15 minute followed by bonding at 3000-kN of force in 0.8-μBar high vacuum at room temperature. The plasma is used to promote surface silanol groups which increase bonding strength without increasing surface roughness [7.32]. Bonding yield has been consistently above 90% (i.e. one or two voids with 1-cm diameter) since these guidelines were followed.

7.3 Nitride-to-Oxide Wafer Bonded CMUT

The parameters of the reported CMUTs were designed for collapse-mode operation. The membrane was designed to collapse at low bias voltage (< 15V) such that deep collapse studies can be conducted in the future without using a high bias. The process, as shown in Figure 7-3 should be indifferent for a conventional CMUT design since the bonding should be independent of nitride film thickness and cavity size. The process is as follows:

A 600-nm low-stress nitride was deposited (Tytan 4600 Mini Fourstack Horizontal Furnace,TYSTAR) on a standard RCA-1 cleaned, 4", 500-um thick prime wafer (handling layer). Tool acceptance specification on the low-stress nitride recipe shows n=2.30, < 100MPa compressive stress, < 5% intra-wafer uniformity, < 10% wafer-to-wafer uniformity. After the batch deposition, the polishing of the wafers was outsourced to the contracted polishing lab (3IT.NANO, Université de Sherbrooke). CMP was done using an Alpsitec E460E with a 50-nm colloidal silica slurry with a pH of 9.6. Specifications were made and verified based on a roughness requirement of < 10 ÅRMS and a thickness variation of < 5%.

The bottom handling wafer is the bottom electrode and the patterned cavities on thermal oxide is fabricated as follows. A prime 4" highly doped (<0.01Ωcm), <100> orientation, single side polished wafer is used. A 500-nm oxide film is wet-grown in a furnace (Tytan 4600 Mini Fourstack Horizontal Furnace, TYSTAR). Next, a lithography step is done to pattern the cavities and a subsequent RIE dry etch step is used to etch out the 190-nm deep cavities. Prior to bonding, the wafers are RCA 1 SC-1 cleaned with 5:1:1 recipe for 5 minutes and DIW rinsed for 5 minutes followed by 20 minutes of oxygen plasma. Next, the wafers are brought in contact with a 4" wafer bonder (AWB 04, AML) at 3000-N of force and at 6E-4 mBar for 30 minutes. The bonded wafers are then annealed at 1100°C for an hour. The wafers are then immersed in TMAH solution until the top handling layer is completely removed. Since the bottom wafer has 500-nm of oxide covering the layer, only the top handling layer is etched. Once the wet etching is finished, a lithography step and a dry etch step is done to expose bottom electrodes through RIE. Finally, an e-beam process is done to deposit 30-nm of chromium to promote adhesion followed by 70-nm of aluminum as electrodes for wire-bonding. This process uses 3 masks only and is highly compatible with the existing processes used in conventional CMUT fabrication. The CMUT parameters are listed in Table 7.1 A picture of the final diced device is show in Figure

7-4. The micrograph and SEM image of the fabricated device are shown in Figure 7-5 and Figure 7-6.

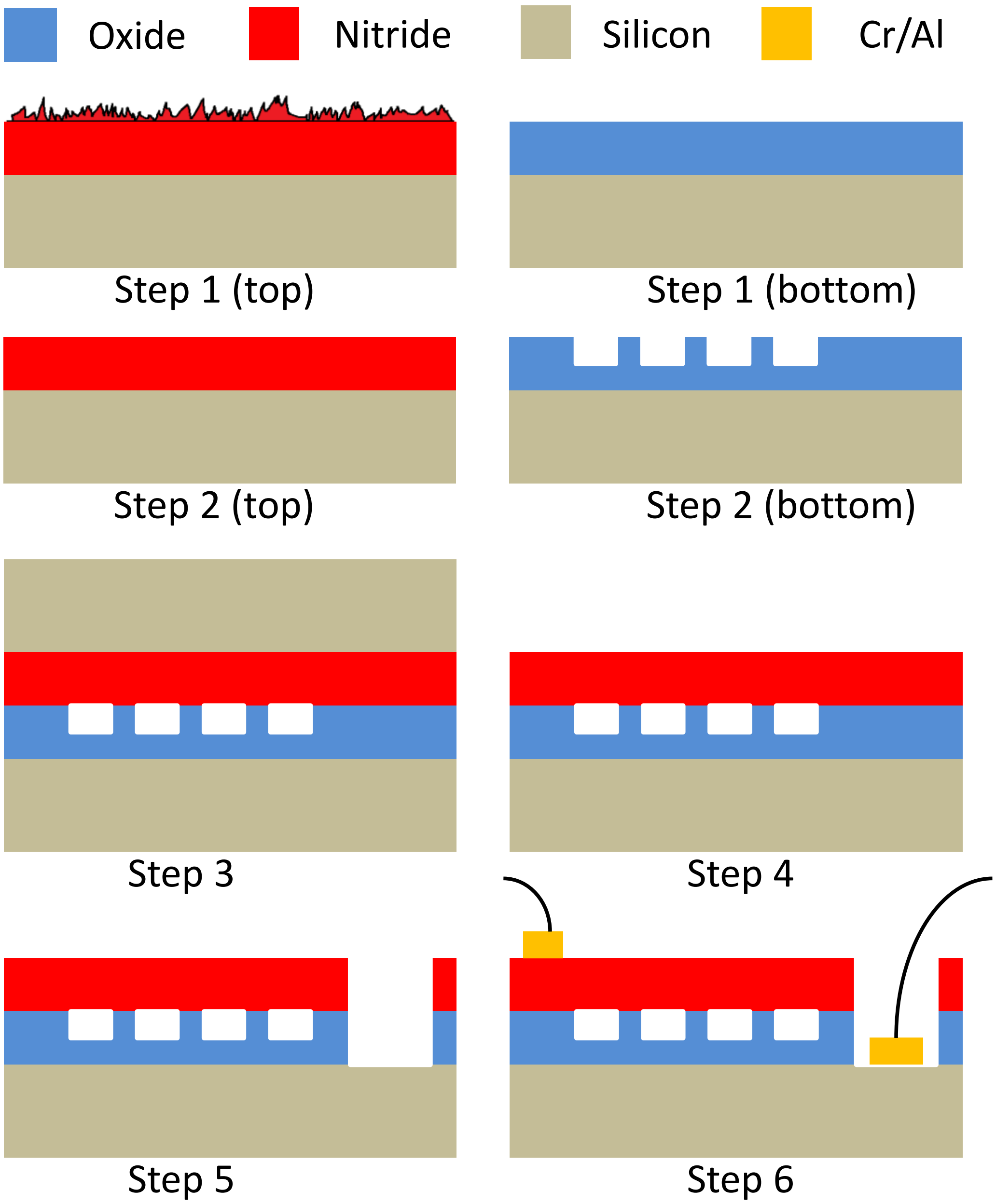

Figure 7-3: Fabrication Flow.

TABLE 7-2: DESIGN PARAMETERS FOR 4.7-MHZ, 16-ELEMENT CMUT ARRAY

Membrane Thickness (nm)	450
Electrode Diameter (μm)	30
Cavity Diameter (μm)	50
Cavity Depth (nm)	190
Insulation Layer Thickness (nm)	310
Element Length (mm)	6

Element Width (µm)	380
Cell per Element	880
Element Pitch (µm)	400
Cell-to-Cell pitch (µm)	55

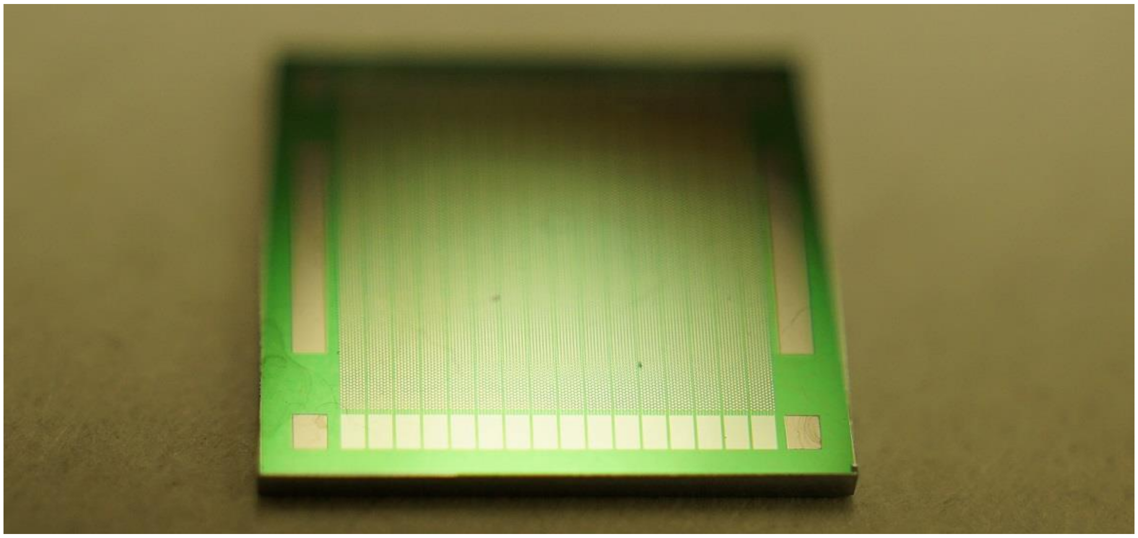

Figure 7-4: An 1-D 16 element CMUT array with 6-mm by 6-mm aperture.

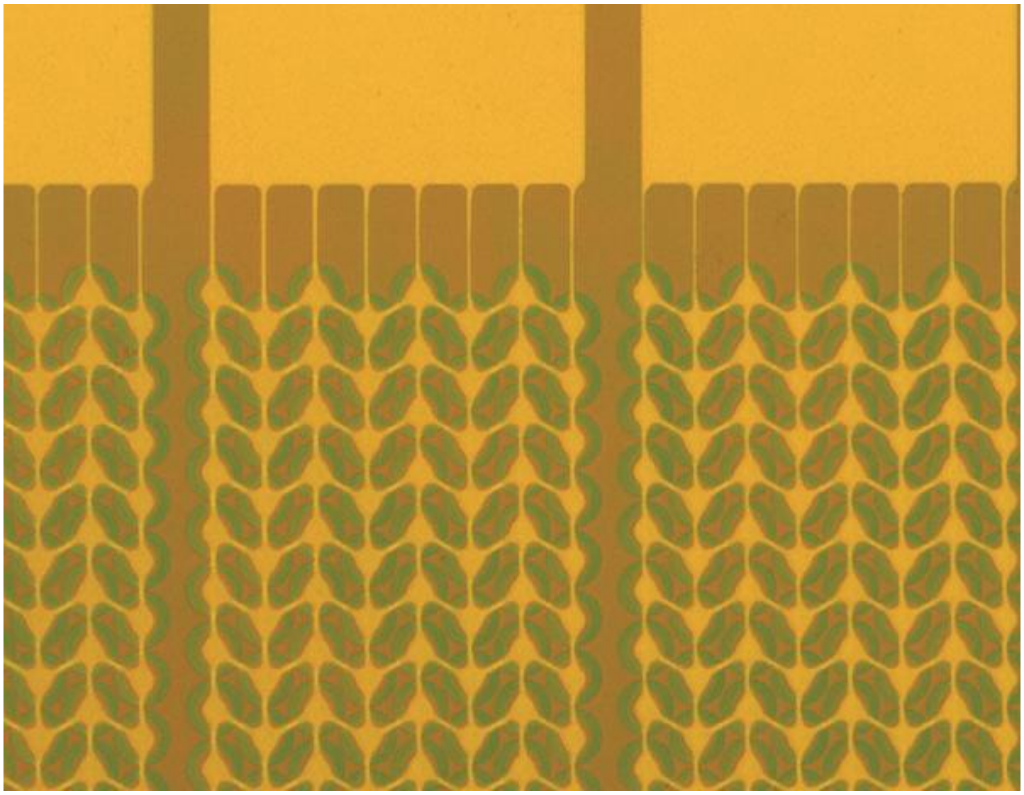

Figure 7-5: Micrograph of fabricated CMUTs. Each element is 380 µm wide.

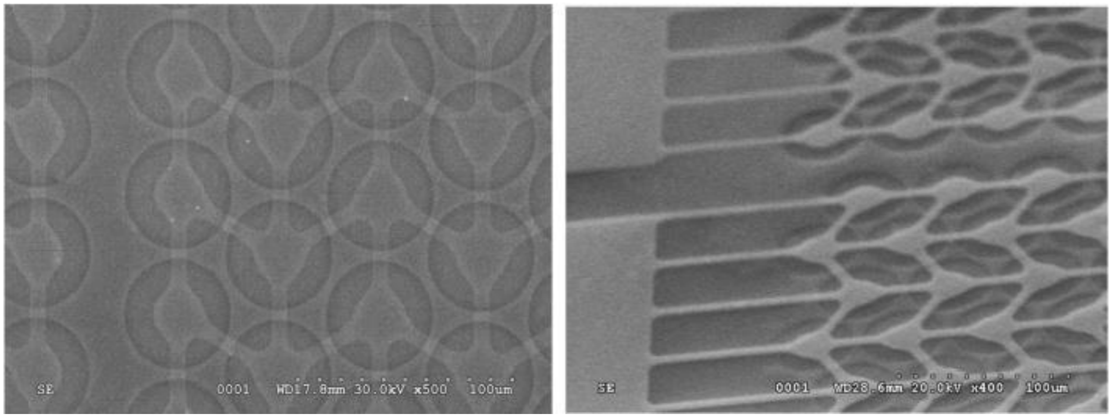

Figure 7-6: Scanning electron microscopy of CMUTs

7.4 Characterization and Results

Prior to the CMP, the wafers were randomly selected from the same LPCVD silicon nitride batch and the roughness at five different points were measured to be in the range of 9~10- ÅRMS. Although this roughness should be acceptable for direct bonding, there were several pillars over 10-nm tall, as discussed in Section 7.2.1, that can prevent bonding. After CMP, the surface is noticeably smoother with no trace of any pillar and the surface roughness decreased to 3~5- ÅRMS as shown in Figure 7-7.

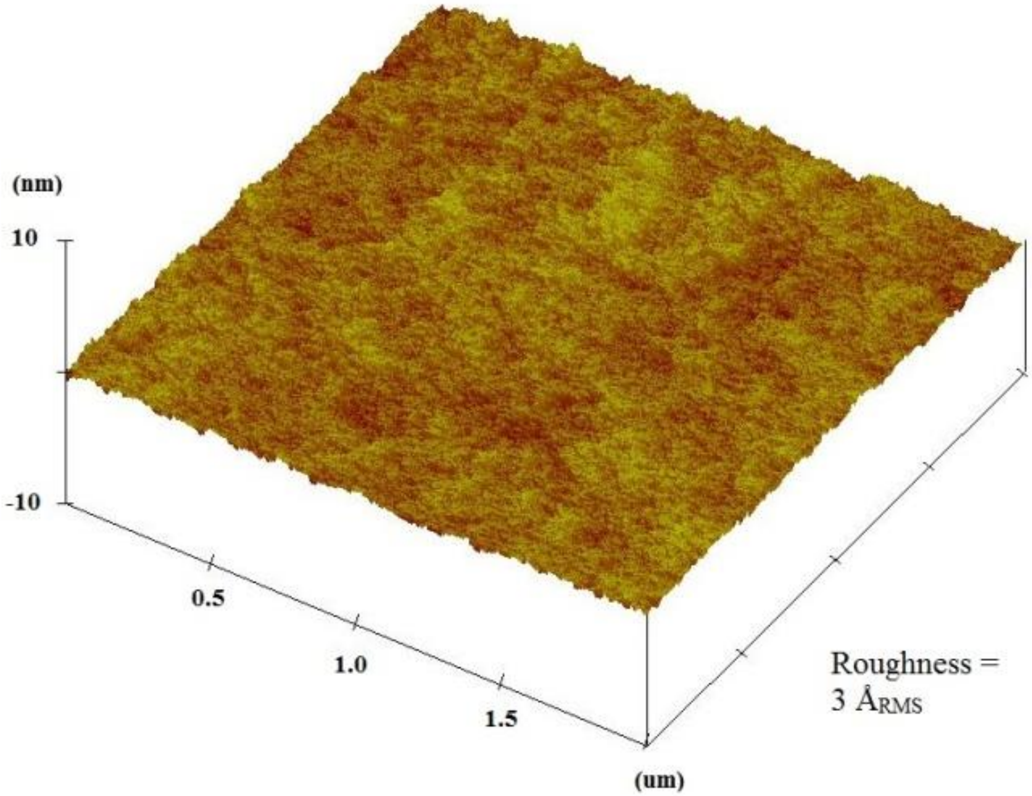

Figure 7-7: After CMP, the nitride film is successfully flattened. Pillars are no longer noticeable and roughness dropped to 3ÅRMS.

To verify the surface oxide presence and also roughness after plasma, ellipsometry was used before and after a 20-minutes oxygen plasma treatment. A Cody-Lorentz optical model (MSE < 5) is used on the ellipsometry data (Woollam M-2000 Model DI, J.A. Woollam Co.) and the before and after silicon oxynitride thickness were determined to be 5 Å and 9 Å, respectively, on the silicon rich, low stress SiN film. Meanwhile, the roughness remains unchanged.

Two nitride-to-oxide pairs were bonded. After bonding and releasing the first bonded pair, a 60% bonding area was found. The cause of the low yield on the first pair was not certain but it was likely caused by slurry residue contamination. Therefore, the second bonding process involved an additional RCA-2 step after RCA-1 which remove metal contamination. This subsequent step is followed by another RCA-1 to ensure the surface was hydrophilic. The second nitride-to-oxide bonding yielded 90% which suggests that metal contamination could likely be the cause of the low yield in the first run. Metal contamination is common in the CMP process and RCA-1 and -2 cleaning is highly recommended post polishing [7.33].

After bonding, a vibrometer (Polytec OFV-5000, DD-300 displacement decoder) was used to characterize the collapse-mode vibration in air. The frequency was measured to be 10.25 MHz with a ± 2 kHz variation across 5 devices on the same wafer. A 2-D scan is shown in Figure 7-8. Areas indicated by red hue represents the higher displacement at close to 40 nm, which is reasonable for collapsed-mode. However, the primary vibration is concentrated on a quadrant of the cell rather than evenly distributing to that of a doughnut shape. The cause of the uneven distribution can be attributed to the asymmetry and minor misalignment in the electrode branches layout.

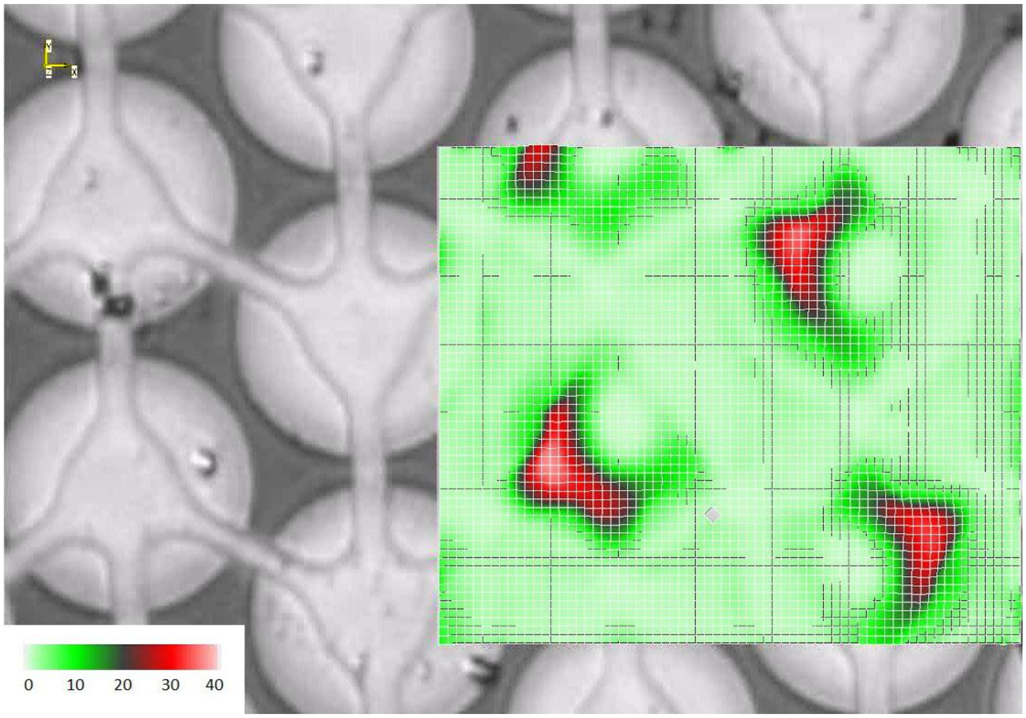

Figure 7-8: Vibrometer displacement measurement of collapsed mode at +30-V bias with 10-Vpp AC signal at 10.25MHz.

An electrical impedance characterization with a vector network analyzer (Rohde & Schwarz ZNB-20 VNA) was also done to see the effect of bias voltage, collapse voltage, and frequency shift. As shown in Figure 7-9, the collapse occurs at 15 V. Figure 7-10 shows a larger scale.

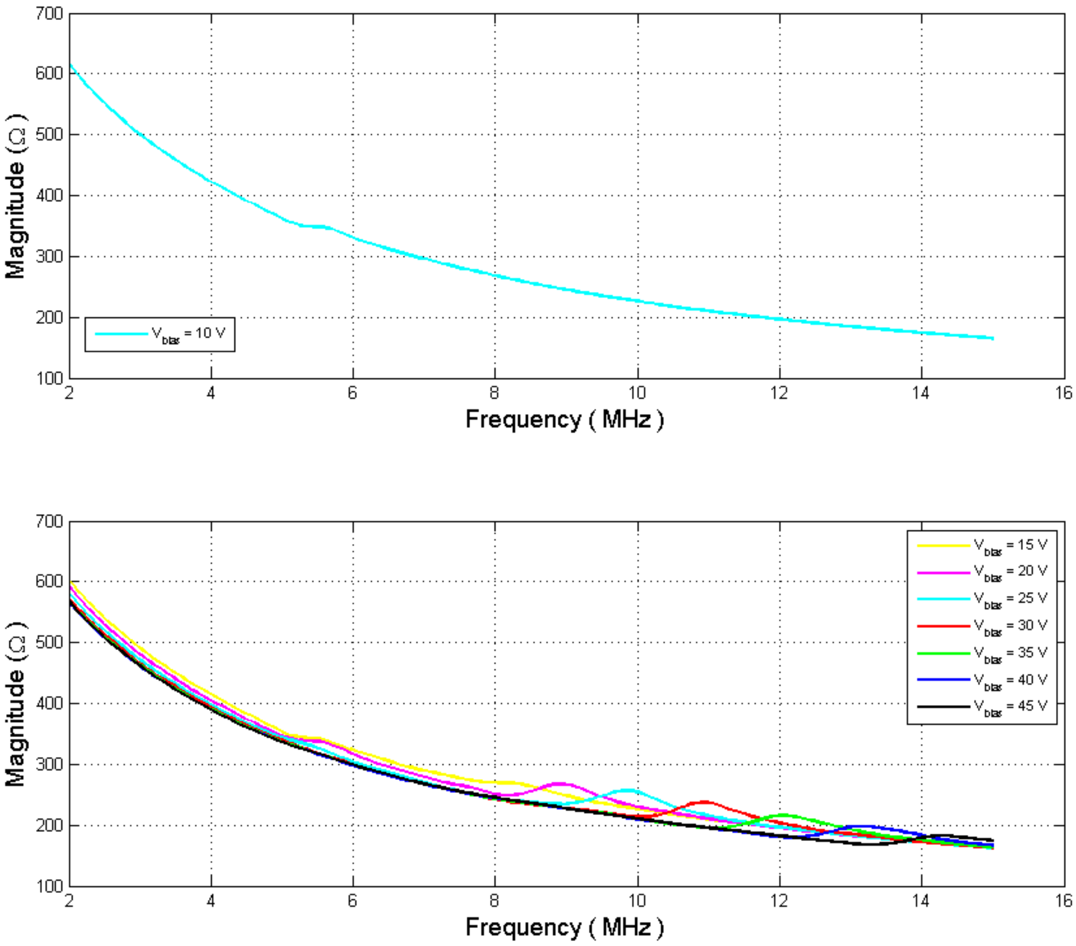

Figure 7-9: Impedance Measurement of (top) pre-collapse and (bottom) collapse-mode operation.

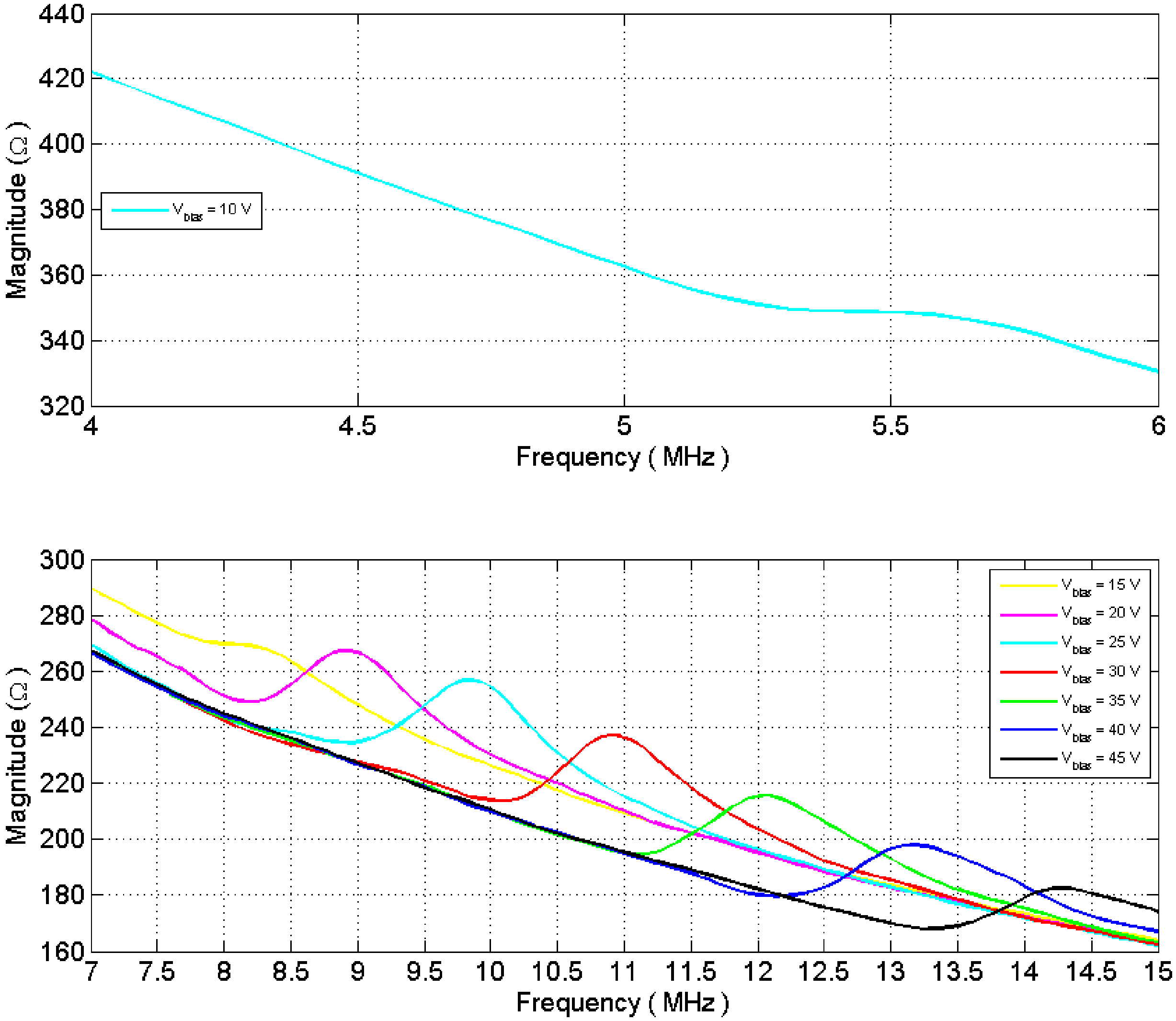

Figure 7-10:A closer look at impedance Characterization

The resonant frequency in air for pre-collapse is about 5.5 MHz. At 15 V, the membrane collapses and the frequency immediately shifts to close to 8.2 MHz. There is a consistent frequency increase with increased bias voltage at collapse mode. This can be explained by the fact that with increasing bias voltage, the membrane-to-bottom contact area increases and is similar to reducing the radius of the vibrating membrane – which increases the vibrating frequency. Figure 7-11 shows the corresponding phase.

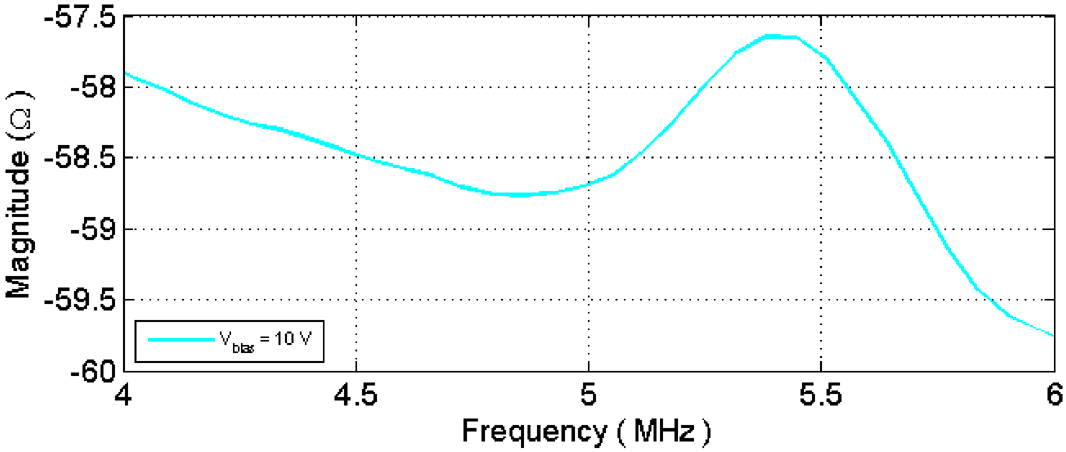

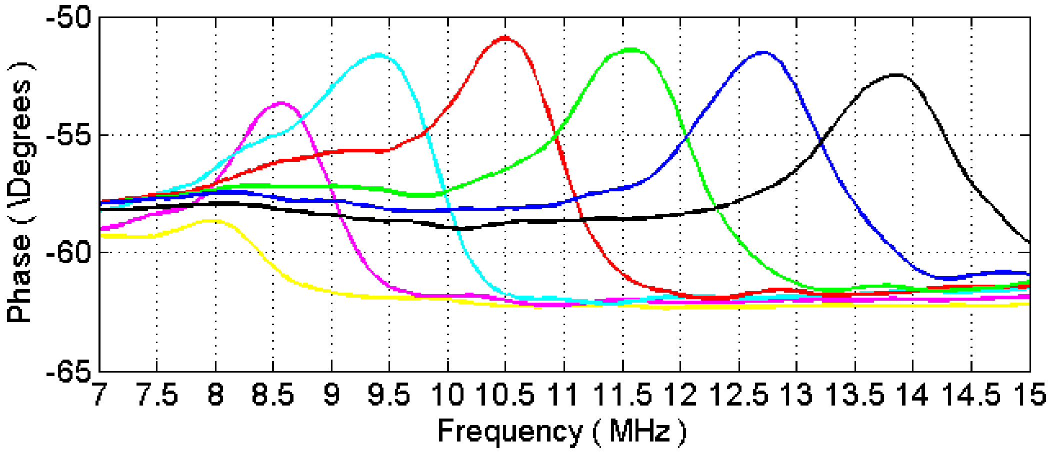

Figure 7-11: Phase of impedance

Immersion performance was also characterized. First, a CMUT-for-transmit experiment was conducted in vegetable oil where all 16 elements of the CMUT array was pulsed simultaneously while biased at 15 V. A commercial pulser (Panametrics NDT 5073PR) was used to pulse the CMUTs while acoustic signals were captured by a hydrophone (Onda HGL-0200) with signal amplified by a pre-amplifier (Onda AH-2010) before measuring by an oscilloscope. A CMUT-for-receive experiment was followed where 4 elements of the CMUTs were activated for receiving using a transimpedance amplifier circuit with a 10-kΩ feedback resistor. A commercial piezoelectric transducer (Panametrics-NDT V327-SU) driven by a commercial pulser/receiver (Panametrics 5073) located 40-mm away was used to generate acoustic pulses. The captured data for both tests are shown in Fig. 8 and Fig. 9 along with the corresponding Fourier transforms. Pressure at 40-mm was measured to be 0.47 MPa.

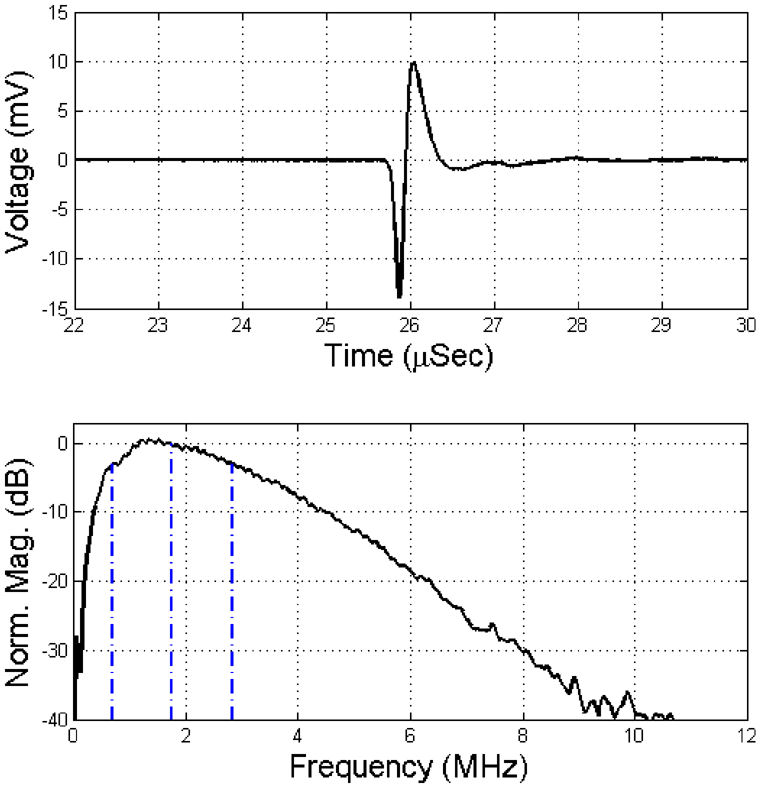

Figure 7-12: Determining transmit spectrum using hydrophone as receiver at 40-mm away. Center frequency is 1.7 MHz with a 122% -3-dB fractional bandwidth.

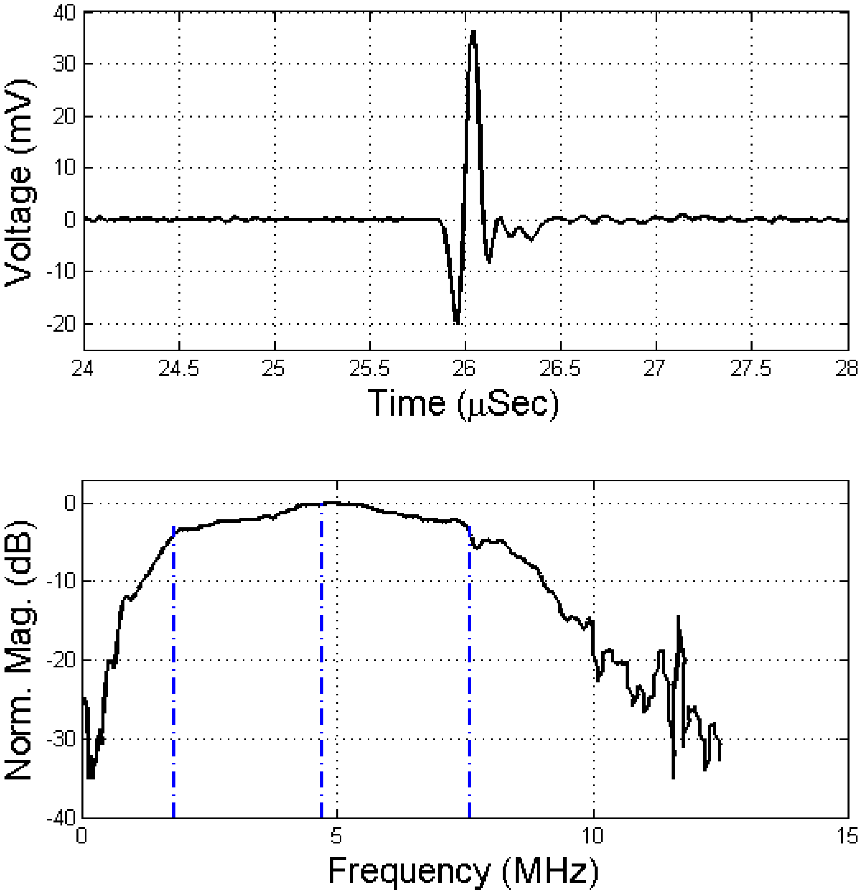

Figure 7-13: Receive test with commercial pulser as source and CMUT as receiver at 40-mm away. Centre frequency is measured to be 4.7 MHz with a 124% -3-dB fractional bandwidth.

A pulse-echo test is also set-up using a custom-made transmit and receiving circuit. A unipolar pulsing circuit is made with two sets of high voltage switches with a 200-ns width and a 25-V amplitude. The receiving circuit uses OPA354 in a transimpedance set-up with 10-kΩ gain and a 0.4pF feedback capacitor. A Spartan-3 FPGA board is used to trigger the pulser circuit and controlling the pulse width in addition to syncing the Tx-Rx switch. An 8-cm thick aluminum slab is placed 5-cm in front of the CMUTs and the received signal is shown Figure 7-14.

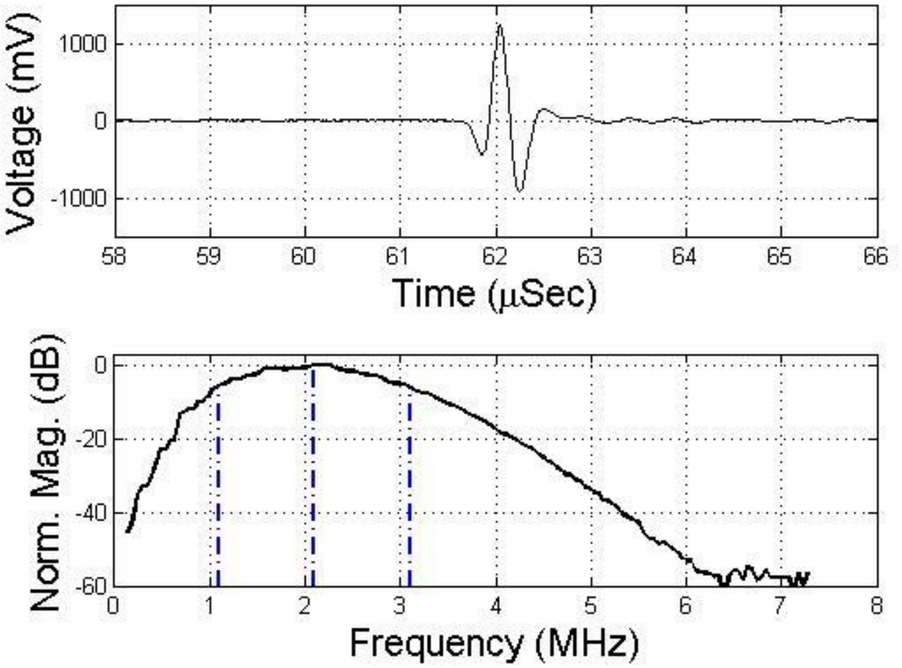

Figure 7-14: Pulse-echo waveform. Centre frequency is measured to be 2.1 MHz while -6-dB fractional bandwidth is 100%.

With the same pulse-echo circuit, an A-line test was done in oil with a 10-mm thick aluminum plate positioned 50-mm away from the 4-element transducer. The A-line oscilloscope data, as shown in Figure 7-15, shows the reflection of the front and the back face of the aluminum block with a separation time-width of 3.2µs. This accurately measures the two-way distance of the 10-mm thick aluminum plate given that the speed of sound travels at 6320 m/s inside aluminum (6320 m/s * 1.6 us = 1 cm). The reflected signal of the back plate shows a 20-dB drop from that of the front plate which is reasonable as some acoustic energy is attenuated and scattered within the aluminum plate while some energy is loss due to impedance mismatch.

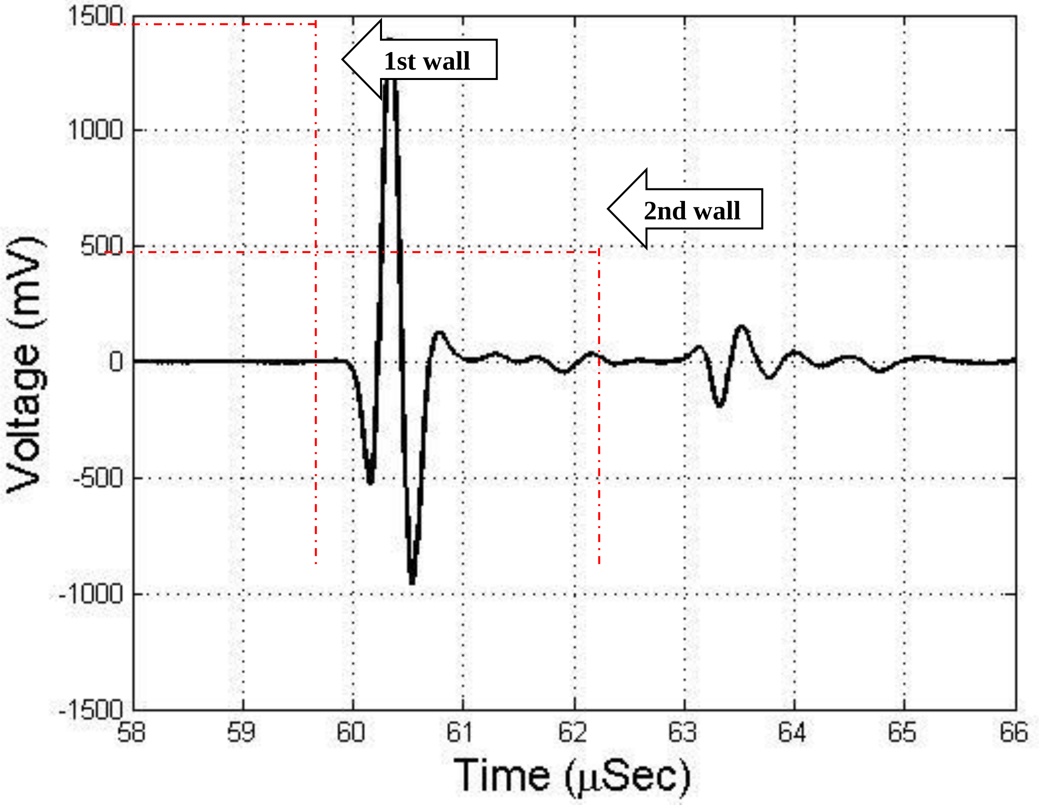

Figure 7-15: Thickness detection of aluminum block.

7.5 Discussion

It was found that the reason for bonding failures for thick (>400-m) nitride films is likely due to the growths and spreads of nanopillars during deposition. Although RMS surface roughness is the primary gauge of bonding success, yet this metric does not clearly reflect the recurrence and size of nanopillars. The nanopillar phenomenon explains why nitride films that are ≤ 10 ÅRMS fails to bond contrary to common understanding. Moreover, if a 5-µm×5-µm AFM scan was done to identify the RMS, one can easily miss the nanopillars, and thus it is important to scan a larger area to identify nanopillars. Nevertheless, CMP is necessary for the removal of these pillars and secure bonding for thicker films.

The oxygen plasma treatment showed a growth in surface oxide thickness from 5 to 9 Å which shows agreement with [7.17]. The surface roughness remained at 3 ÅRMS, which is expected as roughness is already near the molecular limit. It is difficult to conclude if the oxide thickness has a significant impact in bonding strength as it also promotes surface dangling bonds which are necessary for strong bonding. Future study can be conducted to compare surface oxide thickness and bonding strength.

The vibrometer characterization showed good consistency across both intra- and inter-element cells as expected from a wafer-bonded CMUT. The <5% thickness variation of nitride membrane after the CMP is reflected on minor frequency variation across the wafer. The immersion transmit and receive performance is comparable to that reported by Logan et al. in terms of transmit and receive power [7.14]. The receive mode showed a centre frequency of 4.7 MHz while the -3-dB fractional bandwidth is 124%. The transmit mode did not agree with the receive mode as the spectrum seem to represent the non-collapse-mode operation despite the collapsed-membrane. It is possible that the whole membrane still managed to vibrate during the pulse even though it was collapsed. Future work will include the impact of top electrode branch design on collapse-mode vibration distribution.

The cost of polishing a batch of nitride wafers (< 25 units) was 1500 $CAD. This means a ready-to-bond silicon nitride wafers cost approximately 15 $CAD/wafer (prime wafer cost) + 400 $CAD/25 wafers (LPCVD Nitride deposition) + 1500 $CAD/25 wafers (CMP) = 91 $CAD/wafer. Relative to a commercial SOI wafer, our wafer cost is approximately a quarter of the cost for a SOI wafer. Avoiding the use of silicon membrane also means that the use of LOCOS oxidation process is not needed which saves additional lithography steps, masks, and high temperature operation, thus dramatically simplifying the fabrication process. However, the LOCOS process does provide tight vertical tolerances (<10-nm) gap and insulation height control compared with the reported process since the cavity and insulation thickness is controlled by thermal oxide growth rather than dry-etch. Nevertheless, this CMUT fabrication process combines the merits of the traditional surface fabrication process, which include a lower parasitic capacitance, with the merits of wafer-bonding process such as higher fill-factor, better uniformity, and stiction-free devices. Although the LOCOS method can improve the parasitic capacitance and breakdown voltage, it requires significantly more processing time. More importantly, ultra-uniform SOI wafers are becoming scarce, not to mention very costly, as manufacturers with SIMOX technology are shifting towards ≥ 200-mm wafer production. Meanwhile, non-SIMOX-based SOIs have poor device layer uniformity and the thickness selection and availability are limited. In contrast, the nitride-to-oxide wafer bonding approach ensures a uniform membrane thickness which allows a better tolerance control.

7.6 Chapter Conclusion and Future Work

This chapter reports a new CMUT fabrication process with nitride-to-oxide wafer bonding. The reported process requires only 3 masks while the CMP process is outsourced as maintenance of the equipment for angstrom level smoothness is not practical for many academic labs. The devices resulting from this fabrication process are very promising and the process should be compatible with many existing SOI-wafer bonding processes. Since SOI wafer availability and quality are limited, the benefit of using nitride membrane for wafer bonding should be revisited by the CMUT community.

Future work should apply the reported fabrication technique to make curved RC-CMUTs and consider incorporating collapse-mode design to enhance performance. Since the membrane is non-conductive, only 4 masks and lithography steps are needed which reduces fabrication complexity and lower cost. As discussed in Section 6.7, the nitride membrane will prevent edge damages from prolong wet etching using TMAH. Furthermore, the nitride membrane is less likely to propagate cracks due to crystalline structure.

Charging effects of the collapse-mode CMUT should also be studied as it was not characterized. Charging effect is typically more prominent in collapse-mode since there is direct contact between the membrane and the insulation layer and it is likely to be a concern after prolong operation. This effect may degrade performance as charge can be stored in between the dielectric layer and electrostatic force can decrease.

Another important metric that was not reported in this chapter is yield across batches. Ideally, this process should be repeated vigorously to quantify the batch yield and void to convince researchers and industries to adopt the process. Perhaps to save time, an infrared camera can be used post bonding, but prior to annealing, to determine the voids.

Chapter 8 SUMMARY

The impact of real-time 3-D ultrasound can potentially change the way medical diagnosis work. Having properly reconstructed volume data can allow physicians to diagnose not only faster but more accurately. New treatments, in theory, could be developed using RT3D imaging. For example, surgeries can be performed with concurrent ultrasound imaging to reduce complications such as mistakenly cutting into an underlying blood vessel. Although CT-scans and MRIs have already matured in 3-D scanning in medical imaging, it could be easily argued that ultrasound can achieve 3-D in a much more cost-effective and portable manner. Furthermore, the fast emergence of microfabricated transducer technology is pointing towards a future where ultrasound imaging machines can be an off-the-shelf product that can be accessible by the mass public - perhaps even an attachable product to consumer cellular phones.

With the impressive parallel digital computational technology, processing data and subsequently reconstructing and rendering volumetric scans is made possible and has been demonstrated at fast speed. The frame rate, however, is limited by the sound speed. As sound wave has to travel from and to the transducer, the frame rate can be no faster than the time it takes for sound waves to finish scanning throughout the image sector. For a 2-D scan, real-time frame-rate (>20fps) can be made with commercially available 1-D transducer arrays. For a 3-D scan, however, the speed of sound greatly limits the number of scan lines, which limits the image resolution. Another limitation is that a fully addressed 2-D array with N × N elements, which is capable of steering the sound beam in 3-D, requires N × N electrical addressing lines or wirings. Assuming front-end circuitry can be fabricated small enough with the submicron CMOS technology, the number of electrical leads connecting the front-end circuitry with the processing unit (i.e. FPGA and computer) could easily exceed one thousand. As a result, the system can quickly become very bulky and thus eliminating the portability benefit that makes ultrasound modality so competitive. Perhaps if there is a high density cabling and interconnect technology break through, a fully addressed 2-D array will one day be revisited. Until then, a simplified solution is necessary to drive 2-D arrays for RT3D imaging.

Row-column addressing is a simplification scheme that requires only N + N addressing lines to activate each element in an N × N array. More precisely, it uses two overlaying, orthogonal, and elongated 1-D arrays to perform transmit and receive events separately. As a result, the fabrication, circuit, and processing complexity dramatically decreases. This makes row-column array a very achievable simplification method. Combining the addressing method with microfabrication technology, a compact and high performing 2-D array can be made. The wide bandwidth CMUTs have to offer along with the micro-precision fabrication can complement volumetric imaging very well.

The application-in-mind that steered much of this dissertation work is a finger-probe imaging system. A RT3D imaging system on a finger tip can allow physicians to image with ease during surgeries and RC-CMUT array aligns particularly well with this application. Keep in mind that CMUT technology excels relative to piezoelectric-based probes when the aperture is small and array count is high. It would not make sense to have a CMUT aperture over a few centimetres. Since addressing channel is typically limited to 128 or 256, having large aperture would not benefit from microfabrication. In fact, yield is typically inversely proportional to device area (which is also why cameras with larger CMOS are much more expensive). On the opposite end, a small RC-CMUT would not be too useful given a limited field-of-view (FOV) and FOV-to-resolution ratio. Hence, an RC-CMUT design with an aperture size that can fit on a finger tip would be rather sensible.

In Chapter 4, acoustic field simulation of the one-way beam radiation of the transmit aperture shows that the focused acoustic pulse is a narrow elongated beam in the elevation direction. The importance of this limitation is that the height of this elongated beam governs the FOV. Given the principle of reciprocity, the focusing field of the receive aperture is identical but orthogonal to that of the transmit aperture. Since the two-way, or pulse-echo, spatial response is simply the convolution of the transmit and receive field, the possible spatial field for focusing is limited to what is directly in front of the transducer. As a result, the possible focused scanning space of an RC-array can be perceived as a rectangular prism with the same x- and y-width as the RC-array itself. For a large aperture of several centimetres, this limitation would not be of great importance as linear 1-D arrays share similar problem. For a smaller aperture, however, this could be of great concern. As explained in chapter 4.5, the aperture size scales with the FWHM of the PSF. This means a smaller aperture will yield a lower lateral resolution. Since aperture size is limited by both the application and fabrication yield, another approach to overcome the bottleneck of RC-CMUT arrays is to curve the aperture. In chapter 4.8, the simulated one-way radiation profile is provided along with a B-mode image with wire-targets. This reconstructed image shows that the FOV significantly improved from less than 15 degrees to 73 degrees with a 10-mm radius-of-curvature.

In Chapter 5, the design and pseudo-RT3D scanning results of a customizable RC-CMUT imaging system is presented. This is the first system to demonstrate a real-time scanning with an RC-array. The reported system demonstrates an approximately 5 volume-per-second refresh rate at 41°×41° scan volume with 1800 scan lines. The results demonstrate that the reported platform exhibits great potential in becoming the foundation of a viable and fast 3-D ultrasound imaging system. This system was tested with a 32 × 32 CMUT array with a center frequency of 5.9MHz and a relative bandwidth of 110%. Beamforming simulation and a three-dimensional image of three pin heads were demonstrated.

Commercial medical ultrasound imaging systems cannot drive customized 2-D arrays, including RC-CMUT arrays. There are a few existing commercialized prototyping systems design to drive customized 1-D arrays. Although these systems do offer most of the internal hardware components to drive an RC-array, significant hardware and software design effort is still required to interface with the front-end circuitry and also perform RC beamforming and image reconstruction. Instead, we developed most of the hardware on the PCI eXtensions for Instrumentation (PXI) framework which is a very modularized and standardized lab instrument/platform. PXI systems are common in both academic and industry labs. Furthermore, the software was designed with Labview, which has become a very popular software platform for engineers of all types. Many of the established CMUT groups have collaborated with well-known ultrasound imaging companies such as GE medical or BK medical. As a result, many of the front-end circuitries or system design are either not-reported in detail or use ASICs that are not accessible to researchers. In comparison, the reported front-end circuits were made from very obtainable circuit components. This system may be very suitable for ultrasound labs that are looking for a more budget-friendly and customizable prototyping system.

Chapter 6 presents a novel fabrication method for creating a thin and flexible CMUT array. The array can be mounted on a curved surface to improve FOV. Taking advantage of silicon-on-insulator (SOI)’s buried oxide (BOX) layer, the wet-etch removal of the silicon handling layer naturally provides a uniform thickness and achieve a ~5-μm transducer thickness. A polydimethylsiloxane (PDMS) layer was deposited prior to etching and served as an encapsulation layer and also an etch-resist layer. Several design iterations were carried out and failure modes were discussed. Through vibrometer characterization, the in-air resonant frequency of 12.5MHz is found. Given a 60-V bias and a 15-Vpp AC voltage, the maximum membrane displacement at resonant frequency was measured to be 32 nm. The pull-in voltage was measured to be 72 V. Pitch-catch experiment in vegetable oil revealed a centre frequency of 3.1 MHz, a bandwidth of 63%, and a receive sensitivity of 0.87 V/MPa. After the PDMS film was applied, an increase in centre frequency from 3.1 MHz to 5.7 MHz was found. The received signal amplitude decreased by 80% while the fractional bandwidth increased to 74%. These losses are likely attributed to the acoustic impedance mismatch at the PDMS-oil. After thinning, a decrease in centre frequency from 5.7 MHz to 4.5 MHz was found. The received signal decreased by 60% while the fractional bandwidth increased to 82%. A vibrometer check was done after thinning and a fully functional 8+8 array subset was confirmed. The array was able to be bend and can be placed on a 10-mm radius rod without visual damage. One of the critical concern was the difficulty in electrical interfacing. Wire-bonds, which are commonly used to package MEMS devices were easily damaged during the thinning or handling process. Therefore, a new design is presented with a flip-chip bonding approach to interface the CMUTs. An interfacing flexible circuit is designed specifically to bond with the CMUT.

Chapter 7 presents a fabrication method that addresses some limitation in the standard wafer bonding process used in Chapter 6. The usage of SOI wafers as the top bonding wafer imposes some problems. Edge defects due to etching process combined with the crystalline structure can lead to crack propagation. Using a nitride membrane can resolve these issues since LPCVD nitride is completely resistant against the etching solution and it does not have a directional-dependent, crystalline structure. In addition, the thickness uniformity of SOI wafers is very poor (variation of 33%+). This means the intended resonant frequency can be shifted as much as 1-MHz due to thickness variation. and membrane failures occurs in thin areas. The new fabrication method uses low-pressure chemical vapor deposition (LPCVD) silicon nitride as a membrane layer. Since using a traditional SOI-based wafer bonding process means the breakdown voltage is limited by the thickness of the oxide insulating post, a nitride (non-conductive) membrane will yield a much more robust device. Furthermore, the top silicon plate layer, from the SOI process, in the area between the cells contributes to parasitic capacitance due to the conductivity of the silicon membrane. Although a reported local oxidation of silicon (LOCOS) technique can overcome the two limitations by separating the fixed constraint of gap height and post height, the fabrication complexity and cost of LOCOS process, are considerably higher than conventional wafer bonding process. The reported nitride process only uses 3 masks while the LOCOS-based process uses at least 6 masks. In addition, the LOCOS process uses several high temperature steps to grow and process nitride and oxides where each step would add significant process time. Another noticeable advantage with the reported process is that the cost of using nitride membrane is a fraction of that of an SOI-based membrane.

The surface morphology of LPCVD nitride film was also studied. The AFM scans shows the growth and spread of nanopillars during deposition that accounts for bonding failures in thick (>400-m) nitride films. This discovery can help explain why RMS surface roughness does not clearly reflect the ability to bond. Moreover, if a 5-µm×5-µm AFM scan was done to identify the RMS, one can easily miss the nanopillars, and thus it is important to scan a larger area to identify nanopillars. It is also concluded that CMP is necessary for the removal of these pillars and secure bonding for thicker films.

Functional CMUTs were fabricated using the novel nitride-to-oxide wafer bonding process. To simplify the development of the process, only a 1-D array CMUT was designed and fabricated instead of the 2-D RC-CMUT array. However, the process can be extended to RC-CMUTs. The membrane and cavity structure of the CMUT was designed for collapse-mode operation as an attempt to add more value to future CMUT devices related to this project. Collapse-mode offers higher sensitivity and a wider-bandwidth which result in better contrast and resolution. An impedance measurement was done to verify in-air resonance, which was found to vary significantly based on bias voltage as expected. The membrane collapses at 15-V bias voltage and the corresponding resonance frequency was found to be 8.2 MHz. As the bias voltage increases, the frequency increases as well. This is expected given the reduction in vibrating membrane area. At 45-V bias, the frequency can shift to 14.2 MHz although output pressure stops increasing. This is likely because the average membrane displacement and effective aperture decreases beyond 45-V. Immersion acoustic measurements were conducted via one-way transmit/receive and pulse-echo experiment. Unexpectedly, the transmit and receive centre frequency were very different. In transmit test, the centre frequency was 1.7 MHz with a -

3-dB fractional bandwidth of 122%. In receive, the centre frequency was 4.7 MHz with a 124% -3-dB fractional bandwidth. The 1.7-MHz center frequency matches well with the immersion pre-collapse natural frequency which is unexpected as the CMUT should already be operating in collapse-mode. With the bias voltage increased to 30-V the transmit was still operating in pre-collapse frequency. The discrepancy is likely attributed to electrode misalignment in photolithography. A sectional vibrometer displacement scan of the membranes captured the asymmetry (due to misalignment) of the vibrational area which helps explain the discrepancy. Given a large pulse excitation in transmit mode, the asymmetry reduces the effects of collapse-mode vibration and promotes the first-mode natural vibration of the membrane. Pulse-echo experiment shows excellent sensitivity with a centre frequency of 2.1 MHz and a 100% fractional bandwidth. An A-line test was also done to determine the thickness of an aluminum plate.

References

[3.1] M. I. Haller and B. T. Khuri-Yakub, “A surface micromachined electrostatic ultrasonic air transducer,” in *Ultrasonics Symposium, 1994 IEEE*, 1994, vol. 2, pp. 1241–1244.

[3.2] H. T. Soh, I. Ladabaum, A. Atalar, C. F. Quate, and B. T. Khuri-Yakub, “Silicon micromachined ultrasonic immersion transducers,” *Applied physics letters*, vol. 69, no. 24, pp. 3674–3676, 1996.

[3.3] X. Jin, I. Ladabaum, F. Degertekin, S. Calmes, and B. T. Khuri-Yakub, “Fabrication and characterization of surface micromachined capacitive ultrasonic immersion transducers,” *Journal of Microelectromechanical Systems*, vol. 8, no. 1, pp. 100–114, Mar. 1999.

[3.4] L. E. Kinsler, A. R. Frey, A. B. Coppens, and J. V. Sanders, “Fundamentals of acoustics,” *Fundamentals of Acoustics*, 4th Edition, by Lawrence E. Kinsler, Austin R. Frey, Alan B. Coppens, James V. Sanders, pp. 560. ISBN 0-471-84789-5. Wiley-VCH, December 1999., p. 560, 1999.

[3.5] I. O. Wygant, M. Kupnik, and B. T. Khuri-Yakub, “Analytically calculating membrane displacement and the equivalent circuit model of a circular CMUT cell,” in *2008 IEEE Ultrasonics Symposium*, 2008, pp. 2111–2114.

[3.6] Y. Huang, E. H. eggström, M. H. Badi, B. T. Khuri-Yakub, and others, “Fabricating capacitive micromachined ultrasonic transducers with wafer-bonding technology,” *Microelectromechanical Systems, Journal of*, vol. 12, no. 2, pp. 128–137, 2003.

[3.7] E. Jeanne, C. Meynier, F. Teston, D. Certon, N. Felix, M. Roy, and D. Alquier, “Protection Layer Influence on Capacitive Micromachined Ultrasonic Transducers Performance,” Warrendale, PA, 2008, vol. 1052.

[3.8] D.-S. Lin, X. Zhuang, S. H. Wong, M. Kupnik, and B. T. Khuri-Yakub, “Encapsulation of Capacitive Micromachined Ultrasonic Transducers Using

Viscoelastic Polymer*,"* *J Microelectromech Syst*, vol. 19, no. 6, pp. 1341–1351, Dec. 2010.

[3.9] D. N. Stephens, K. K. Shung, J. Cannata, JianZhong Zhao, R. Chia, H. Nguyen, K. Thomenius, A. Dentinger, D. G. Wildes, Xunchang Chen, M. O'Donnell, R. I. Lowe, J. Pemberton, G. H. Burch, and D. J. Sahn, "Clinical application and technical challenges for intracardiac ultrasound imaging catheter based ICE imaging with EP mapping," *presented at the Ultrasonics Symposium, 2004 IEEE*, 2004, vol. 1, p. 772–777 Vol.1.

[3.10] B. Bayram, M. Kupnik, G. G. Yaralioglu, O. Oralkan, A. S. Ergun, S. H. Wong, and B. T. Khuri-Yakub, "Finite element modeling and experimental characterization of crosstalk in 1-D CMUT arrays," *Ultrasonics, Ferroelectrics and Frequency Control, IEEE Transactions on*, vol. 54, no. 2, pp. 418–430, 2007.

[3.11] E. Campbell, L. A. J. Davis, G. Hayward, and D. Hutchins, "Cross-Coupling in Sealed cMUT Arrays for Immersion Applications," presented at *the Ultrasonics Symposium, 2007. IEEE*, 2007, pp. 2135–2138.

[3.12] P. Rev, M. Salhi, S. Giroud, P. Robert, C. Lagahe-Blanchard, S. CIatot, and S. Ballandras, "New manufacturing method for capacitive ultrasonic transducers with monocrystalline membrane," *presented* at *the Micro Electro Mechanical Systems, 2007. MEMS. IEEE 20th International Conference on*, 2007, pp. 581–584.

[3.13] Xuefeng Zhuang, Der-Song Lin, O. Oralkan, and B. T. Khuri-Yakub, "Fabrication of Flexible Transducer Arrays With Through-Wafer Electrical Interconnects Based on Trench Refilling With PDMS," *Microelectromechanical Systems, Journal of*, vol. 17, no. 2, pp. 446–452, 2008.

[3.14] C. B. Doody, Xiaoyang Cheng, C. A. Rich, D. F. Lemmerhirt, and R. D. White, "Modeling and Characterization of CMOS-Fabricated Capacitive Micromachined Ultrasound Transducers," *Microelectromechanical Systems, Journal of*, vol. 20, no. 1, pp. 104–118, 2011.

[3.15] X. Zhuang, A. Nikoozadeh, M. A. Beasley, G. G. Yaralioglu, B. T. Khuri-Yakub, and B. L. Pruitt, "Biocompatible coatings for CMUTs in a harsh, aqueous environment," *J. Micromech. Microeng.*, vol. 17, no. 5, pp. 994–1001, May 2007.

[3.16] Stephens, Douglas N, Uyen T Truong, Amin Nikoozadeh, Omer Oralkan, Chi HyungSeo, Jonathan Cannata, Aaron Dentinger, et al, "First in Vivo Use of a Capacitive Micromachined Ultrasound Transducer Array-based Imaging and Ablation Catheter." *Journal of Ultrasound in Medicine: Official Journal of the American Institute of Ultrasound in Medicine* 31 (2012): 247–256.

[3.17] Choe, J.W., O. Oralkan, A. Nikoozadeh, M. Gencel, D.N. Stephens, M. O'Donnell, D.J. Sahn, and B.T. Khuri-Yakub, "Volumetric Real-time Imaging Using a CMUT Ring Array." *IEEE Transactions on Ultrasonics, Ferroelectrics and Frequency Control* 59(2012): 1201 –1211.

[3.18] Degertekin, F. L., R. O. Guldiken, and M. Karaman., "Annular-ring CMUT Arrays for Forward-looking IVUS: Transducer Characterization and Imaging." *IEEE Transactions On Ultrasonics, Ferroelectrics and Frequency Control,* 53(2006): 474–482.

[3.19] Leproux, A., M. Van Beek, U. De Vries, M. Wasser, L. Bakker, O. Cuisenaire, M. Van Der Mark, and R. Entrekin, "Automated 3D Whole-breast Ultrasound Imaging: Results of a Clinical Pilot Study." *In SPIE Medical Imaging,* (2011):762902–762902.

[3.20] Maruotti, G. M., D. Paladini, R. Napolitano, L. L. Mazzarelli, T. Russo, M. Quarantelli, M. R. D'Armiento, and P. Martinelli, "Prenatal 2D and 3D Ultrasound Diagnosis of Diprosopus: Case Report with Post-mortem Magnetic Resonance Images (MRI) and Review of the Literature." *Prenatal Diagnosis*, 29 (2009): 992–994.

[3.21] Natarajan, S., L. S. Marks, D. J. A. Margolis, J. Huang, M. L. Macairan, P. Lieu, and A. Fenster, "Clinical Application of a 3D Ultrasound-guided Prostate Biopsy System." In *Urologic Oncology: Seminars and Original Investigations*, 29(2011):334–342.

[3.22] Lockwood, G. R., and F. S. Foster, "Optimizing Sparse Two-dimensional Transducer Arrays Using an Effective Aperture Approach." *Proceedings In IEEE International Ultrasonics Symposium,* 3(1994):1497–1501.

[3.23] Thomenius, K. E., "Evolution of Ultrasound Beamformers*." Proceedings In International Ultrasonics Symposium*, 2(1996):1615–1622.

[3.24] Huang, Yongli, Edward O Haeggström, Xuefeng Zhuang, Arif S Ergun, and Butrus T Khuri-Yakub, "A Solution to the Charging Problems in Capacitive Micromachined Ultrasonic Transducers." *IEEE Transactions on Ultrasonics, Ferroelectrics, and Frequency Control* 52 (2005): 578–580.

[3.25] Bayram, B., M. Kupnik, G.G. Yaralioglu, O. Oralkan, Dersong Lin, Xuefeng Zhuang, A.S. Ergun, A.F. Sarioglu, S.H. Wong, and B.T. Khuri-Yakub, "Characterization of Cross-coupling in Capacitive Micromachined Ultrasonic Transducers." *In IEEE International Ultrasonics Symposium*, 1(2005):601 – 604. doi:10.1109/ULTSYM.2005.1602924.

[3.26] Bayram, B., G.G. Yaralioglu, M. Kupnik, and B.T. Khuri-Yakub. 2006. "5F-4 Acoustic Crosstalk Reduction Method for CMUT Arrays." *Proceedings In International IEEE Ultrasonics Symposium*, (2006) 590 –593.

[4.1] C. E. Morton and G. R. Lockwood, "Theoretical assessment of a crossed electrode 2-D array for 3-D imaging," in *Ultrasonics, IEEE Symposium* on, 2003, vol. 1, pp. 968 – 971 Vol.1.

[4.2] N. M. Daher and J. T. Yen, "Rectilinear 3-D ultrasound imaging using synthetic aperture techniques," in *IEEE Ultrasonics Symposium*, 2004, vol. 2, pp. 1270–1273 Vol.2.

[4.3] N. M. Daher and J. T. Yen, "2-D array for 3-D ultrasound imaging using synthetic aperture techniques," *Ultrasonics, Ferroelectrics and Frequency Control, IEEE Transactions on*, vol. 53, no. 5, pp. 912 –924, May 2006.

[4.4] A. S. Logan, L. L. Wong, and J. T. Yeow, "2-D CMUT wafer bonded imaging arrays with a row-column addressing scheme," *in 2009 IEEE International Ultrasonics Symposium*, 2009, pp. 984–987.

[4.5] S. I. Awad and J. T. Yen, "3-D Spatial Compounding Using a Row-Column Array," *Ultrason Imaging*, vol. 31, no. 2, pp. 120–130, Jan. 2009.

[4.6] C. H. Seo and J. T. Yen, "A 256 x 256 2-D array transducer with row-column addressing for 3-D rectilinear imaging," *Ultrasonics, Ferroelectrics and Frequency Control, IEEE Transactions on*, vol. 56, no. 4, pp. 837 –847, Apr. 2009.

[4.7] C. E. M. Demore, A. Joyce, K. Wall, and G. Lockwood, "Real-time volume imaging using a crossed electrode array," *Ultrasonics, Ferroelectrics and Frequency Control, IEEE Transactions on,* vol. 56, no. 6, pp. 1252 –1261, Jun. 2009.

[4.8] R. J. Zemp, W. Zheng, and P. Zhang, "Feasibility of Top-Orthogonal-to-Bottom Electrode (TOBE) 2D CMUT arrays for low-channel-count 3D imaging*," in 2011 IEEE International Ultrasonics Symposium*, 2011, pp. 498–502.

[4.9] A. S. Logan, L. L. P. Wong, A. I. H. Chen, and J. T. W. Yeow, "A 32 x 32 element row-column addressed capacitive micromachined ultrasonic transducer," *Ultrasonics, Ferroelectrics and Frequency Control, IEEE Transactions on,* vol. 58, no. 6, pp. 1266 –1271, Jun. 2011.

[4.10] R. J. Zemp, R. Chee, A. Sampaleanu, D. Rishi, and A. Forbrich, "S-sequence bias-encoded photoacoustic imaging with top Orthogonal to Bottom Electrode (TOBE) CMUT arrays," *in 2013 IEEE International Ultrasonics Symposium (IUS),* 2013, pp. 1197–1200.

[4.11] T. L. Christiansen, C. Dahl-Petersen, J. A. Jensen, and E. V. Thomsen, "2-D row-column CMUT arrays with an open-grid support structure," 2013, pp. 1712–1715.

[4.12] A. Sampaleanu, P. Zhang, A. Kshirsagar, W. Moussa, and R. J. Zemp, "Top-orthogonal-to-bottom-electrode (TOBE) CMUT arrays for 3-D ultrasound imaging," *IEEE transactions on ultrasonics, ferroelectrics, and frequency control*, vol. 61, no. 2, pp. 266–276, 2014.

[4.13] R. K. W. Chee, A. Sampaleanu, D. Rishi, and R. J. Zemp, "Top orthogonal to bottom electrode (TOBE) 2-D CMUT arrays for 3-D photoacoustic imaging," *IEEE Transactions on Ultrasonics, Ferroelectrics, and Frequency Control*, vol. 61, no. 8, pp. 1393–1395, Aug. 2014.

[4.14] T. L. Christiansen, M. F. Rasmussen, J. A. Jensen, and E. V. Thomsen, "Row-column addressed 2-D CMUT arrays with integrated apodization,", *in 2014 IEEE International Ultrasonics Symposium,* 2014, pp. 600–603.

[4.15] L. L. P. Wong, A. I. H. Chen, Z. Li, A. S. Logan, and J. T. W. Yeow, "A row-column addressed micromachined ultrasonic transducer array for surface scanning applications," *Ultrasonics,* vol. 54, no. 8, pp. 2072–2080, Dec. 2014.

[4.16] I. Ben Daya, A. I. H. Chen, M. J. Shafiee, A. Wong, and J. T. W. Yeow, "Compensated Row-Column Ultrasound Imaging System Using Fisher Tippett Multilayered Conditional Random Field Model," *PLoS ONE*, vol. 10, no. 12, p. e0142817, 2015.

[4.17] T. L. Christiansen, M. F. Rasmussen, J. P. Bagge, L. N. Moesner, J. A. Jensen, and E. V. Thomsen, "3-D imaging using row–column-addressed arrays with integrated apodization— part ii: transducer fabrication and experimental results," *IEEE Transactions on Ultrasonics, Ferroelectrics, and Frequency Control*, vol. 62, no. 5, pp. 959–971, May 2015.

[4.18] M. F. Rasmussen, T. L. Christiansen, E. V. Thomsen, and J. A. Jensen, "3-D imaging using row-column-addressed arrays with integrated apodization - part i: apodization design and line element beamforming," *IEEE Transactions on Ultrasonics, Ferroelectrics, and Frequency Control*, vol. 62, no. 5, pp. 947–958, May 2015.

[4.19] H. Bouzari, M. Engholm, T. L. Christiansen, M. B. Stuart, S. I. Nikolov, E. V. Thomsen, and J. A. Jensen, "Volumetric ultrasound imaging with row-column addressed 2-D arrays using Spatial Matched Filter beamforming," 2015, pp. 1–4.

[4.20] M. Engholm, T. L. Christiansen, C. Beers, J. P. Bagge, L. N. Moesner, H. Bouzari, A. Lei, M. Berkheimer, M. B. Stuart, J. A. Jensen, and E. V. Thomsen, "A hand-held row-column addressed CMUT probe with integrated electronics for volumetric imaging," *in 2015 IEEE International Ultrasonics Symposium* 2015, pp. 1–4.

[4.21] T. L. Christiansen, J. A. Jensen, and E. V. Thomsen, "Acoustical cross-talk in row–column addressed 2-D transducer arrays for ultrasound imaging," *Ultrasonics*, vol. 63, pp. 174–178, Dec. 2015.

[4.22] H. Bouzari, M. Engholm, T. L. Christiansen, C. Beers, A. Lei, M. B. Stuart, S. I. Nikolov, E. V. Thomsen, and J. A. Jensen, "Volumetric synthetic aperture imaging with a piezoelectric 2D row-column probe," in *SPIE Medical Imaging*, 2016, p. 97900Y–97900Y.

[5.1] M. I. Haller and B. T. Khuri-Yakub, "A surface micromachined electrostatic ultrasonic air transducer", *Ultrasonics Symposium*, pp.1241 -1244 1994

[5.2] Caronti , G. Caliano , R. Carotenuto , A. Savoia , M. Pappalardo , E. Cianci and V. Foglietti "Capacitive micromachined ultrasonic transducer (CMUT) arrays for medical imaging", *Microelectron. J.*, vol. 37, no. 8, pp.770 -777 2006

[5.3] D. N. Stephens, U. T. Truong, A. Nikoozadeh, O. Oralkan, C. H. Seo, J. Cannata, A. Dentinger, K. Thomenius, A. de la Rama, T. Nguyen, F. Lin, B. T. Khuri-Yakub, A. Mahajan, K. Shivkumar, M. O'Donnell, and D. J. Sahn "First in vivo use of a capacitive micromachined ultrasound transducer array-based imaging and ablation catheter", *J. Ultrasound Med.*, vol. 31, no. 2, pp. 247-256, 2013

[5.4] I. Wygant , X. Zhuang , D. Yeh , O. Oralkan , A. Ergun , M. Karaman and B. Khuri-Yakub "Integration of 2D CMUT arrays with front-end electronics for volumetric ultrasound imaging", *IEEE Trans. Ultrason., Ferroelectr., Freq. Control*, vol. 55, no. 2, pp.327 -342 2008

[5.5] J. Zahorian , M. Hochman , T. Xu , S. Satir , G. Gurun , M. Karaman and F. Degertekin "Monolithic CMUT-on-CMOS integration for intravascular ultrasound applications", *IEEE Trans. Ultrason., Ferroelectr., Freq.Control*, vol. 58, no. 12, pp.2659 -2667 2011

[5.6] A. Nikoozadeh , Ö. Oralkan , M. Gencel , J. W. Choe , D. N. Stephens , A. de la Rama , P. Chen , K. Thomenius , A. Dentinger , D. Wildes , K. Shivkumar , A. Mahajan , M. O'Donnell , D. Sahn and P. T. Khuri-Yakub "Forward-looking volumetric intracardiac imaging using a fully integrated CMUT ring array", *IEEE Ultrason. Symp.*, pp.511 -514 2009

[5.7] M. Karaman, I. O. Wygant, Ö. Oralkan, and B. T. Khuri-Yakub, "Minimally redundant 2-D array designs for 3-D medical ultrasound imaging ," *Medical Imaging, IEEE Transactions on* , vol. 28, no. 7, pp. 1051-1061, Jul. 2009.

[5.8] A. Bhuyan, J.W. Choe, C. L. Byung, I. Wygant, A. Nikoozadeh, O. Oralkan, B. T. Khuri-Yakub, "3D volumetric ultrasound imaging with a 32×32 CMUT array integrated with front-end ICs using flip-chip bonding technology," *Solid-State Circuits Conference Digest of Technical Papers (ISSCC) IEEE International,* pp. 396-397 2013.

[5.9] D.-S Lin, R. Wodnicki, X. Zhang, C. Woychik, K. E. Thomenius, R. A. Fisher, D. M. Mills, A. J. Byun, W. Burdick, P. Khuri-Yakub, B. Bonitz, T. Davies, G. Thomas, B.

Otto, M. Topper, T. Fritzsch, and O. Ehrmann, "Packaging and Modular Assembly of Large-Area and Fine-Pitch 2-D Ultrasonic Transducer Arrays," *Ultrasonics, Ferroelectrics and Frequency Control, IEEE Transactions on*, vol. 60, no. 7, pp. 1356-1375, Jul. 2013.

[5.10] S. Vaithilingam , T.-J. Ma , Y. Furukawa , I. O. Wygant , Z. Xuefeng , A. De La Zerda , O. Oralkan , A. Kamaya , S. S. Gambhir , R. B. Jeffrey and B. T. Khuri-Yakub "Three-dimensional photoacoustic imaging using a two-dimensional CMUT array", *IEEE Trans. Ultrason. Ferroelectr. Freq. Control*, vol. 56, no. 11, pp.2411 -2419 2009

[5.11] T. J. Ma, S. R. Kothapalli, S. Vaithilingam, O. Oralkan, A. Kamaya, I. O. Wygant, X. Zhuang, S. S. Gambhir, R. B. Jeffrey, B. T. Khuri-Yakub, "3-D Deep Penetration photoacoustic imaging with a 2-D CMUT array", *Ultrasound Symposium*, pp. 375-377 2010

[5.12] R. Wodnicki, K. Thomenius, F. M. Hooi, S. P. Sinha, P. L. Carson, D. S. Lin, X. Zhuang, B. T. Khuri-Yakub, C. Woychik, "Large area MEMS based ultrasound device for cancer detection", *Nuclear Instruments and Methods in Physics Research*, vol. 648, pp. 135-138 2011

[5.13] D. Mills, "Medical imaging with capacitive micromachined ultrasound transducer (CMUT) arrays"), *Ultraonics Symposium*, pp. 384-390 2004

[5.14] K. E. Thomenius "Evolution of ultrasound beamformers", *Proc. IEEE Ultrason. Symp.*, pp.1615 -1622 1996.

[5.15] C. R. Hazard and G. R. Lockwood, "Real-time synthetic aperture beamforming: practical issues for hardware implementation," *in Proc. IEEE Ultrason. Symp.*, pp.1513 -1516 vol.2. 2001

[5.16] J. T. Yen and S. W. Smith, "Real-time rectilinear volumetric imaging," *Ultrasonics, Ferroelectrics and Frequency Control, IEEE Transactions on*, vol. 49, no. 1, pp. 114 -124, Jan. 2002.

[5.17] M. Inerfield, G. R. Lockwood, and S. L. Garverick, "A sigma-delta-based sparse synthetic aperture beamformer for real-time 3-D ultrasound," *Ultrasonics, Ferroelectrics and Frequency Control, IEEE Transactions on*, vol. 49, no. 2, pp. 243 -254, Feb. 2002.

[5.18] S. Tamano, M. Yamazaki, S. Sano, K. Hara, J. Sakano, and Y. Miwa, "3D ultrasound imaging system using Fresnel ring array," *in Proc. IEEE Ultrason. Symp.*, pp.1310 - 1313 Vol.2. 2003

[5.19] J. T. Yen and S. W. Smith, "Real-time rectilinear 3-D ultrasound using receive mode multiplexing," *Ultrasonics, Ferroelectrics and Frequency Control, IEEE Transactions on*, vol. 51, no. 2, pp. 216 -226, Feb. 2004.

[5.20] A. C. Dhanantwari, S. Stergiopoulos, L. Song, C. Parodi, F. Bertora, P. Pellegretti, and A. Questa, "An efficient 3D beamformer implementation for real-time 4D ultrasound systems deploying planar array probes," in *Proc. IEEE Ultrason. Symp.*, pp.1421 - 1424 Vol.2. 2004

[5.21] C. R. Hazard and G. R. Lockwood, "Theoretical assessment of a synthetic aperture beamformer for real-time 3-D imaging," *Ultrasonics, Ferroelectrics and Frequency Control, IEEE Transactions on*, vol. 46, no. 4, pp. 972 -980, Jul. 1999.

[5.22] D. H. Turnbull, F. S. Foster, "Beam steering with pulsed two-dimensional transducer arrays," *Ultrasonics, Ferroelectrics and Frequency Control*, IEEE Transactions on, vol. 38, no. 4, pp. 320-333, July 1991.

[5.23] D. H. Turnbull, P. K. Lum, A. T. Kerr, F. S. Foster, "Simulation of B-scan images from two-dimensional transducer arrays: Part I - Methods and quantitative contrast measurements," *Ultrasonic Imaging*, vol. 14, pp. 323-343, Oct 1992.

[5.24] R. E. Davidsen, J. A. Jensen, S. W. Smith, "Two-dimensional random arrays for real-time volumetric imaging," Ultrasonic Imaging, vol. 16, pp.143-163, Jul 1994.

[5.25] P. K. Weber, R. M. Schmitt, B. D. Tylkowski, J. Steck, "Optimization of random sparse 2-D transducer arrays for 3-D electronic beam steering and focusing," in *Proc. IEEE Ultrason. Symp.*, pp. 1503-1506. 1994.

[5.26] S. Holm, B. Elgetun, G. Dahl, "Properties of the Beampattern of Wegiht- and Layout-Optimized Sparse Arrays," *Ultrasonics, Ferroelectrics and Frequency Control, IEEE Transactions on*, vol. 44, No. 5, pp. 983-991, September 1997.

[5.27] T. L. Szabo, Diagnostic Ultrasound Imaging: Inside Out. Academic Press, 2004.

[5.28] G. R. Lookwood and F. S. Foster, "Optimizing the radiation pattern of sparse periodic two-dimensional arrays," *Ultrasonics, Ferroelectrics and Frequency* Control, IEEE Transactions on, vol. 43, no. 1, pp. 15 -19, Jan. 1996.

[5.29] G. R. Lockwood, J. R. Talman, and S. S. Brunke, "Real-time 3-D ultrasound imaging using sparse synthetic aperture beamforming," *Ultrasonics, Ferroelectrics and Frequency Control, IEEE Transactions on*, vol. 45, no. 4, pp. 980 -988, Jul. 1998.

[5.30] J. W. Choe, O. Oralkan, and P. T. Khuri-Yakub, "Design optimization for a 2-D sparse transducer array for 3-D ultrasound imaging," in *Proc. IEEE Ultrason. Symp*., pp. 1928 -1931. 2010

[5.31] J. W. Choe, A. Nikoozadeh, O. Oralkan, and B. T. Khuri-Yakub, "GPU-Based Real-Time Volumetric Ultrasound Image Reconstruction for a Ring Array," *Medical Imaging, IEEE Transactions on*, vol 32, no 7, pp 1258-1264, Jul. 2013.

[5.32] A. Bhuyan, J. W. Choie, C. L. Byung, I. Wygant, A. Nikoozadeh, O. Oralkan, B. T. Khuri-Yakub, "3D volumetric ultrasound imaging with a 32×32 CMUT array integrated with front-end ICs using flip-chilp bonding technology", *Solid-State Circuits Conference Digest of Technical Papers (ISSCC), 2013 IEEE International*, pp. 396-397 2013

[5.33] A. S. Logan, L. L. Wong, A. I. H. Chen, and J. T. W. Yeow, "A 32 x 32 element row-column addressed capacitive micromachined ultrasonic transducer," *Ultrasonics, Ferroelectrics and Frequency Control, IEEE Transactions on*, vol. 58, no. 6, pp. 1266 -1271, Jun. 2011.

[5.34] Versonics, Inc. (2016, Sept 8). Key System Specifications of the Vantage Platforms [Online]. Available: http://verasonics.com/vantage-systems/

[5.35] J. M. Yang, K. Maslov, H. C. Yang, Q. Zhou, K. K. Shung, L. V. Wang, "Photoacoustic endoscopy", *Optics Letters*, vol. 34, no. 10, pp. 1591-1593, 2009

[5.36] K. Ohbayashi, D. Choi, H. Hiro-oka, A. Kubota, T. Ohno, R. Ikeda, K. Shimizu, "Ultra-high speed real-time 4D display system installed in ultra-high speed parallel OCT system at a volume rate of 12 volumes/sec", *SPIE Proceedings*, vol 7889, Feb. 2011

[5.37] H. Hiro-oka, D. Choi, K. Shimizu, K. Ohbayashi, "Detailed software design of an ultra-parallel ultra-high speed SD-OCT for real-time 4D display at 12 volume/second ", *SPIE Proceedings*, vol 8213, Feb. 2012

[5.38] C. E. Morton and G. R. Lockwood, “Theoretical assessment of a crossed electrode 2-D array for 3-D imaging,” in *Proc. IEEE Ultrason. Symp*., pp. 968 – 971 Vol.1.2003

[5.39] C. H. Seo and J. T. Yen, “A 256 x 256 2-D array transducer with row-column addressing for 3-D rectilinear imaging,” *Ultrasonics, Ferroelectrics and Frequency Control, IEEE Transactions on*, vol. 56, no. 4, pp. 837 –847, Apr. 2009.

[5.40] A. S. Logan, L. L. Wong, and J. T. W. Yeow, “2-D CMUT wafer bonded imaging arrays with a row-column addressing scheme,” in *Proc. IEEE Ultrason. Symp*., pp. 984 –987.2009

[5.41] J. A. Jensen, J. B. Svendsen,“Calculation of pressure fields from arbitrarily shaped, apodized, and excited ultrasound transducers,”*Ultrasonics, Ferroelectrics and Frequency Control, IEEE Transactions on*,vol. 39, no. 6, pp. 262–267, Mar. 1992.

[5.42] A. S. Logan, L. L. Wong, A. I. H. Chen, and J. T. W. Yeow, “A 32 x 32 element row-column addressed capacitive micromachined ultrasonic transducer,” *Ultrasonics, Ferroelectrics and Frequency Control, IEEE Transactions on*, vol. 58, no. 6, pp. 1266 –1271, Jun. 2011.

[5.43] A. I. Chen and M. Pallapa, "LabVIEW FPGA Design for Real-Time 3-D Ultrasound Imaging System," CMC Microsystems, Kingstron, Canada, App. Note. CMC-00200-01899, Feb, 2012

[5.44] L. L. P. Wong, A. I. Chen, A. S. Logan, and J. T. W. Yeow, “An FPGA-based ultrasound imaging system using capacitive micromachined ultrasonic transducers,” *Ultrasonics, Ferroelectrics and Frequency Control, IEEE Transactions on*, vol. 59, no. 7, pp. 1513 –1520, Jul. 2012.

[5.45] A. I. Chen, L. L. Wong, A. S. Logan, J.T.W. Yeow, “A CMUT-based real-time volumetric ultrasound imaging system with row-column addressing,” in *Proc. IEEE Ultrason. Symp*., pp. 1755 –1758.2011

[5.46] A. S. Logan, “The Design, Fabrication and Characterization of Capacitive Micromachined UltrasonicTransducers for Imaging Applications,” Ph.D. dissertation, Dept. Sys. Des. Eng., Univ. of Waterloo, Waterloo, ON, 2010.

[5.47] I. O. Wygant, N. S. Jamal, H. J. Lee, A. Nikoozadeh, O. Oralkan,M. Karaman, and B. T. Khuri-Yakub, “An integrated circuit withtransmit beamforming flip-chip bonded to a 2-D CMUT array for3-D ultrasound imaging,” *IEEE Trans. Ultrason. Ferroelectr. Freq.Control,* vol. 56, no. 10, pp. 2145–2156, 2009.

[5.48] B. Yiu, I. Tsang, and A. Yu, “Real-time GPU-based software beamformer designed for advanced imaging methods research,” in *Proc. IEEE Ultrason. Symp.*, pp. 1920–1923, 2010.

[6.1] G. S. Letterie and W. H. Catherino, “A 7.5-MHz finger-grip ultrasound probe for real-time intraoperative guidance during complex reproductive surgical procedures,” *Am. J. Obstet. Gyneco*l., vol. 187, no. 6, pp. 1588–1590, Dec. 2002.

[6.2] S. S. Corbett, R. W. Schutz, and J. E. Okies, “A finger-worn ultrasound probe for point-of-care applications,” *in 2014 IEEE Healthcare Innovation Conference (HIC)*, pp. 79–82, 2014.

[6.3] C. E. M. Demore, A. W. Joyce, K. Wall and G. R. Lockwood "Real-time volume imaging using a crossed electrode array", *IEEE Trans. Ultrason. Ferroelecir. Freq. Control*, vol. 56, pp.1252-1261, 2009.

[6.4] C. H. Seo and J. T. Yen, “A 256 x 256 2-D array transducer with row-column addressing for 3-D rectilinear imaging,” *IEEE Trans. Ultrason. Ferroelecir. Freq. Control*, vol. 56, no. 4, pp. 837 –847, Apr. 2009.

[6.5] S. Logan, L. L. P. Wong, A.I. H. Chen, J. T. W. Yeow, "A 32x32 element row-column addressed capacitive micromachined ultrasonic transducer", *IEEE Trans. Ultrason. Ferroelecir. Freq. Control*, vol 58, no. 6, pp. 1266-1271, Jun. 2011.

[6.6] L. L. P. Wong, A.I. H. Chen, Z. Li, A. S. Logan, J. T. W. Yeow, “A row–column addressed micromachined ultrasonic transducer array for surface scanning applications” *Ultrasonics*. Vol. 54 no.8 pp. 2072-2080, Dec. 2014.

[6.7] A.I. H. Chen, L. L. P. Wong, J. T. W. Yeow, "A CMUT-based finger-mounted 3D ultrasound probe” *in Proc. IEEE Ultrason. Symp.*, pp. 1603 - 1606. 2014.

[6.8] C. E. Morton and G. R. Lockwood, "Theoretical assessment of a crossed electrode 2-D array for 3-D imaging", *in Proc. IEEE Ultrason. Symp.* , vol. 1, pp.968 -971, 2003.

[6.9] R. K. W. Chee, A. Sampaleanu, D. Rishi, R. J. Zemp, “Top Orthogonal to Bottom Electrode (TOBE) 2-D CMUT Arrays for 3-D Photoacoustic Imaging” *IEEE Trans. Ultrason. Ferroelecir. Freq. Control*, vol. 61, no. 8, pp. 1394–1395, 2014

[6.10] Sampaleanu, P. Zhang, A. Kshirsagar, W. Moussa, R. J. Zemp, "Top-Orthogonal-to-Bottom-Electrode (TOBE) CMUT Arrays for 3-D Ultrasound Imaging, "*IEEE Trans. Ultrason. Ferroelecir. Freq. Control*, vol. 61, no. 2, pp. 266–276, 2014

[6.11] M. F. Rasmussen, T. L. Christiansen, E. V. Thomsen, J. A. Jensen, "3-D Imaging Using Row–Column-Addressed Arrays With Integrated Apodization— Part I: Apodization Design and Line Element Beamforming," *IEEE Transactions on Ultrasonics, Ferroelectrics, and Frequency Control*, vol. 62, no. 5, pp. 947–958, May. 2015.

[6.12] T. L. Christiansen, M. F. Rasmussen, J. P. Bagge, L. N. Moesner, J. A. Jensen, E. V. Thomsen, "3-D Imaging Using Row–Column-Addressed Arrays With Integrated Apodization— Part II: Transducer Fabrication and Experimental Results," *IEEE Transactions on Ultrasonics, Ferroelectrics, and Frequency Control*, vol. 62, no. 5, pp. 959–971, Jan. 2015.

[6.13] M. Engholm, T. L. Christiansen, C. Beers, J. P. Bagge, L. N. Moesner, H. Mourzari, A. Lei, M. Berheimer, M. B. Stuart, J. A. Jensen, E. V. Thomsen, "A hand-held row-column addressed CMUT probe with integrated electronics for volumetric imaging," *in Proc. IEEE Ultrason. Symp.*, 2015, vol. 1, pp. 959-576.

[6.14] M. I. Haller and B. T. Khuri-Yakub, "A surface micromachined electrostatic ultrasonic air transducer," *in Proc. IEEE Ultrason. Symp*., 1994, pp. 1241-1244.

[6.15] D. N. Stephens, U. T. Truong, A. Nikoozadeh, O. Oralkan, C. H. Seo, J. Cannata, A. Dentinger, K. Thomenius, A. de la Rama, T. Nguyen, F. Lin, P. Khuri-Yakub, A. Mahajan, K. Shivkumar, M. O'Donnell, and D. J. Sahn, "First in vivo use of a capacitive micromachined ultrasound transducer array-based imaging and ablation catheter," *J Ultrasound Med*, vol. 31, no. 2, pp. 247–256, Feb. 2012.

[6.16] X. Jin, I. Ladabaum, F. Degertekin, S. Calmes, and B. T. Khuri-Yakub, "Fabrication and characterization of surface micromachined capacitive ultrasonic immersion transducers," *Journal of Microelectromechanical Systems*, vol. 8, no. 1, pp. 100–114, Mar. 1999.

[6.17] Logan and J. T. Yeow, "Fabricating capacitive micromachined ultrasonic transducers with a novel silicon-nitride-based wafer bonding process," *IEEE Trans. Ultrason. Ferroelecir. Freq. Control*, vol. 56, no. 5, pp. 1074–1084, 2009.

[6.18] S. Erguri, Y. Huang, X. Zhuang, Ö. Oralkan, G. G. Yarahoglu, and B. T. Khuri-Yakub, "Capacitive micromachined ultrasonic transducers: fabrication technology," *IEEE Trans. Ultrason. Ferroelecir. Freq. Control*, vol. 52, no. 12, pp. 2242–2258, 2005.

[6.19] H. C. Ko, M. P. Stoykovich, J. Song, V. Malyarchuk, W. M. Choi, C.-J. Yu, J. B. Geddes Iii, J. Xiao, S. Wang, Y. Huang, and J. A. Rogers, "A hemispherical electronic eye camera based on compressible silicon optoelectronics," *Nature*, vol. 454, no. 7205, pp. 748–753, Aug. 2008

[6.20] K. A. Wong, S. Panda, and I. Ladabaum, "Curved micromachined ultrasonic transducers," *in Proc. IEEE Ultrason. Symp.*, 2003, vol. 1, pp. 572–576.

[6.21] X. Zhuang, D.-S. Lin, Ö. Oralkan, and B. T. Khuri-Yakub, "Fabrication of flexible transducer arrays with through-wafer electrical interconnects based on trench refilling with PDMS," *Microelectromechanical Systems, Journal of*, vol. 17, no. 2, pp. 446–452, 2008.

[6.22] Caronti, A. Coppa, A. Savoia, C. Longo, P. Gatta, B. Mauti, A. Corbo, B. Calabrese, G. Bollino, A. Paz, and others, "Curvilinear capacitive micromachined ultrasonic transducer (CMUT) array fabricated using a reverse process," *in Proc. IEEE Ultrason. Symp.*, 2008, pp. 2092–2095.

[6.23] Z. Wang, Q.-T. Xue, Y.-Q. Chen, Y. Shu, H. Tian, Y. Yang, D. Xie, J.-W. Luo, and T.-L. Ren, "A Flexible Ultrasound Transducer Array with Micro-Machined Bulk PZT," *Sensors*, vol. 15, no. 2, pp. 2538–2547, 2015.

[6.24] Virginia Semiconductor. Mar. 10, 2008. [Online]. Available: http://www.virginiasemi.com/newprod.cfm

[6.25] D. S. Lin, X. Zhuang, S. H. Wong, M. Kupnik, and B. T. Khuri-Yakub, "Encapsulation of Capacitive Micromachined Ultrasonic Transducers Using Viscoelastic Polymer," *Journal of Microelectromechanical Systems*, vol. 19, no. 6, pp. 1341–1351, Dec. 2010.

[6.26] M. F. la Cour, M. B. Stuart, M. B. Laursen, S. E. Diederichsen, E. V. Thomsen, and J. A. Jensen, "Investigation of PDMS as coating on CMUTs for imaging," *in Proc. IEEE Ultrason. Symp.*, 2014, pp. 2584–2587.

[6.27] E. P. Popov, “Moment-curvature Relation,” in *Engineering Mechanics of Solids*, 2nd ed. New Jersey: Prentice Hall, 1991, ch. 14, sec. 2, pp. 583-585.

[6.28] D. Armani, C. Liu, and N. Aluru, “Re-configurable fluid circuits by PDMS elastomer micromachining,” *in Twelfth IEEE International Conference on Micro Electro Mechanical Systems*, 1999, pp. 222–227.

[6.29] T. Ye, Z. Suo, A. G. Evans, “Thin Film Cracking and the Roles of Substrate and Interface,” Int. J. Solids Structures, Vol. 29, No. 21, pp. 2639-25648, 1992.

[6.30] P. Zhang, G. Fitzpatrick, T. Harrison, W. A. Moussa, and R. J. Zemp, “Double-SOI Wafer-Bonded CMUTs With Improved Electrical Safety and Minimal Roughness of Dielectric and Electrode Surfaces,” *Journal of Microelectromechanical Systems*, vol. 21, no. 3, pp. 668–680, Jun. 2012.

[7.1] W. H. Ko, J. T. Suminto, and G. J. Yeh, “Bonding techniques for microsensors,” in *Micromachining and Micropackaging of Transducers*, C. D. Fung, P. W. Cheung, W. H. Ko, and D. G. Fleming, Eds. Amsterdam: The Netherlands: Elsevier, 1985, p. 41.

[7.2] A. Hanneborg, “Silicon wafer bonding techniques for assembly of micromechanical elements,” in *Proc. MEMS Workshop*, Nara, Japan, 1991, p. 92.

[7.3] F. S. D’Aragona and L. Ristic, "Silicon direct wafer bonding" in *Sensor Technology and Devices*, 1994, pp.157-201..

[7.4] K. K. Park, H. J. Lee, M. Kupnik, O. Oralkan and B. T. Khuri-Yakub, "Fabricating capacitive micromachined ultrasonic transducers with direct wafer-bonding and LOCOS technology," in *MEMS 2008. IEEE 21st International Conference on*, Wuhan, 2008, pp. 339-342.

[7.5] J. E. Gragg, W. E. McCulley, W. B. Newton, and C. E. Derrington, “Compensation and calibration of a monolithic four terminal silicon pressure transducer,” in *Tech. Dig. IEEE Solid-State Sensor Workshop*, Hilton Head, SC, June 1984, pp. 21–27.

[7.6] J. B. Lasky, S. R. Stiffler, F. R. White and J. R. Abernathey, "Silicon-on-insulator (SOI) by bonding and ETCH-back," Electron Devices Meeting, 1985 International, 1985, pp. 684-687.

[7.7] Lasky, "Wafer bonding for silicon-on-insulator technologies", *Appl. Phys. Lett.*, vol. 48, no. 1, p. 78, 1986.

[7.8] M. Shimbo, K. Furukawa, K. Fukuda and K. Tanzawa, "Silicon-to-silicon direct bonding method", *J. Appl. Phys*., vol. 60, no. 8, p. 2987, 1986.

[7.9] J. Haisma, G. A. C. M. Spierings, U. K. P. Biermann, and J. A. Pals, “Silicon-on-insulator wafer bonding-wafer thinning technological evaluations,” Jpn. J. Appl. Phys., vol. 28, no. 8, p. 1426, Aug. 1989.

[7.10] M. A. Schmidt, “Wafer-to-wafer bonding for microstructure formation,” *Proceedings of the IEEE*, vol. 86, no. 8, pp. 1575–1585, 1998.

[7.11] Y. Huang, A. S. Ergun, E. Haeggstrom, M. H. Badi, and B. T. Khuri-Yakub, “Fabricating capacitive micromachined ultrasonic transducers with wafer-bonding technology,” *Journal of Microelectromechanical Systems,* vol. 12, no. 2, pp. 128–137, Apr. 2003.

[7.12] M.I. Haller et al., "Micromachined 1-3 Composites for Ultrasonic Air Transducers", *Rev. Sci. Instrum*., vol.65, p.2095-2098, 1994.

[7.13] N. Tas et al., “Stiction in Surface Micromachining”, *J. Micromech. Microeng*., vol. 6, pp. 385–397, 1996.

[7.14] A. Logan and J. T. W. Yeow, "Fabricating capacitive micromachined ultrasonic transducers with a novel silicon-nitride-Based wafer bonding process," *in IEEE Transactions on Ultrasonics, Ferroelectrics, and Frequency Control*, vol. 56, no. 5, pp. 1074-1084, May 2009.

[7.15] A. S. Logan, “The Design, Fabrication and Characterization of Capacitive Micromachined Ultrasonic Transducers for Imaging Applications,” 2010.

[7.16] R. Rhoades, "The Dark Art of CMP", Future Fab International, no. 24, 2007.K. K. Park, H. Lee, M. Kupnik, and B. T. Khuri-Yakub, "Fabrication of capacitive micromachined ultrasonic transducers via local oxidation and direct wafer bonding," *Microelectromechanical Systems, Journal of,* vol. 20, no. 2, pp. 95-103, Feb. 2011.

[7.17] A. Usenko and J. Senawiratne, “Silicon Nitride Surface Conversion into Oxide to Enable Hydrophilic Bonding,” *ECS Transactions*, 2010, pp. 475–483.

[7.18] A. S. Logan, L. L. P. Wong, A.I. H. Chen, J. T. W. Yeow, "A 32x32 element row-column addressed capacitive micromachined ultrasonic transducer", *IEEE Trans. Ultrason. Ferroelecir. Freq. Control*, vol 58, no. 6, pp. 1266-1271, Jun. 2011.

[7.19] M.-C. Ho, M. Kupnik, S. Vaithilingam, and B. T. Khuri-Yakub1, "Fabrication and model validation for CMUTs operated in permanent contact mode," *presented at the IEEE Ultrasonics Symposium*, Orlando, FL, Oct. 18-21, 2011.

[7.20] A. Sampaleanu, P. Zhang, A. Kshirsagar, W. Moussa, R. J. Zemp, "Top-Orthogonal-to-Bottom-Electrode (TOBE) CMUT Arrays for 3-D Ultrasound Imaging, "*IEEE Trans. Ultrason. Ferroelecir. Freq. Control*, vol. 61, no. 2, pp. 266-276, 2014

[7.21] T. L. Christiansen, M. F. Rasmussen, J. P. Bagge, L. N. Moesner, J. A. Jensen, E. V. Thomsen, "3-D Imaging Using Row-Column-Addressed Arrays With Integrated Apodization- Part II: Transducer Fabrication and Experimental Results," *IEEE Transactions on Ultrasonics, Ferroelectrics, and Frequency Control*, vol. 62, no. 5, pp. 959-971, Jan. 2015.

[7.22] P. Zhang, G. Fitzpatrick, T. Harrison, W. A. Moussa, and R. J. Zemp, "Double-SOI Wafer-Bonded CMUTs With Improved Electrical Safety and Minimal Roughness of Dielectric and Electrode Surfaces," *Journal of Microelectromechanical Systems*, vol. 21, no. 3, pp. 668-680, Jun. 2012.

[7.23] Y. Huang, E.O. Haggstrom, X. Zhuang, A.S. Ergun, and B.T. Khuri-Yakub, "Capacitive micromachined ultrasonic transducers (cMUTs) with piston-shaped membranes," *in Proc. IEEE Ultrason. Symp*., Rotterdam, Netherlands, vol.1, pp. 589-592, Sept. 2005.

[7.24] X. Zhuang, A.S. Ergun, O. Oralkan, Y. Huang, I.O. Wygant, G.G. Yaralioglu, D.T. Yeh, and B.T. Khuri-Yakub, "Through-wafer trench-isolated electrical interconnects for cMUT arrays," *in Proc. IEEE Ultrason. Symp.*, Rotterdam, Netherlands, vol.1, no.pp. 475- 478, 18-21 Sept. 2005.

[7.25] A. I. H. Chen, L. L. P. Wong, S. Na, Z. Li, M. Macecek, and J. T. W. Yeow, “Fabrication of a Curved Row-Column Addressed Capacitive Micromachined Ultrasonic Transducer Array,” *Journal of Microelectromechanical Systems*, vol. PP, no. 99, pp. 1–8, 2016.

[7.26] H. Setyawan, M. Shimada, Y. Imajo, Y. Hayashi, and K. Okuyama, “Characterization of particle contamination in process steps during plasma-enhanced chemical vapor deposition operation,” *Journal of Aerosol Science*, vol. 34, no. 7, pp. 923–936, Jul. 2003.

[7.27] M. Shimada, K. Okuyama, Y. Hayashi, H. Setyawan, and N. Kashihara, “Visualization and Control of Particulate Contamination Phenomena in a Plasma Enhanced CVD Reactor,” 2004.

[7.28] W. P. Maszara, “Silicon-On-Insulator by Wafer Bonding: A Review,” *Journal of the Electrochemical Society*, vol. 138, no. 1, pp. 341–347, 1991.

[7.29] K. Reck, E. V. Thomsen, O. Hansen, and others, “Fusion bonding of silicon nitride surfaces,” *Journal of Micromechanics and Microengineering*, vol. 21, no. 12, p. 125015, 2011.

[7.30] M. S. Ismail, R. W. Bower, J. L. Veteran and O. J. Marsh, "Silicon nitride direct bonding," in *Electronics Letters*, vol. 26, no. 14, pp. 1045-1046, 5 July 1990.

[7.31] T. L. Christiansen, O. Hansen, M. D. Johnsen, J. N. Lohse, J. A. Jensen, and E. V. Thomsen, “Void-free direct bonding of CMUT arrays with single crystalline plates and pull-in insulation,” *in 2013 IEEE International Ultrasonics Symposium (IUS)*, 2013, pp. 1737–1740.

[7.32] Aml.co.uk. (2016). AML :: Technologies2. [online] Available at: http://www.aml.co.uk/index.php/technologies2/ [Accessed 27 Jul. 2016].

[7.33] de Larios, "CMP cleaning", in *Chemical-Mechanical Planarization of Semiconductor Materials*, 1st ed., M. Oliver, Ed. Springer Berlin Heidelberg, 2004, pp. pp 251-281.

Appendix A Detail Design and Implementation of PXI-based Imaging System

This section describes the detailed design and implementation of a LabVIEW field programmable gate array (FPGA) for a MEMS-based ultrasound imaging system. The LabVIEW FPGA target is a National Instrument (NI) FlexRIO FPGA module (NI 7954) with a digitizer adapter (NI 5752), installed in a PXI chassis.

LabVIEW Project Setup

Equipment Required

- LabVIEW 9.0 with an FPGA module

1. To ensure the correct setup of the targets and the devices in the project, in the Labview window Project Explorer (as in Figure 16), right click **My Computer**.

2. From the drop-down menu, select **New | Targets and Devices | Existing target or device** (Discover an existing target(s) or device(s)) **| FPGA Target | FlexRIO | RIO1 (PXI-7954R)**.

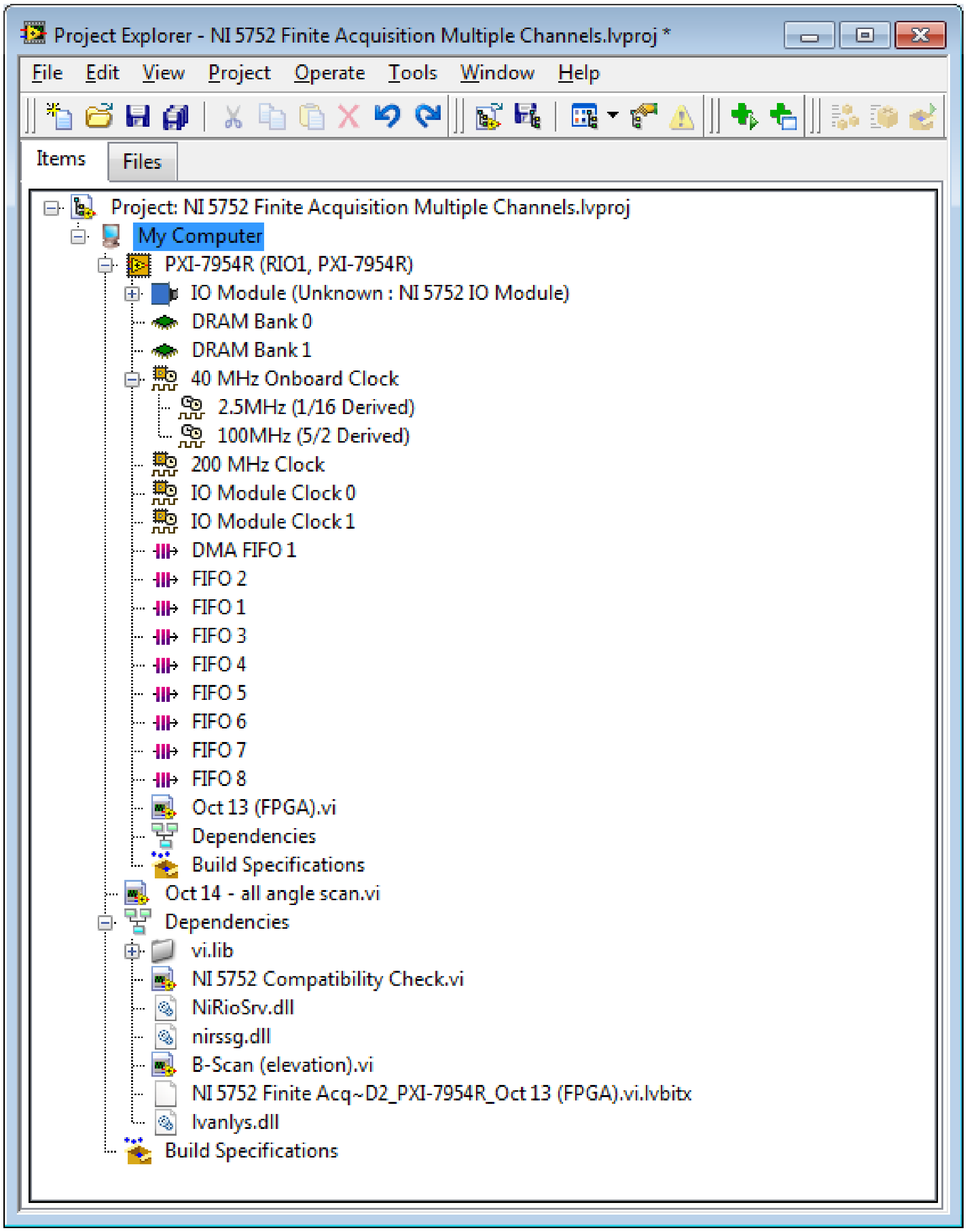

- Project: NI 5752 Finite Acquisition Multiple Channels.lvproj
  - My Computer
    - PXI-7954R (RIO1, PXI-7954R)
      - IO Module (Unknown : NI 5752 IO Module)
      - DRAM Bank 0
      - DRAM Bank 1
      - 40 MHz Onboard Clock
        - 2.5MHz (1/16 Derived)
        - 100MHz (5/2 Derived)
      - 200 MHz Clock
      - IO Module Clock 0
      - IO Module Clock 1
      - DMA FIFO 1
      - FIFO 2
      - FIFO 1
      - FIFO 3
      - FIFO 4
      - FIFO 5
      - FIFO 6
      - FIFO 7
      - FIFO 8
      - Oct 13 (FPGA).vi
      - Dependencies
      - Build Specifications
    - Oct 14 - all angle scan.vi
    - Dependencies
      - vi.lib
      - NI 5752 Compatibility Check.vi
      - NiRioSrv.dll
      - nirssg.dll
      - B-Scan (elevation).vi
      - NI 5752 Finite Acq~D2_PXI-7954R_Oct 13 (FPGA).vi.lvbitx
      - lvanlys.dll
    - Build Specifications

Figure 16: LabVIEW Project Explorer Window

3. Once the target has been added, ensure the resource name is addressed correctly:
   – To change the resource name, right click the FPGA Target, which is **PXI-7954R** in Figure 16**.**

4. To set up clocks and choose the proper IO module clock, follow these steps:

   Note: The FlexRIO module comes with a 40-MHz onboard clock. For this project, a 100-MHz clock is needed and is derived from the 40-MHz onboard clock.

   a. From the window Project Explorer, under the FPGA Target **PXI-7954R**, right click **40 MHz Onboard Clock**.

b. From the drop-down menu, select **New FPGA Derived**.

c. Change the desired derived frequency to 100 MHz and name it **100 MHz clock**, as shown in Figure 16.

Note: The project requires an additional clock that is dedicated to the digitizer module (NI 5752). As long as an analog-to-digital converter is used, an IO Module clock must be used.

5. Under the target clock, verify that **IO Module Clock 0** and **IO Module Clock 1** are present as shown in Figure 16. They are inherently clocked at 50 MHz and 150 MHz respectively.

6. To create the target FPGA file, follow these steps:

   Note: The VI for the FPGA must be created within the Target FPGA tree.

   a. To create the FPGA VI, right click **PXI-7954R (RIO1, PXI-7954R)**.

   b. From the drop-down menu, select **New | VI**.

      Note: The resource name for this example project is **RIO1**.

   c. Name the VI in the format of [**Target(FPGA).vi**]. For example, in Figure 16, it is named **Oct 13 (FPGA).vi**.

      Tip: It is a good practice to add the word **FPGA** in the name so that the user does not confuse the target file with the host file.

7. To create the HOST VI, right click **My Computer**.
8. From the drop-down menu, select **New | Host VI**. For example, in Figure 16, the VI is named **Oct 14 - all angle sca.vi**.

Troubleshooting

If the target FPGA device, which is **PXI-7954R** in this application (see Figure 16), does not show up in the window Project Explorer, follow these steps:

1. From **Windows Start Menu**, select **All Programs | National Instruments | Measurement & Automation**.
2. Ensure the drivers are installed properly.

Hardware Setup

There are 16 channels of analog inputs (AI 0-15), 16 channels of digital inputs (DI 0-15), and 15 channels of digital outputs (DO 0-15) used in the design. They are available from the PXI 7954R FPGA card.Target FPGA VI

Breakdown of Target FPGA VI

If you click the file **Oct 13 (FPGA).vi** from the window Project Explorer in Figure 16, you can see that the target file is broken down into the loops as shown in Figure 17, and the FPGA design begins with a two-step sequential loop. The second sequential loop contains two single-cycle-timed loops (SCTLs) with the **Case** structure embedded in each SCTL. The tasks performed in each loop are listed in Table 3 below.

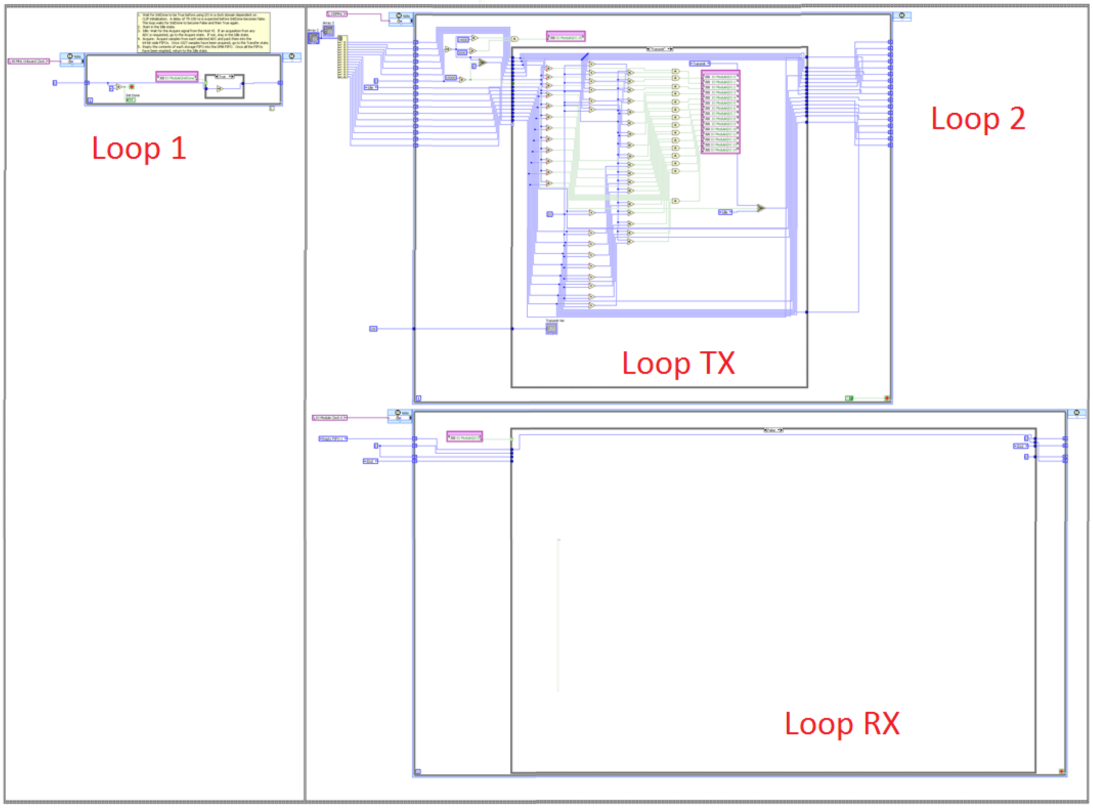

Figure 17: Screen Shot of the Target FPGA File

Table 3: FPGA Task Breakdown

Loop	**Tasks**	**Physical I/O**	**Control / Indicator**
1	Synchronize the I/O Module with the Target FPGA	None	
2-TX	Receive delay instruction; Form transmit phased delay by triggering delayed pulses at different intervals; Signal RX to start when done; Switch to Idle mode.	DI 0~15 DO 0	Delay 1~16
2-RX	Stay Idle until TX finish; Read from ADC and write to FIFO; Write data to the Host file; Return to Idle mode.	DI0 AI 0~15	DMA 1

Loop 1: Synchronizing the I/O Module with Target FPGA

The digitizer NI 5752 can automatically synchronizes with the FPGA (see Figure 18). The synchronizing process may take a while—at least 4 clock cycles as recommended by NI. If the synchronization does not occur, the program exits.

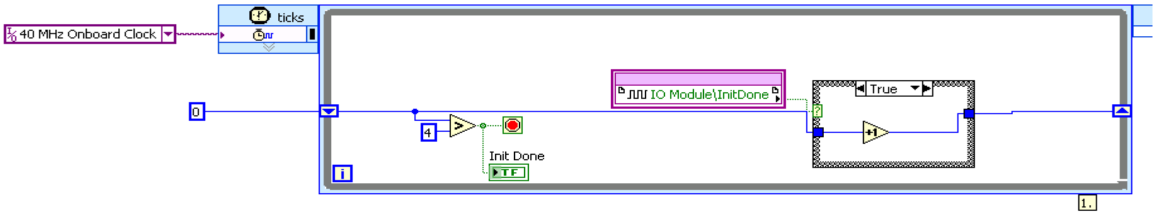

Figure 18: Initializing I/O Module

Loop 2-TX: Transmit Beamforming

The transmit beamforming requires different pulses to be sent at different times, as specified by the Host VI. The loop is set up to have two states—an idle state and a firing state. The transition between states is governed by a counter. The tasks associated with the counter are specified in Table 4.

Table 4: Counter Sequence for the TX Loop

Counter (ticks)	**State Description**
0	Idle: Get the delay instructions (i.e. Delay Number 1, 2,…,15)
1~3,000	Firing: toggle the digital output to **ON** as soon as the corresponding delay number (counter) is reached. The **ON** state only stays for 20 ticks (i.e. 200 ns). There are 15 digital outputs (DO 0~14) assigned for connecting to the external pulsers. This number is limited by the fact that NI 5752 only has 16 digital outputs and at least one is needed for activating the other loop. When 3,000 ticks are reached, DO 15 is triggered to signal that the ADC is ready to be read and recorded.
3,000~14,000	IDLE – DO 15 (Receiving Mode) turns **ON**
14,000~15,000	IDLE – DO 15 is off and nothing happens

During the idle state, the TX-Loop waits for the **Acquire** signal (see Figure 19) to change to **True** before any action. This signal is given by the Host VI (see Figure 20). This communication method where data is sent via controls and indicators is called Programmatic Front Panel Communication. In a later section, another communication method called Direct Memory Access (DMA) will be discussed.

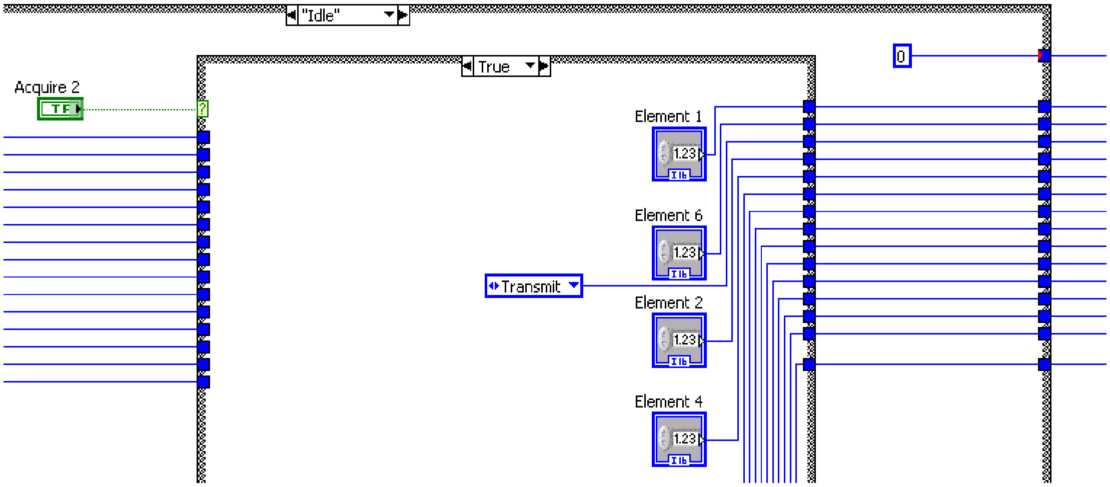

Figure 19: Programmatic Front Panel Communication

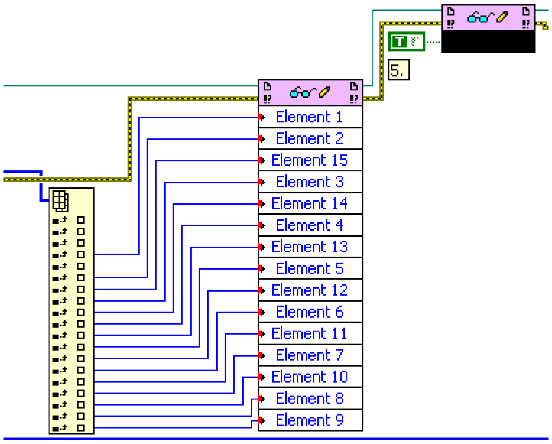

Figure 20: Look-up Table Passing Data to be Written and Sent (from Host PC) to the Target FPGA

Once the **Acquire** signal turns **ON**, the delay sequences start and the **Case** loop switches to **Transmit**. A counter starts incrementing and when it reaches a particular delay value given by the Host PC, it will toggle a digital output to **ON** for 20 ticks. A total of 3,000 ticks is given to ensure sufficient time for all 15 delays to be toggled. Following this sequence is the idle (i.e. RX Loop = TRUE) case. 11,000 ticks are required for the ADC channels to complete the reading (1,000 ticks) and the data to be stored into the DMA FIFO (4,000 ticks).

The remaining ticks are just to ensure the cycle does not loop before the RX mode ends (as given by DI 0). The logic for controlling the timing of these frames is by having a loop counter, which is constructed with a '+1' function, a shift register, and comparators as indicated in Figure 21.

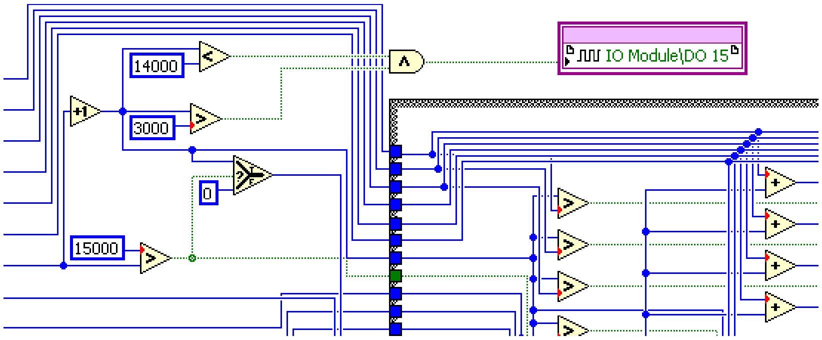

Figure 21: Comparator Logic for Controlling Different States in TX Loop

Loop 2-RX: Recording Echo

After the pulses are fired, the transducer goes in a receiving state where it transduces sound energy to electrical signal. Therefore, the Loop 2-RX is responsible for reading the ADCs on NI 5752 and sending the data to the host PC via DMA FIFOs. The sequence of reading and writing is specified by the counter sequence in Table 5.

Table 5: Counter Sequence for the RX Loop

Counter (ticks)	**State Description**
0 to 300	If DI 0 is on start tick, wait for 300 ticks to occur before starting the ADC. The 300 ticks is a result of a waiting time for the echo to reflect back and be recorded.
300 to 1,300	For every cycle, store each ADC reading data into FIFO (total 1,000 ticks)
1,300 to 5,300	Because there are 4 FIFOs with 1,000 elements each, it will take 4,000 cycles or ticks to append all elements into the DMA FIFO serially.

To use the ADC function of the digitizer, the I/O Module Clock must be used. Hence, Loop RX is a single-cycle-time-loop (SCTL) paired with the I/O Module Clock. If another task requires faster clock speed, that task must have a separate SCTL. Another complication involving I/O-Module-Clock-based SCTL is that there can be no exit condition. Therefore programmers must take this unique condition into consideration when designing the algorithm. To address this issue in the example program, an external switch is programmed with DO 15 and DI 0 to toggle the state in the Loop RX.

FIFOs

Most NI PXI FPGAs offer three DMA channels. For this example, only one DMA channel is sufficient to perform the tasks of transferring data from the FPGA to the host PC. There are 16 ADC channels and the program is designed to acquire 1,000 elements for each channel. This adds up to a total of 16,000 elements. Eventually, these elements or data have to be stored in the DMA FIFO for the host PC to read. A large amount of data means longer writing time. To speed up the transfer, 4 ADC channels are read simultaneously by a single FIFO through the **Join Number** function (See Figure 22) in the **Acquire** State. The user must ensure that the FIFO is configured to be 16 bits with 1,024 elements each and the DMA FIFO has enough bits to store a minimum of 64 bits (16 bits x 4) of data.

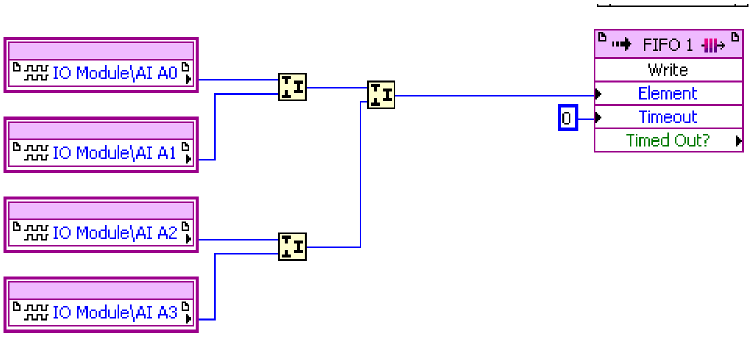

Figure 22: Join Number Function Combining 4 ADC Channels to Speed up Data Transfer

DMA FIFOs

One of the most critical aspects of the host PC to the target FPGA communication is the DMA FIFO. There are two methods to communicate between the host PC and the DMA FIFO, and both are used in this program.

The first method, Programmatic Front Panel Communication, is used to send delay instructions. An example is given in the section Loop 2-TX: Transmit Beamforming.

The second method, Direct Memory Access, is commonly used in FPGA programming when a large amount of data needs to be transferred at a fast rate. In the FPGA, the **DMA FIFO Read** instance is called in the **Transfer Case** (see Figure 23). During the **Transfer Case**, each of the FIFO is read and stored in the DMA FIFO. When all elements of a FIFO are read, the condition **Timed Out ?** returns **True** and the program starts emptying the next FIFO until the last FIFO is read.

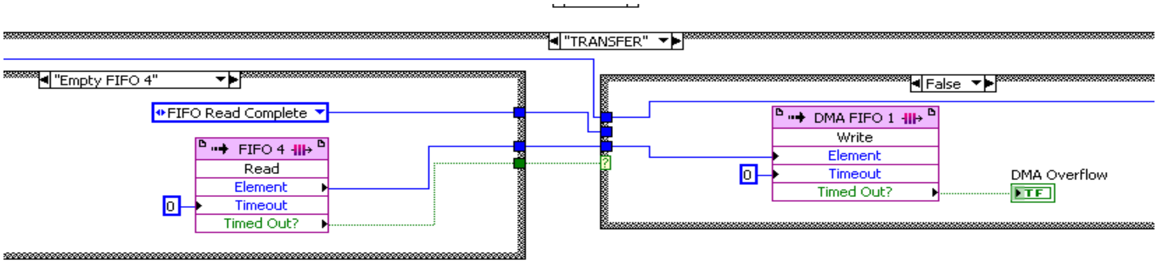

Figure 23: Reading Large Amount of Data from Numerous FIFOs in the FPGA and Writing to Only One DMA FIFO

Host VI

The Host VI contains a **Case** loop with three selections—**Idle**, **Read**, and **Graph**.

In the **Idle** state, a new set of delay instructions are sent to the FPGA followed by a signal instructing the FPGA to start firing pulses and acquiring echo data.

In the **Read** phase, the acquired data from the FPGA is read and stored.

In the **Graph** phase, the echo data read from the FPGA is converted into meaningful 2D sectional scan (B-scan).

Host VI Methodology

The Host VI can be broken down to the following procedures:

1. Check for the compatibility issues between the NI 5752 and NI FlexRIO FPGA modules. (See the most left icon in Figure 24).

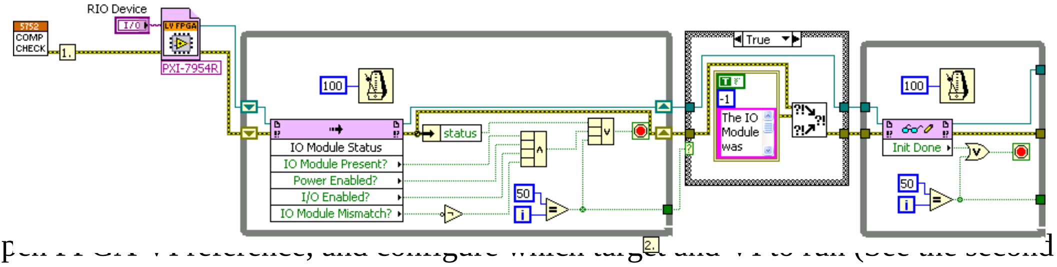

2. Open FPGA VI reference, and configure which target and VI to run (See the second icon in Figure 24). This VI defaults to running on the target.
3. Wait for the IO module to be detected, powered, and enabled before continuing with the program. This code waits for a maximum of 10 seconds before issuing a **Module not Found** error. (See Figure 24).
4. Wait for **CLIP Ready** signal from the target. This means that the module clocks have been synchronized. This code waits for a maximum of 30 seconds before issuing a **CLIP not ready** error. (See Figure 25).

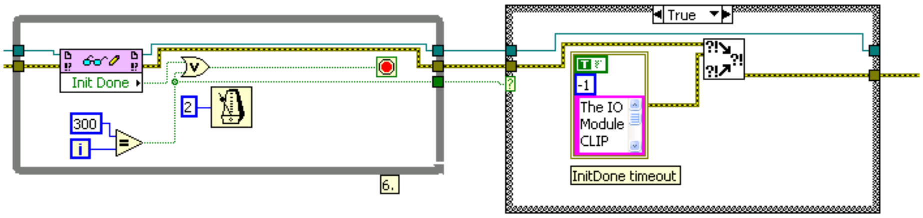

Figure 25: I/O Module Initialization and CLIP Ready Signal

5. Select which set of the delays (based on the angle from -20 to 20) to send to the target FPGA VI and clear graphs from the previous acquisitions. The delay set are stored in an array generated through geometric calculations based on acoustic physics.
6. Signal the FPGA to acquire data (through Programmatic Front Panel Communication).
7. Go to the **Fetch Data** state.
8. DMA the data returned from the FPGA.
9. Go to the **Graph Data** state.
10. The data from the 12-bit ADCs are represented in the CLIP as a 2's compliment, MSB justified, I16. The 4 LSBs are padded with zeros. The data is multiplied by a scaling factor (i.e. ADC voltage resolution = voltage range / ADC intervals x 16) to LSB justify the data and scale to volts.
11. De-interleave and scale the data. (See Figure 26).

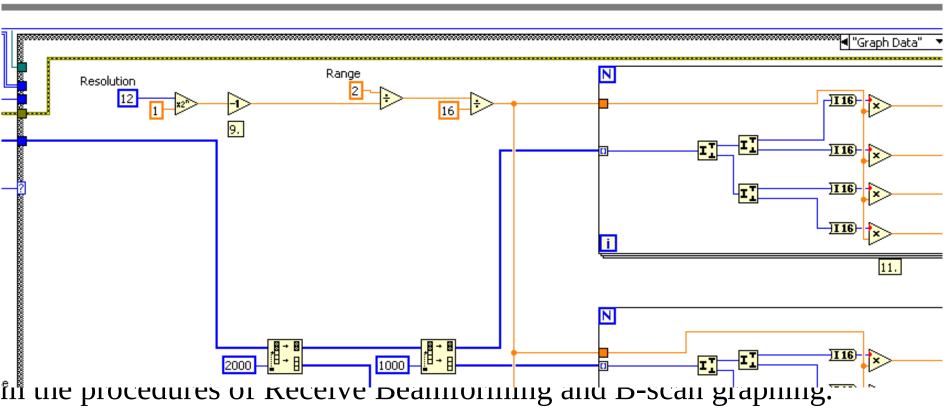

12. Perform the procedures of Receive Beamforming and B-scan graphing.
13. Go to the next delay set (operated in the **Idle** state).
14. Close the FPGA VI reference. This function closes the reference and resets the FPGA.
15. Display any errors encountered.

Reading DMA FIFO

In Figure 27, the **DMA FIFO Read** is called after the Host VI sends the delay instruction. Once called, the **Read** function will wait for maximum 1 ms, as specified by the user, for the reading to complete. In the case where less than 4,000 elements are read within 1 ms, an error message will occur and the program will end. Therefore, it is important for the user to program the Target FPGA VI such that at least 4,000 elements can be ready within a 1-ms timeframe.

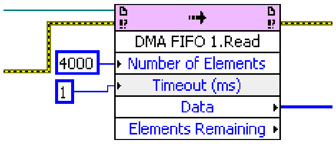

Figure 27: Reading DMA FIFO from the Host PC

Another scenario that needs to be addressed is the partial overwriting/overlapping of the DMA FIFO in the target FPGA VI before it is read properly. For example, if the host file waits for 1 ms before collecting 4,000 elements, but at the same time the FPGA has already finished the TX/RX and is on the second iteration, the host may collect a part of the old data and a part of new data. This can be avoided by adding additional buffer time in the TX/RX loop. In this example, 5,300 ticks at 50 MHz, or 10,600 ticks at 100 MHz is needed for data to be acquired and transferred. However, 12,000 ticks at 100 MHz were dedicated for the RX Loop. The extra 1,400 (=12,000-10,600) ticks are buffering time to avoid overlapping.

Receive Beamforming and Graphing

The 16-channel data with 1,000 elements each forms a waveform that describes the time-of-flight of the pulse-echo. A phased-delay focusing procedure (i.e. receive beamforming) is done by the B-Scan sub-VI. The B-Scan Sub-Vi acts as a converter for transforming these waveforms into 2-D image, where X-Y coordinates along with the associated intensity value is given. Coming out from the B-Scan output, there are 1,353 points to be plotted for 41 different angles each with 300 points in depth. The order of the series is fitted for a polar plot. To convert it into Cartesian for LabVIEW front-panel plotting, a look-up table is constructed that represents the Cartesian equivalent to the plotting coordinates where the B-scan output is ordered. A 3-D scatter plot is created from the X and Y information, see Figure 28.

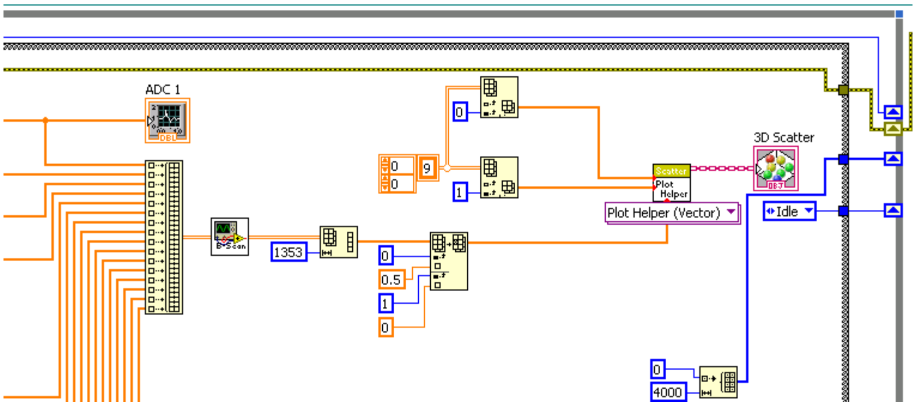

Figure 28: B-Scan Function and 3-D Scatter Plot

Appendix B

Matlab (Field II) code for curved RC-array

```
%all units in m
clear; clc;
%This is a phased array b-mode
%PART 1(a): create curved array for Tx-----------------------------------
----
px = 0.4e-3; %pitch of elements
enum = 32; %number of elements
arcLength = px*enum; %arc length
R = 10e-3; %Radius of Curvature
circum = 2*pi*R; %circumference
sec = (arcLength/circum)*2*pi; %total array sector angle
dtheta = sec/enum; %angular pitch

apo = 1;
zMin = R;
zMax = 0;
cCo = zeros(enum,3);

for j = 1:enum
    theta = -sec/2;
    for i = 1:enum
        xCo(1) = -0.95*px/2+(j-1)*px-px*enum/2+px/2;
        xCo(2) = +0.95*px/2+(j-1)*px-px*enum/2+px/2;
        xCo(3) = +0.95*px/2+(j-1)*px-px*enum/2+px/2;
        xCo(4) = -0.95*px/2+(j-1)*px-px*enum/2+px/2;

        yCo(1) = R*sin(theta-dtheta/2);
        yCo(2) = R*sin(theta-dtheta/2);
        yCo(3) = R*sin(theta+dtheta/2);
        yCo(4) = R*sin(theta+dtheta/2);

        zCo(1) = R*cos(theta-dtheta/2);
        zCo(2) = R*cos(theta-dtheta/2);
        zCo(3) = R*cos(theta+dtheta/2);
        zCo(4) = R*cos(theta+dtheta/2);

        if min(zCo)<zMin
            zMin =min(zCo);
        end
        if max(zCo)>zMax
            zMax =max(zCo);
        end

        rect(i+enum*(j-1),:) = [j xCo(1) yCo(1) zCo(1) xCo(2) yCo(2) zCo(2)
xCo(3) yCo(3) zCo(3)...
            xCo(4) yCo(4) zCo(4) apo 0.95*px 0.95*px (j-1)*px-
px*enum/2+px/2 0 0.002];
```

```
        theta = theta + dtheta;
    end
    cCo(j,1) = (j-1)*px-px*enum/2+px/2;
    cCo(j,2) = 0;
    cCo(j,3) = zMax-zMin;

end
rect(:,4) = rect(:,4) - zMin;
rect(:,7) = rect(:,7) - zMin;
rect(:,10) = rect(:,10) - zMin;
rect(:,13) = rect(:,13) - zMin;
rect(:,19) = zMax-zMin;


focus=[0 0 50]/1000;
center = [0 0 zMax-zMin];
ThT = xdc_rectangles (rect, cCo, focus);
% figure(1)
% subplot(2,1,1)
% % xdc_show(Th)
% clear rect; clear cCo;
% show_xdc(ThT)
% set(figure(1), 'Position', [0 0 800 800])
% title('transmit aperture, 32 elements')
% colorbar('off')
% % close(figure(6))

%PART 1(b): create curved array for Rx------------------------------------
----
cCo = zeros(enum,3);
zMin = R;
zMax = 0;
theta = -sec/2;

for j = 1:enum
        yCo(1) = R*sin(theta-0.95*dtheta/2);
        yCo(2) = R*sin(theta-0.95*dtheta/2);
        yCo(3) = R*sin(theta+0.95*dtheta/2);
        yCo(4) = R*sin(theta+0.95*dtheta/2);

        zCo(1) = R*cos(theta-dtheta/2);
        zCo(2) = R*cos(theta-dtheta/2);
        zCo(3) = R*cos(theta+dtheta/2);
        zCo(4) = R*cos(theta+dtheta/2);

    for i = 1:enum
        xCo(1) = -1.0*px/2+(i-1)*px-px*enum/2+px/2;
        xCo(2) = +1.0*px/2+(i-1)*px-px*enum/2+px/2;
        xCo(3) = +1.0*px/2+(i-1)*px-px*enum/2+px/2;
        xCo(4) = -1.0*px/2+(i-1)*px-px*enum/2+px/2;

        if min(zCo)<zMin
            zMin =min(zCo);
        end
        if max(zCo)>zMax
            zMax =max(zCo);
```

```
        end

        rect(i+enum*(j-1),:) = [j xCo(1) yCo(1) zCo(1) xCo(2) yCo(2) zCo(2)
xCo(3) yCo(3) zCo(3)...
            xCo(4) yCo(4) zCo(4) apo 0.95*px 0.95*px 0 R*sin(theta) 0.002];

    end
    cCo(j,1) = 0;
    cCo(j,2) = R*sin(theta);
    cCo(j,3) = zMax-zMin;

    theta = theta + dtheta;
end

cCo(:,3) = zMax-zMin;
rect(:,4) = rect(:,4) - zMin;
rect(:,7) = rect(:,7) - zMin;
rect(:,10) = rect(:,10) - zMin;
rect(:,13) = rect(:,13) - zMin;
rect(:,19) = zMax-zMin;


focus=[0 0 50]/1000;
center = [0 0 zMax-zMin];
ThR = xdc_rectangles (rect, cCo, focus);
% figure(1)
% subplot(2,1,2)
% % xdc_show(Th)
% clear rect; clear cCo;
% show_xdc(ThR)
% set(figure(1), 'Position', [0 0 500 800])
% title('receive aperture, 32 elements')
% colorbar('off')
% close(figure(6))

%%
%--------------------------------------------------------------------------
------
%PART II: create point scatterers, perform calc_scat, reconstruct B-mode
%  Set initial parameters
% Generate the transducer apertures for send and receive
f0=4e6; % Transducer center frequency [Hz]
fs=100e6; % Sampling frequency [Hz]
c=1540; % Speed of sound [m/s]
lambda=c/f0; % Wavelength
set_sampling(fs);% Set the sampling frequency
D = 50;
focus=[0 0 D]/1000; % Initial electronic focus [m]

%  Define the transducer
%  Set the impulse response and excitation of the emit aperture
impulse_response=sin(2*pi*f0*(0:1/fs:2/f0));
impulse_response=impulse_response.*hanning(max(size(impulse_response)))';
xdc_impulse (ThT, impulse_response);
excitation=sin(2*pi*f0*(0:1/fs:2/f0));
xdc_excitation (ThT, excitation);
% Set the impulse response for the receive aperture
```

```
xdc_impulse (ThR, impulse_response);

% Load the computer phantom
[phantom_positions, phantom_amplitudes] = AC_point_scatterers(2,D);

% Do phased array imaging
no_lines=150; % Number of A-lines in image
% sector=90 * pi/180; % Size of image sector
sector = sec;
d_theta=sector/no_lines; % Increment in angle for image
% Pre-allocate some storage
image_data=zeros(800,no_lines);
theta= -sector/2;
for i=1:no_lines
    % Set the focus for this direction
    xdc_focus (ThT, 0, [0 0 D]/1000);
    xdc_focus (ThR, 0, [0 D*sin(theta) D*cos(theta)]/1000);
    % Calculate the received response
    [v, t1]=calc_scat(ThT, ThR,  phantom_positions, phantom_amplitudes');
    % Store the result
    image_data(1:max(size(v)),i)=v';
    times(i) = t1;
    % Steer in another angle
    theta = theta + d_theta;
    disp(strcat(int2str(i), ' out of ',int2str(no_lines),' calc_scat
done'));
end

% a gray scale image
min_sample=min(times)*fs;
for i=1:no_lines
    rf_env=abs(hilbert([zeros(round(times(i)*fs-min_sample),1);
image_data(:,i)]));
    env(1:size(rf_env,1),i)=rf_env;
    disp(strcat(int2str(i), ' out of ',int2str(no_lines),' envelope
done'));
end
% make logarithmic compression to a 60 dB dynamic range
% with proper units on the axis
env_dB=20*log10(env);
env_dB=env_dB-max(max(env_dB));
env_gray=127*(env_dB+20)/20;
% depth=((0:size(env,1)-1)+min_sample)/fs*c/2;

figure(2)
im = [zeros(3621,150);env_gray]';
depth=(0:size(im,2)-1)/fs*c/2;
angle=((1:no_lines)-no_lines/2)*d_theta;

ang2 = rad2deg(angle);
pixelsx = 800;
pixelsy = 800;
y = 0:(max(depth)/(pixelsy-1)):max(depth);
x = -max(depth)/2:max(depth)/(pixelsx-1):+max(depth)/2;
B = scanConversion(im, ang2, [0.08, 0.080], 1540, 1/fs, [800,800]);
image(x*1000, y*1000,B)
colormap(gray(128))
```

```
xlabel('Lateral distance [mm]')
ylabel('Depth [mm]')
title(strcat(int2str(radtodeg(sec)), '°; ',...
    int2str(enum),'x',int2str(enum), ' curved; ROC'...
    ,int2str(R*1000),'mm; pitch', int2str(px*1e6),'um'))
color('white')

%display b-mode

figure(8)
im = [zeros(3621,150);env_gray]';
depth=(0:size(im,2)-1)/fs*c/2;
angle=((1:no_lines)-no_lines/2)*d_theta;

ang2 = rad2deg(angle);
pixelsx = 800;
pixelsy = 800;
y = 0:(max(depth)/(pixelsy-1)):max(depth);
x = -max(depth)/2:max(depth)/(pixelsx-1):+max(depth)/2;
B = scanConversion(im, ang2, [0.08, 0.080], 1540, 1/fs, [800,800]);
image(x*1000, y*1000,B)
colormap(gray(128))
xlabel('Lateral distance [mm]')
ylabel('Depth [mm]')
title(strcat(int2str(radtodeg(sec)), '°; ',...
    int2str(enum),'x',int2str(enum), ' curved; ROC'...
    ,int2str(R*1000),'mm; pitch', int2str(px*1e6),'um'))
color('white')
% Free space for apertures
xdc_free (ThT)
xdc_free (ThR)
```